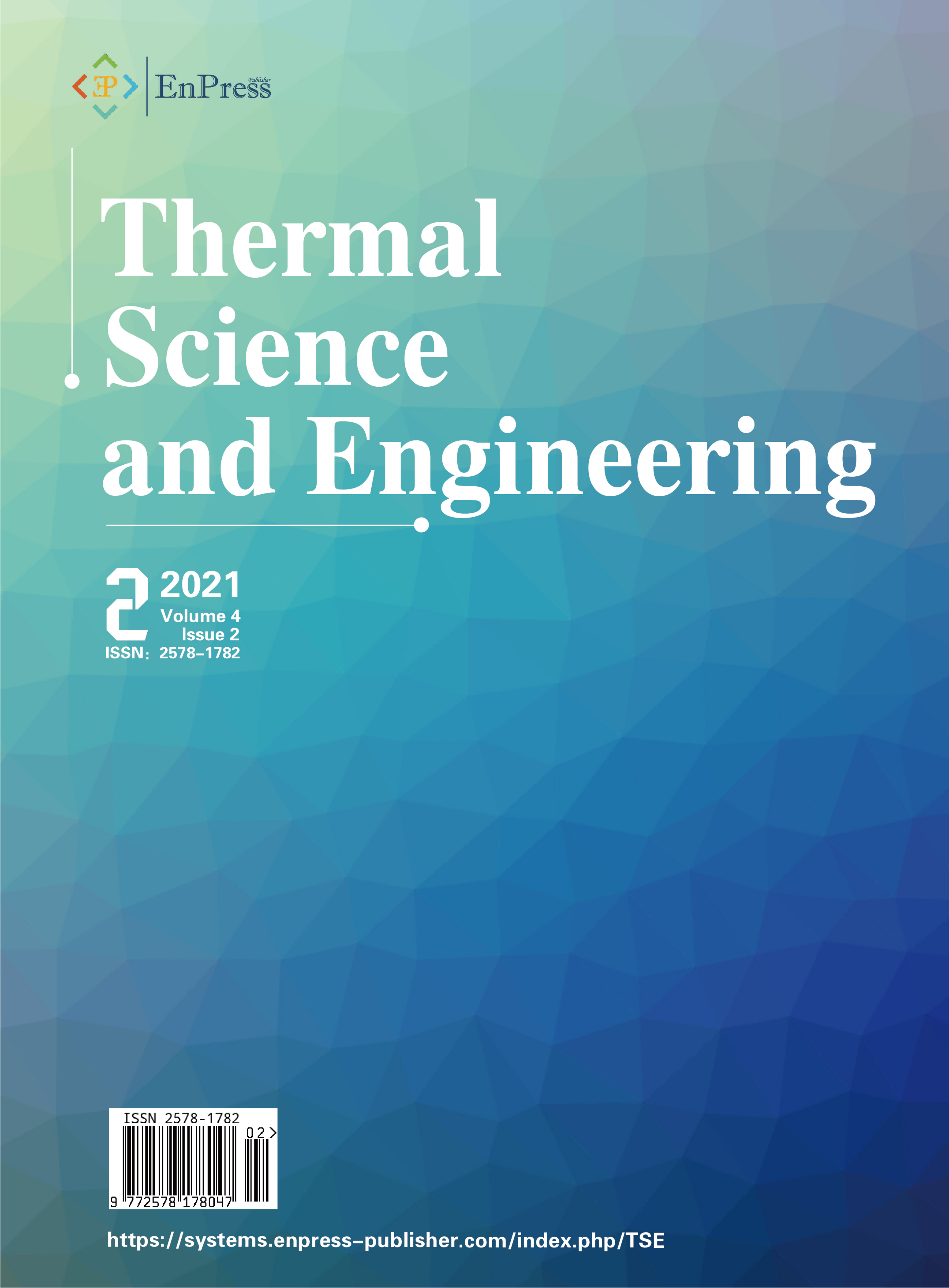

EnPress Publisher

Thermal Science and Engineering

2
2021
Volume 4
Issue 2
ISSN: 2578-1782

ISSN 2578-1782
02
9 772578 178047

https://systems.enpress-publisher.com/index.php/TSE

Editorial Board

Editor-in-Chief

Associate Editor

Editorial Board Member

Volume 4 Issue 2 • 2021

Thermal Science and Engineering

Editor-in-Chief

Prof. Gang Zhang

A-Star, Institute of High Performance Computing (IHPC), Singapore

EnPress Publisher

2021 | Volume 4 | Issue 2

Thermal Science and Engineering

https://systems.enpress-publisher.com/index.php/TSE

Contents

Thermal Science and Engineering (2021) Volume 4 Issue 2
doi:10.24294/tse.v4i2.1514

ORIGINAL RESEARCH ARTICLE

Effects of atmosphere and post catalyst on pyrolysis characteristics of Pingshuo bituminous coal

Huaixiang Li, Mengxiang Fang*, Tong Lv, Jiqing Yan, Zhixiang Xia, Jianmeng Cen

State Key Laboratory of Clean Energy Utilization, Zhejiang University, Hangzhou 310027, China. E-mail: mxfang@zju.edu.cn

ABSTRACT

In order to lighten the tar from coal pyrolysis, the effects of N_2, CH_4 and H_2 atmosphere on the pyrolysis characteristics of Pingshuo bituminous coal were investigated in a small fluidized bed, and Ni-based catalyst was placed downstream of coal pyrolysis to catalyze the upgrading of tar. The results show that both H_2 and CH_4 atmosphere can improve the conversion of coal pyrolysis and improve the yield of pyrolysis tar. Compared with CH_4 atmosphere, the post placed Ni-based catalyst in CH_4 atmosphere can increase the tar yield by 10%, increase the gas yield and H_2 yield, and transform the pyrolysis tar to the light direction. Through simulated distillation and GC-MS analysis, compared with N_2 atmosphere, CH_4, H_2 atmosphere and CH_4 + Ni increased the relative contents of naphtha, phenol oil, naphthalene oil, wash oil and anthracene oil, and the increase showed that CH_4 + Ni > H_2 > CH_4, while the asphalt content decreased. Compared with CH_4, the relative contents of aromatic hydrocarbons and aliphatic hydrocarbons increased significantly under CH_4 + Ni.

Keywords: Pyrolysis; Tar Lightening; Fluidized Bed; Post Catalyst

ARTICLE INFO

Received: 30 April 2021
Accepted: 29 June 2021
Available online: 12 July 2021

COPYRIGHT

1. Introduction

Poly-generation technology based on pyrolysis can obtain high value-added products such as semi-coke, gas and tar[1], which can not only alleviate the environmental problems caused by energy utilization from the source, but also create higher energy economic benefits. In recent years, researchers at home and abroad have paid extensive attention to the effects of atmosphere and catalyst on coal pyrolysis characteristics. Gao *et al.*[2] studied coal hydropyrolysis in a falling fixed bed at atmospheric pressure, the results show that the yield of tar from hydrotreating at 800 ℃ is 30% higher than that in N_2 atmosphere. Hydrotreating can promote the lightening of tar. Chen[3] studied the hydropyrolysis of lignite in a fixed bed. The results show that with the increase of H_2 concentration, the yield of tar increases monotonously, and the aromatic hydrocarbons and phenolic compounds in tar also increase[4]. However, the high cost of H_2 restricts the development of hydro pyrolysis[5,6], CH_4 with high hydrogen carbon ratio and relatively low cost will replace H_2 in coal pyrolysis technology[4]. Coal pyrolysis in fixed bed CH_4 atmosphere shows CH_4 atmosphere is equivalent to inert atmosphere at low temperature which has little effect on the yield of tar. Yan[7] found that the tar yield can be improved under the low temperature of small fluidized bed CH_4, and the tar yield will be flluidized bed CH_4, and the tar yield will be further improved under the high temperature due to the free radicals and hydrogen produced by the decomposition of methane. CH_4 can improve the yield of tar, but the effect is limited. The catalytic activation of methane to improve the yield of tar has been widely concerned. The influence of different catalyst and catalyst arrangement on tar yield was investigated in fixed bed by Zhao[8]. It was found that Mo/HZSM-5 and Ni/Al_2O_3 could increase tar at 600 °C by 17.5%, and the content of light components in tar is more than 90%. Wang *et al.*[9] improved tar yield by combining in-situ catalytic cracking of coal pyrolysis tar with methane in a fixed bed, and the average molecular weight of tar decreased. Compared with 5% Co/Al_2O_3 and 5% Fe/Al_2O_3, 5% Ni/Al_2O_3 obtained light tar with higher content and yield. Li[10] found that adding pre-Mo/HZSM-5 in CH_4 atmosphere can greatly improve the tar yield, and the pre-catalyst has better effect than the mixing of coal and catalyst. Yan[7] found that the addition of Ni-based catalyst under CH_4 + N_2 atmosphere increased the tar yield at 600 °C by 40% and the aromatic hydrocarbons content by 16% compared with no catalyst added.

Based on the above research results, CH_4, H_2 atmosphere and catalyst can effectively improve the yield and quality of coal pyrolysis tar, and the separation of coal and catalyst is better. However, nowadays, most of the catalytic activation of methane is carried out in fixed bed, and less research is involved in small fluidized bed which is closer to industrial application. Therefore, this study investigated the effects of N_2, CH_4 and H_2 atmosphere on the pyrolysis characteristics of Pingshuo bituminous coal in a small fluidized bed, and placed Ni-based catalyst on the downstream of coal pyrolysis to achieve the goal of catalytic upgrading of coal pyrolysis gas-phase tar before condensation.

2. Experimental part

2.1 Preparation of coal sample and catalyst

Shanxi Pingshuo bituminous coal was selected as the experimental coal, and the raw coal was crushed and screened to obtain a particle size of 1.25–2 mm coal samples. Before the experiment, the coal sample was dried in a blast drying oven at 105 °C for 6 hours, sealed and stored for use. The fluidizing medium of fluidized bed is 0.25–0.35 mm quartz sand. See **Table 1** for industrial analysis and elemental analysis of experimental coal samples.

Table 1. Industrial analysis and elemental analysis of Pingshuo bituminous coal

Industrial analysis w_{ad}/%				**Elemental analysis w_{ad}/%**				
M	A	V	FC	C	H	N	S	O*
1.20	39.08	25.31	34.41	42.49	2.16	0.94	2.47	11.66

*Obtained by subtraction

The catalyst Ni/Al_2O_3 is prepared by equal volume impregnation[11]. It is impregnated with Ni $(NO_3)_2 \cdot 6H_2O$ salt solution for 12 hours, dried at 105 °C for 6 hours, roasted at 550 °C for 6 hours, sealed and stored for later use after reduction, and the Ni load is 5% (mass fraction).

2.2 Experimental method

The small-scale fluidized bed pyrolysis experimental system used in the experiment is shown in **Figure 1**. The experimental system is mainly composed of a gas supply system, a preheating section, a reaction section, a heat preservation section (catalyst placement section), and a product collection device. The inner diameter of the preheating section is 20 mm, and the length is 3.5 m, the inner diameter of the reaction section is 50 mm, and the length is 1.2 m, heated by silicon carbide rods arranged uniformly and graded, the temperature can reach 1,000 °C, and the insulation section is heated by resistance wire. The liquid collection device is composed of two-stage serial serpentine tubes (placed in a constant temperature and low temperature tank at -10 °C), filters and three-stage parallel glass fiber filter cartridges to ensure complete collection of tar and water.

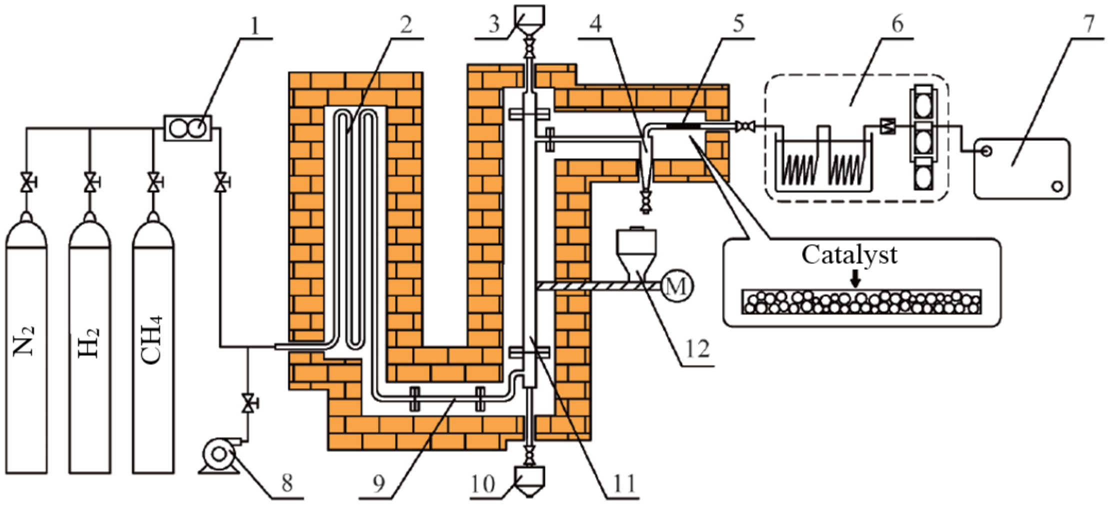

Figure 1. Experimental system of small fluidized bed pyrolysis.
1–mass flowmeter; 2–preheating section; 3–upper hopper; 4–cyclone separator; 5–catalyst; 6–liquid collection device; 7–air bag; 8–air pump; 9–horizontal section; 10–lower hopper; 11–reaction section; 12–screw feeder.

Before the experiment, 550 g quartz sand was fed from the upper hopper as bed material. Set the heating program and wait for the fluidized bed furnace body to rise temperature, during which a small amount of N_2 is introduced to ensure safe operation. When the temperature of the reaction section rises to the pyrolysis temperature, adjust the fluidization gas volume to 25 L/min. The fluidization gas is N_2, and the mixed volume ratio is 60% N_2 + 40% CH_4 and 60% N_2 + 40% H_2. When the atmosphere is completely replaced with the pyrolysis atmosphere set in the experiment, slowly feed 30 g of coal sample from the upper hopper, immediately open 120 L aluminum foil air bag to collect the gas. The pyrolysis tar and water are fully condensed through the liquid collection device, and the pyrolysis time is 3 min. After the reaction, open the lower hopper to collect the semi-coke and bed material, remove the hopper and seal it for storage to prevent the high-temperature oxidation of the semi-coke. After it is naturally cooled to room temperature, sieved to obtain the quality of the semi-coke. The tar and water are washed repeatedly with analytical pure acetone solution, and sealed and stored after filtering the fly ash. The quality of tar and water is obtained by the subtraction method from the quality of the liquid collection device before and after the reaction. The post catalyst is placed behind the cyclone separator, the temperature of the catalytic section is set to 500 °C, and the amount of catalyst is 12 g.

2.3 Calculation, measurement and analysis of pyrolysis product yield

The water content of the tar was measured with ZDJ-2S card type micro moisture tester to calculate the mass of water and tar. The volume of pyrolysis gas is obtained according to the difference between the measured volume of gas meter and the volume of carrier gas. The yield of pyrolysis products is calculated by the following formula:

$$Y_{\mathrm{char}} = \frac{W_{\mathrm{char}} - W \times A}{W \times (1 - A - M)} \times 100\% \tag{1}$$

$$Y_{tar} = \frac{W_{tar}}{W \times (1 - A - M)} \times 100\% \tag{2}$$

$$Y_{water} = \frac{W_{water} - W \times M}{W \times (1 - A - M)} \times 100\% \tag{3}$$

$$Y_{gas} = \frac{V_{gas}}{W \times (1 - A - M)} \times 100\% \tag{4}$$

In the equation: Y_{char}, Y_{tar}, Y_{water} and Y_{gas} are the yields of semi-coke, tar, water and gas respectively (calculated on dry ash free basis); W_{char}, W_{tar} and W_{water} are the quality of semi-coke, tar and water respectively; V_{gas} is the volume of gas; W is the quality of pyrolysis coal; *A* and *M* are the ash and moisture content of coal sample (calculated on air drying basis).

The gas components are detected by Agilent 7890A, and standard gas is used for calibration before detection. The gas components CH_4, C_2–C_3 (the sum of C_2H_4, C_2H_6, C_3H_6 and C_3H_8), CO, CO_2 and H_2 were obtained and the yield of the above components are calculated.

After the moisture content of the tar solution is measured, the excess anhydrous sodium sulfate is used to remove the moisture, and then the tar sample is obtained by distillation with a rotary distiller for 6 hours. The distillation temperature is 62 ℃ and the rotating speed is 20 r/min. The tar components are analyzed by GC-MS with GC/MS-QP2010SE. The tar sample is diluted to 5% with analytical pure CH_2Cl_2 and then injected. The temperature of the injection port is 300 ℃. The chromatographic column model is SH-Rxi-5Sil MS and its specification is 30 m × 0.25 mm × 0.25 μm. GC temperature rise procedure: column temperature was kept at 60 ℃, maintained for 2 min; then raise the temperature to 180 ℃ at the heating rate of 4 ℃/min for 2 minutes, and finally raise the temperature to 300 ℃ at the heating rate of 10 ℃/min for 10 minutes. The tar fraction is obtained by simulated distillation of gas chromatography Agilent 7890A, and the specification of packed column is 1/8 inch × 0.5 m, the tar sample is diluted to 5% with analytical pure CS_2 and then injected. The temperature rise procedure of GC is: the initial temperature is 35 ℃ and maintained at 35 ℃ for 0.5 min; rise to 350 ℃ at the heating rate of 10 ℃/min for 1 min, then rise to 400 ℃ at the heating rate of 5 ℃/min for 10 min. During determination, H_2 (40 mL/min) and air (400 mL/min) are combustion gas and N_2 (25 ml/min) is carrier gas.

3. Results and discussion

In this paper, the pyrolysis product yield, gas component yield, tar component and fraction distribution characteristics of Pingshuo bituminous coal under different pyrolysis temperatures (500 ℃, 600 ℃, 700 ℃, 800 ℃), different pyrolysis atmospheres (N_2, 60% N_2 + 40% CH_4, 60% N_2 + 40% H_2, abbreviated as N_2, CH_4, H_2 for convenience) and post catalyst Ni/Al_2O_3 were investigated in a small fluidized bed.

3.1 Effect of atmosphere on the yield of coal pyrolysis products

Figure 2 shows the yield law of coal pyrolysis products under different pyrolysis atmospheres and different pyrolysis temperatures. The mass recovery of each experiment is more than 94%, and the experiment has good repeatability.

Figure 2(a) shows the effects of different atmospheres on the yield of semi-coke from coal fluidized bed pyrolysis. Under the three atmospheres, the yield of coal pyrolysis semi-coke decreased gradually with the increase of pyrolysis temperature. Compared with N_2 atmosphere, the yield of semi-coke in H_2 atmosphere decreases, and the trend is basically the same as that in N_2 atmosphere. In the process of coal pyrolysis, the activated hydrogen free radicals provided by the H_2 atmosphere combine with the fragment free radicals generated by the breakage of chemical bonds in the coal, reducing the degree of polycondensation between fragments., which effectively improves the coal pyrolysis conversion and promotes the release of volatile matter. Compared with N_2, CH_4 atmosphere reduces the yield of semi-coke in the low temperature section lower than 600 ℃, indicating that CH_4 atmosphere promotes the coal pyrolysis reaction at low temperature. However, the degree of CH_4 atmosphere promoting coal pyrolysis at low temperature is not as good as that of H_2 atmosphere, which indicates that the nature of CH_4 at low temperature is relatively stable and the amount of activated free radicals provided is small. While in the high temperature section above 700 ℃, the CH_4 atmosphere increases the yield of semi-coke. Because there are two competitive reactions of CH_4 atmosphere on coal pyrolysis: on the one hand, the free radicals generated by CH_4 decomposition stabilize the molecular fragments generated by coal pyrolysis and inhibit the polycondensation reaction of fragments, so as to improve the conversion of coal; on the other hand, decomposition of methane occurs at high temperature $CH_4 \rightarrow C + 2H_2$, and the pyrolysis carbon deposition leads to an increase in the semi-coke yield, while inhibiting the precipitation of volatiles in the semi-coke. This confirmed that the increase in pyrolysis semi-coke yield at high temperature is mainly caused by the carbon deposition of methane cracking at high temperature.

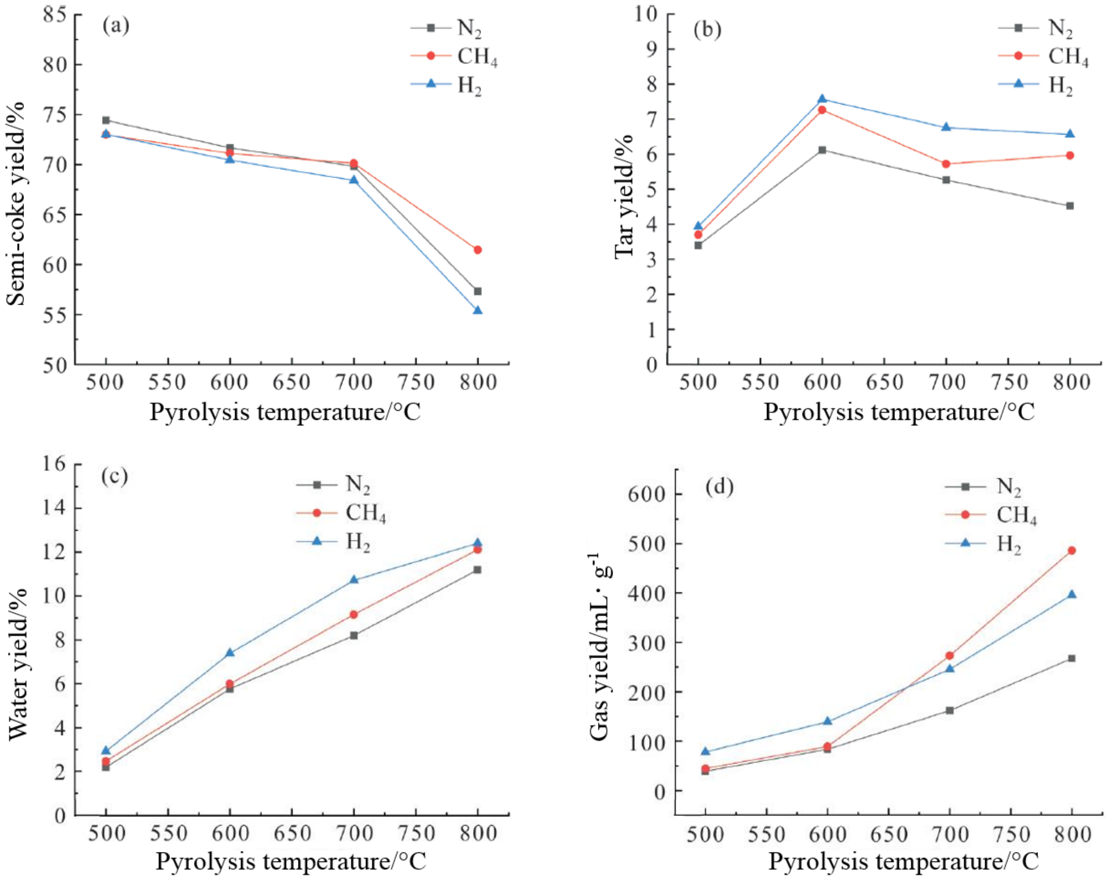

Figure 2. Yield of coal pyrolysis products under different atmospheres.

Figure 2(b) shows the effects of different atmospheres on the yield of tar from coal fluidized bed pyrolysis. It can be seen that the yield of pyrolysis tar first increases and then decreases with the increase of pyrolysis temperature in N_2 and H_2 atmosphere, and reaches the maximum at 600 ℃. Under CH_4 atmosphere, the tar below 700 ℃ meets the trend of first increasing and then decreasing, while the tar yield is higher than 700 ℃ at 800 ℃. This is related to the previous H_2 production from methane cracking at high temperature. CH_4 cracking at 800 ℃ produces a large amount of H_2, so the tar yield is further improved compared with 700 ℃. Compared with N_2 atmosphere, CH_4 and H_2 atmosphere can promote the increase of tar yield, and the promotion effect of H_2 is more obvious. This is because these two gases produce a large number of free radicals, which stabilize the macromolecular groups produced by coal pyrolysis, and H_2 atmosphere has a stronger ability to provide hydrogen free radicals.

Figure 2(c) shows the effect of different atmospheres on the yield of pyrolysis water in fluidized bed. Under the three atmospheres, the yield of pyrolysis water increases gradually with the increase of pyrolysis temperature, and the increasing trend in the high temperature section slows down. This is because more hydrogen radicals are produced at high temperature and the probability of reacting with O increases. Compared with N_2 atmosphere, H_2 atmosphere and CH_4 atmosphere promote the formation of pyrolysis water, and the yield of water in H_2 atmosphere is higher. This is because hydrogen free radicals combine with hydroxyl groups produced by coal pyrolysis to produce water. The number of hydrogen free radicals is the largest in H_2 atmosphere, so the yield of aquatic products is the highest.

Figure 2(d) shows the effects of different atmospheres on the yield of coal pyrolysis gas in coal fluidized bed. Under the three atmospheres, the gas yield increases gradually with the increase of pyrolysis temperature. This is because at high temperature, the organic matter in coal decomposes more completely and the gas is released more thoroughly. The effect of pyrolysis temperature on gas yield is more significant than pyrolysis atmosphere. Compared with N_2 atmosphere, the gas yield in H_2 atmosphere is increased. Under CH_4 atmosphere, the increase of gas yield in low temperature section is not obvious, because CH_4 atmosphere is inert in low temperature section. The increase of gas yield in high temperature section is significant, which is mutually confirmed by the decomposition of methane to produce hydrogen at high temperature.

3.2 Effect of atmosphere on the yield of gas components

Figure 3 shows the effect of atmosphere on the yield of each component of pyrolysis gas in coal fluidized bed. Because the carrier gas flow required for fluidization in this experiment is much larger than the amount of gas generated by pyrolysis, considering the metering error, this paper will no longer investigate the gas yield in the pyrolysis gas with the same composition as the carrier gas. As can be seen from **Figures 3(a)–3(e)**, with the increase of pyrolysis temperature, the yields of various gases produced by pyrolysis in different atmospheres show an increasing trend.

It can be seen from **Figure 3(a)** that H_2 atmosphere can significantly promote the formation of CH_4 during coal pyrolysis. The formation of CH_4 mainly comes from the bond breaking of alkyl compounds during pyrolysis[14]. The hydrogen radicals provided by H_2 atmosphere can effectively stabilize the side chain groups such as methyl and methylene separated from the macromolecular network of coal, so as to promote the formation of CH_4. In the figure, when H_2 atmosphere increases from 700 ℃ to 800 ℃, the small decrease of CH_4 yield is the result of the increase of CH_4 cracking rate at high temperature.

Figure 3(b) shows that compared with N_2 atmosphere, CH_4 and H_2 atmosphere are conducive to the formation of C_2–C_3 gas. At high temperature, free radicals such as methyl and methylene produced by coal pyrolysis can be combined with free radicals provided by CH_4 or H_2 atmosphere to form stable small molecular hydrocarbons[15]. At low temperature, CH_4 and H_2 have similar promoting effects on the release of C_2–C_3. At high temperature, the ability of CH_4 atmosphere to produce living free radicals gradually increases, and the yield of C_2–C_3 is slightly higher than that of H_2 atmosphere.

Figure 3(c) and **Figure 3(d)** show the changes of CO and CO_2 yields under different atmospheres, respectively. In the process of coal pyrolysis, the production of CO comes from the decomposition of carbonyl group, CH_3O-, phenolic hydroxyl and oxygen-containing heterocycles, while CO_2 mainly comes from the decomposition of carboxyl, esters and inorganic carbonates[16]. It can be seen that the increase of temperature will promote the decomposition of these functional groups and make the precipitation of CO and CO_2 more thorough. The existence of activated free radicals in pyrolysis atmosphere can also promote the bond breaking of functional groups and the formation of stable compounds. The yield of CO in H_2 atmosphere is higher than that in N_2 atmosphere, the yield of CO_2 is lower than that in N_2 atmosphere, because the occurrence of reaction $H_2 + CO_2 \rightarrow H_2O + CO$ promotes the conversion of CO_2 to CO, resulting in a more significant increase in the yield of CO. CH_4 atmosphere at 600 ℃ and below has little effect on the yield of CO and CO_2 in pyrolysis gas; the precipitation of CO_2 was slightly inhibited above 700 ℃, while the yield of CO was between N_2 and H_2 atmosphere. It can be inferred that the activation and decomposition of CH_4 is mainly above 700 ℃, while the CH_4 gas itself in the low temperature section has no obvious effect on the reaction of functional groups in coal.

Figure 3(e) shows the variation of H_2 yield with pyrolysis temperature in N_2 and CH_4 atmosphere. Dehydropolycondensation of aromatic structure in coal under N_2 atmosphere is the main source of H_2 in pyrolysis gas[17]. With the increase of pyrolysis temperature, the H_2 yield increases gradually and slowly. Compared with N_2 atmosphere, H_2 yield in CH_4 atmosphere increased significantly with temperature. At 700 ℃ and above, the high temperature decomposition of CH_4 in the carrier gas becomes the main source of H_2.

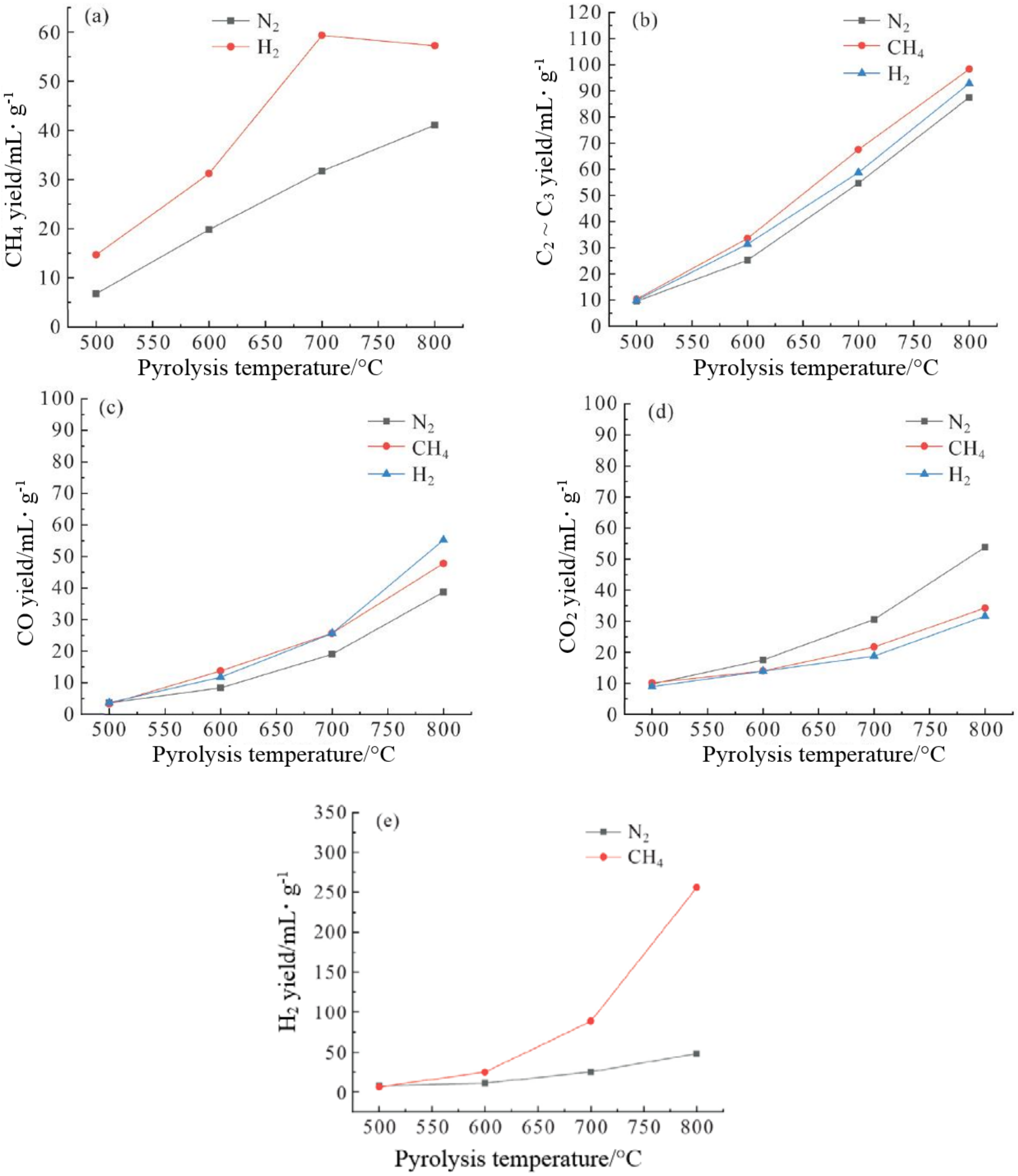

Figure 3. Yield of pyrolysis gas components under different atmospheres.

3.3 Effect of post catalyst on the yield of pyrolysis products

Figure 4 shows the effect of post catalyst Ni/Al_2O_3 on the yield of pyrolysis products. **Figure 4(a)** shows that under the action of post catalyst Ni/Al_2O_3, the yield of semi-coke is lower than that without catalyst. **Figures 4(b)–4(d)** show that the post Ni-based catalyst redistributes the gas-liquid products of coal pyrolysis. Under the condition of no catalyst, the yield increases by 600%, especially under the condition of no catalyst. The yield of aquatic products decreased and the yield of gas increased. The redistribution of the above product yields is attributed to the good catalytic effect of Ni catalyst on CH_4[18]. Due to the existence of Ni based catalyst, CH_4 atmosphere will produce more active radicals such as methyl, methylene and hydrogen radicals. These radicals will recombine the pyrolysis products after contacting with the volatile substances of coal pyrolysis, increasing the yield of tar and gas. As a result, coal pyrolysis is carried out more in the direction of volatilization analysis, resulting in a decrease in the yield of semi-coke.

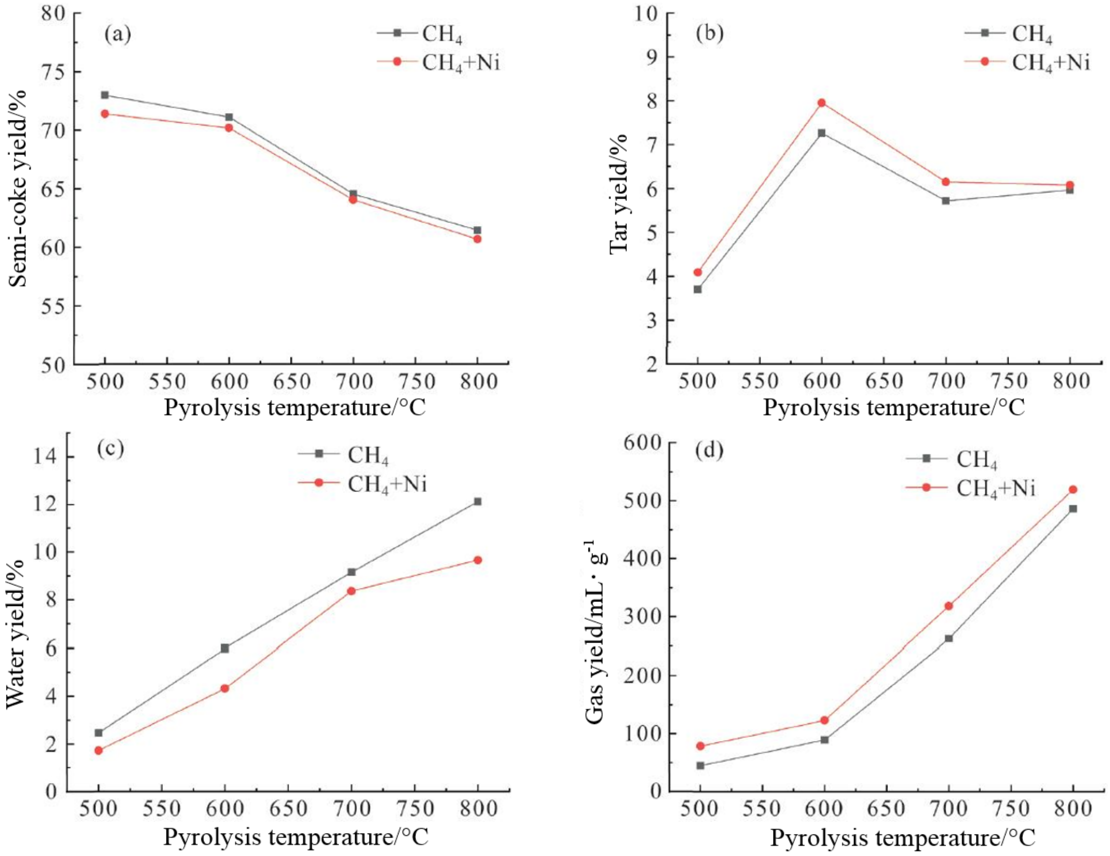

Figure 4. Effect of post catalyst on the yield of pyrolysis products.

Figure 5 shows the effect of post catalyst on H_2 yield. The results showed that Ni-based catalyst promoted H_2 precipitation at various pyrolysis temperatures, especially at 600 ℃ and 800 ℃. At 700 ℃, Ni-based catalyst has no obvious effect on H_2 yield.

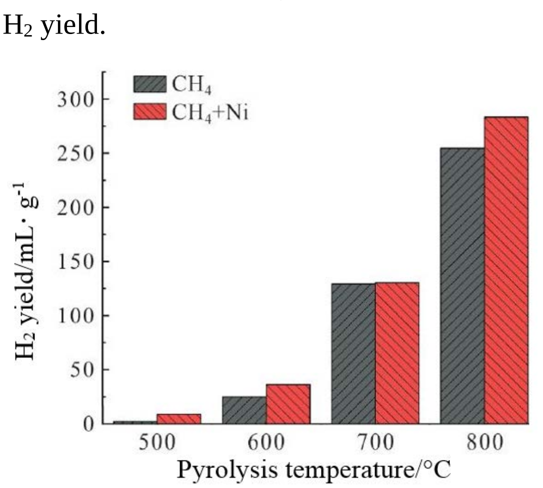

Figure 5. The effect of post catalyst on H_2 yield.

3.4 Influence of atmosphere and post catalyst on tar

Samples obtained under various working conditions shall be analyzed with simulated distillation and GC-MS. Tar samples of N_2, CH_4, H_2 and CH_4 + Ni at 600 ℃ were analyzed as representative data. According to ASTM D2887 method, tar is divided into naphtha with a boiling point of lower than 170 ℃, phenol oil with a boiling point of 170–210 ℃, wash oil with a boiling point of 210–230 ℃, naphthalene oil with a boiling point of 230–300 ℃, anthracene oil with a boiling point of 300–360 ℃ and asphalt with a boiling point of more than 360 ℃.

Figure 6(a) shows that compared with N_2 atmosphere, CH_4, H_2 and CH_4 + Ni all make the simulated distillation curve of tar move to the low temperature zone, and the moving range is CH_4 +

Ni > H_2 > CH_4. This shows that the tar is transforming to the direction of lightening under CH_4 and H_2 atmosphere, and the component content of light tar is higher in CH_4 + Ni atmosphere. The yield of tar with boiling point lower than 360 ℃ is as follows: CH_4 + Ni > H_2 > CH_4 > N_2. The yield of oil with boiling point lower than 360 ℃ under CH_4 + Ni is 14.3% higher than that under CH_4. **Figure 6(b)** shows the effects of atmosphere and catalyst on tar fraction. It is found that compared with N_2 atmosphere, the contents of light oil, phenol oil, naphthalene oil, wash oil and anthracene oil under the conditions of CH_4, H_2 and CH_4 + Ni are increased, and the increase amount shows that CH_4 + Ni > H_2 > CH_4, while the asphalt content decreases.

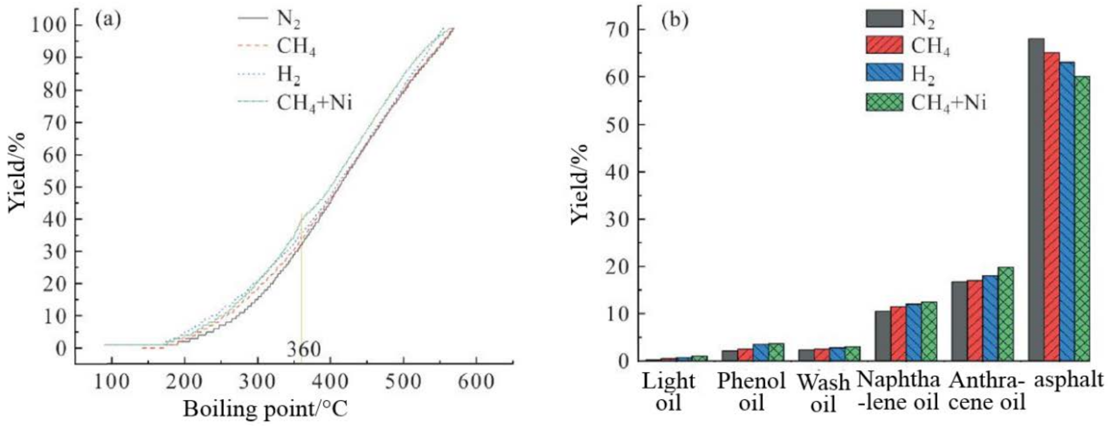

Figure 6. Effects of atmosphere and post-catalyst on tar simulated distillation curve **(a)** and tar fraction **(b)**.

Table 2 shows the GC-MS analysis of pyrolysis tar at 600 ℃. It can be seen from **Table 2** that there are more aromatic hydrocarbons in tar under N_2 atmosphere, with a relative content of 48.14%, followed by aliphatic hydrocarbons and phenols, while the content of oxygen-containing non-phenolic aromatic hydrocarbons is relatively small. Compared with N_2 atmosphere, the relative content of aromatic hydrocarbons in tar in CH_4 and H_2 atmosphere is lower, while the relative content of aliphatic hydrocarbons increases, which indicates that aromatic hydrocarbons are transformed into aliphatic hydrocarbons in reducing atmosphere, because some aromatic hydrocarbons will be converted into aliphatic hydrocarbons by addition reaction under the action of hydrogen free radicals. Compared with CH_4 atmosphere, the addition of post Ni-based catalyst in CH_4 atmosphere will greatly increase the relative contents of aromatic hydrocarbons and aliphatic hydrocarbons, while the phenolic substances will be greatly reduced. This is because CH_4 produces a large number of methyl, methylene and hydrogen free radicals under the action of Ni-based catalyst, which react when contacting with gas-phase tar, so that some phenolic substances are reduced to aromatic hydrocarbons. At the same time, under the action of Ni-based catalyst, aliphatic hydrocarbons also broke, resulting in a further increase in the relative content of aliphatic hydrocarbons. Compared with N_2 atmosphere, the relative content of heteroatom compounds in tar under the conditions of CH_4, H_2 and CH_4 + Ni is reduced, indicating that CH_4 and H_2 atmosphere can remove heteroatoms to a certain extent.

Table 2. GC-MS analysis of pyrolysis tar at 600 ℃

Atmosphere	**Relative content %**					
	Aromatic hydrocarbons	**Phenols**	**Oxygenated non-phenolic aromatic**	**Aliphatic hydrocarbons**	**Alcohols, ketones, ethers, acids**	**Heteroatom compounds**
N_2	48.14	16.39	6.87	19.35	0.81	8.43
CH_4	38.95	29.27	4.22	22.29	0.79	4.48
H_2	45.70	17.68	2.90	25.36	0.54	7.82
CH_4 + Ni	46.50	14.44	3.38	27.37	1.78	6.52

4. Conclusion

(1) Compared with N_2 atmosphere, both CH_4 and H_2 can improve the conversion of coal pyrolysis, and the promotion effect of H_2 is more obvious. H_2 reduces the yield of semi-coke while improves the yield of tar, water and gas. The effect of CH_4 on the four products is basically the same as that of H_2, but CH_4 will decompose at high temperature, resulting in an increase in the yield of semi-coke at high temperature compared with N_2 atmosphere.

(2) H_2 atmosphere can obviously promote the formation of CH_4. Compared with N_2 atmosphere, both CH_4 and H_2 atmosphere are conducive to the formation of C_2–C_3. H_2 atmosphere increases the yield of CO and reduces the yield of CO_2. The yield of H_2 in CH_4 atmosphere is higher.

(3) Compared with CH_4 atmosphere, the addition of post Ni-based catalyst in CH_4 atmosphere increases the tar yield by 10%, the gas yield and the H_2 yield is increased, and the tar is transformed to the direction of lightening. Compared with N_2, CH_4, H_2 and CH_4 + Ni increased the relative contents of light oil, phenol oil, naphthalene oil, wash oil and anthracene oil, and the increase showed that $CH_4 + Ni > H_2 > CH_4$, while the asphalt content decreased. Compared with CH_4, CH_4 + Ni greatly increases the relative content of aromatic hydrocarbons and aliphatic hydrocarbons in tar.

Acknowledgements

Fund Project: National Key Research and Development Program (2018YFB0605000).

Conflict of interest

The authors declare that they have no conflict of interest.

References

1. Deng C. Exploratory experimental study on coal partial gasification of in circulating fluidized bed [MSc thesis]. Beijing: University of Chinese Academy of Sciences (The institute of Engineering Thermophysics, Chinese Academy of Sciences); 2020.
2. Gao R, Dou B, Chang Q, *et al*. Effect of temperature and hydrogen on product distribution and evolution of char structure during pyrolysis of bituminous coal in a drop tube furnace. Fuel 2020; 267: 70–78.
3. Chen R. Study on Hydro-Pyrolysis of Shuicheng lignite in fixed-bed reactor [MSc thesis]. Beijing: Tsinghua University; 2015
4. Wang P, Jin L, Liu J, *et al*. Analysis of coal tar derived from pyrolysis at different atmospheres. Fuel 2013; 104: 14–21.
5. Liao H. Sun C, Li B, *et al*. Copyrolysis of coal with coke oven gas–III. Analyses of tar. Journal of Fuel Chemistry and Technology 1998; 26(1): 3–5.
6. Li B. Hydropyrolysis of Chinese coal–III: Catalytic and non-catalytic hydropyrolysis and pyrolysis under H_2–CH_4 of Shenfu bituminous coal. Journal of Fuel Chemistry and Technology 1995; 23(2): 192–197.
7. Yan Q. The effect of atmosphere and catalyst on coal pyrolysis in a fluidized bed [MSc thesis]. Hangzhou: Zhejiang University; 2017.
8. Zhao L. Study on characteristics of pyrolysis under different conditions and mechanism of catalyst used in pyrolysis [MSc thesis]. Hangzhou: Zhejiang University; 2017.
9. Wang M, Jin L, Li Y, *et al*. In-situ catalytic upgrading of coal pyrolysis tar coupled with CO_2 reforming of methane over Ni-based catalysts. Fuel Processing Technology 2018; 177: 119–128.
10. Li M. Studies on coal catalytic pyrolysis characteristics during hydrogen-rich atmosphere [MSc thesis]. Hangzhou: Zhejiang University; 2015.
11. Gao T. Study on pyrolysis characteristics of transition metal oxide supported USY zeolites to Shendong coal [MSc thesis]. Xi'an: Northwest University; 2019.
12. Chen L, Jin J, Suo Y, *et al*. Effects of methane concentration on CO-gasification of coal and methane. Boiler Technology 2010; 41(5): 1–4.
13. Xie Z, Quan B. Kinetic analysis on the main reactions in the conversion of methane catalyzed by coal char. Natural Gas Chemical Industry (C1 Chemistry and Chemical Industry) 2009; 34(4): 39–41.
14. Gao J. Meide rejie, lianjiao he meijiaoyou de jagong (Chinese) [Coal pyrolysis, coking and coal tar processing]. Beijing: Chemical Industry Press; 2010.
15. Zhao L, Guo H, Ma Q. Study on gaseous products distributions during coal pyrolysis. Coal Conversion 2007; 30(1): 5–9.
16. Siti M. Experimental research on the influence of atmosphere on pyrolysis characteristics during coal pyrolysis in fluidized bed reactor [MSc thesis]. Hangzhou: Zhejiang University; 2018.
17. Wang Y. Experiments on the influence of pyrolysis atmosphere on the fluidized bed pyrolysis characteristics of low rank coal [MSc thesis]. Hangzhou: Zhejiang University; 2020.
18. Yan Q, Cen J, Fang M, *et al*. Effect of atmosphere and methane catalytic activation on coal pyrolysis in fluidized bed. Coal Conversion 2017; 40(2): 22–28.

Thermal Science and Engineering (2021) Volume 4 Issue 2
doi:10.24294/tse.v4i2.1515

ORIGINAL RESEARCH ARTICLE

Performance analysis of ground source heat pump system under low load rate

Yangfang Dong[1,2], Zhaotian Zeng[2*], Hui Zhu[1], Yan Liu[1], Miaomeng Liang[2]

[1] *College of Energy Engineering and Building Environment, Guilin University of Aerospace Technology, Guilin 541005, China.*

[2] *College of Civil Engineering and Architecture, Guilin University of Technology, Guilin 541005, China. E-mail: zengzhaotian@163.com.*

ABSTRACT

Taking a demonstration project of a ground source heat pump system under karst geological conditions in Guilin as the research object, based on the measured data under operating conditions in a typical season, and sorted according to the importance of influencing factors, this paper mainly studies the influence of system at very low load rate and unit load rate on the operation effect of ground source heat pump system. The research results show that the ground source heat pump system is in good operating condition when the system load rate is lower than 30.00% and the unit load rate is higher than 80.00% in typical seasons, and the proportion of power consumption of units and pumps meets the energy consumption requirements of transmission and distribution system. During the operation of the heat pump unit in July, the average refrigeration performance coefficient of the unit is 4.48, and the average refrigeration energy efficiency ratio of the system is 3.59; during the operation in January, the average heating performance coefficient of the unit is 4.26, and the average heating energy efficiency ratio of the system is 3.32; the energy saving rate in summer and winter is 30.72% and 35.93%, respectively. The energy-saving effect of the ground source heat pump system is remarkable, and it is worth popularizing and applying in Guilin.

Keywords: Ground Source Heat Pump System; System Load Rate; Unit Performance Coefficient; System Energy Efficiency Ratio; Energy Saving rate

ARTICLE INFO

Received: 21 May 2021
Accepted: 30 July 2021
Available online: 9 August 2021

1. Introduction

With the development of green buildings and zero energy consumption buildings and the implementation of energy conservation and emission reduction policies, building energy conservation has become an issue to be considered in the whole life cycle of building planning, design, construction, delivery, operation and so on. The energy consumption of air conditioning system accounts for 30% to 70% of the building energy consumption. Therefore, solving the energy consumption of air conditioning system to a large extent solves the problem of building energy conservation. Ground source heat pump technology takes advantage of the fact that the soil temperature in summer is lower than the outdoor air temperature, and the soil temperature in winter is higher than the outdoor air temperature. As a natural renewable cold and heat source, it has the advantages of high efficiency and energy saving, clean and environmental protection, and low operating cost[1], which can well solve the energy problem of the air conditioning system.

Guilin is an area hot in summer and cold in winter with abundant rainfall, which is mostly concentrated in spring and summer. It is also a typical carbonate karst area with rich groundwater resources[2], which lays a foundation for the development and application of shallow geothermal energy. The ground source heat pump air conditioning system has been widely used in practical engineering projects. Guilin has also actively responded to the call for energy conservation and emission reduction policies and has built a certain scale of ground source heat pump air conditioning hot water application projects, such as the ground source heat pump system of the entrepreneurial mansion office building, the ground source heat pump system of Huayu residence community, the ground source heat pump system of public buildings of Guilin Grand Theater, Guilin Museum, Guangxi Guilin Library, and auxiliary facilities cultural square, etc. Most of the actual ground source heat pump projects in Guilin are basically under extremely low load or test conditions 2 ~ 3a before the system operation, while there are few studies on the actual operation performance, cost-effectiveness ratio, and investment payback period of the ground source heat pump system in karst areas. Most of them are based on the impact of different operation modes of the experimental platform[3,4], groundwater seepage[5], different underground pipe partitions[6], and unbalanced cooling and heating load rates[7] on the heat transfer performance of the underground pipe. Li *et al*.[8] and Wang *et al*.[9] studied the operation performance analysis of ground source heat pump and solar composite system under the energy utilization optimization strategy. Yan, Hu, Li, *et al*.[10], and Yan, Hu, Peng, *et al*.[11] studied the energy efficiency evaluation of 39 ground source heat pump demonstration projects in Wuhan and compared and analyzed the performance prediction of ground source heat pump systems based on actual monitoring geothermal data using a variety of data mining methods, Huang and Liu[12] applied random forest model to analyze the factors affecting the operation performance of geothermal system. These research results do not meet the geothermal application of Guilin because of the geological conditions or system load rate operation conditions unable to meet the use requirements in the literature. Therefore, this paper studies the actual power consumption, operating energy efficiency ratio, energy saving rate, etc. under low load rate conditions in karst areas from the measured operation data of ground source heat pump system, providing empirical data reference for subsequent geothermal application projects.

2. Project overview

The ground source heat pump project is located in the Guilin geothermal application demonstration project which is hot in summer and cold in winter, with a total construction area of 105,965 m^2, including 9,500 m^2 of the Grand Theater, 32,475 m^2 of the library, and 34,195 m^2 of the museum. The designed total cooling load of the system is 9,980.3 kW, the total heating load is 6,197.6 kW, and the domestic hot water load is 300.0 kW. The dry bulb temperature of the air conditioner in summer is 34.20 ℃, the wet bulb temperature is 27.30 ℃, and the dry bulb temperature of the air conditioner in winter is 1.10 ℃. The temperature of chilled water under refrigeration conditions in summer is 7.00/12.00 ℃, and the temperature of hot water under teating conditions in winter is 50.00/45.00 ℃. According to the “Technical code for ground-source heat pump system” GB 50366-2009[13], the design conditions in winter are selected to determine the number of buried pipe heat exchange wells. There is a total of 852 wells with a depth of 100 m, and the vertically buried pipes are made of double U-shaped PE pipes. The distance between the vertical shafts is 5 m, and the buried pipe groups are arranged in the outdoor green belt and under the road according to the function of the building.

Considering the air conditioning end load and simultaneous use coefficient, the parameters of air conditioning cold and heat source heat pump unit and water system equipment are shown in **Table 1**.

Table 1. Equipment parameters for air conditioning systems

Equipment name	**Quantity/set**	**Parameter**
Ground source heat pump unit	27	Refrigerating capacity 258.0 kW
		Heating capacity 299.0 kW
Ground source heat pump unit (waste heat recovery type)	10	Refrigerating capacity 258.0 kW
		Heating capacity 299.0 kW
Ground source side circulating pump	3 Sets (2 for use and 1 for standby)	Flow 620.00 m^3/h
		Lift 35.0 m
Circulating pump on user's side	5 Sets (4 for use and 1 for standby)	Flow 480.00 m^3/h
		Lift 32.0 m
Hot water circulating pump	2 Sets (1 for use and 1 for standby)	Flow 76.20 m^3/h
		Lift 12.8 m

Under the design conditions of the Guilin geothermal application project, in summer (June to September), the buried pipe heat exchange system is used as the main cold source of the air conditioning system, and 37 ground source heat pump units + cooling tower auxiliary air conditioning systems are operated to make domestic hot water from the recovered waste heat; in winter (January to March and December), the buried pipe heat exchange system is used as the heat source of the air conditioning system, and 20 ground source heat pump units are operated, of which 5 heat pump units are waste heat recovery type, and the recovered waste heat is used to produce domestic hot water; in the transitional season (April, May, October, and November), start five waste heat recovery ground source heat pump units, set them to the hot water priority mode, and use the recovered waste heat to produce domestic hot water.

3. Operation performance analysis method

After the completion of the construction of the ground source heat pump system project, because the library and museum have not been settled in the building, only some offices, conference rooms, and theatres (non-scheduled) have been used for a long time, so the ground source heat pump project has been operating under extremely low load rate for the first 2 ~ 3a. This paper will analyze the operating performance of the ground source heat pump system under a low load rate, and the calculation method of each parameter is:

Average refrigerating (heating) capacity during the test period:

$$W = qvc_p\rho\Delta t/3600 \tag{1}$$

Where: Δt is the average temperature difference between supply and return water at the user side of the heat pump unit, ℃; c_p is the specific constant pressure heat capacity of water supply and return, J/(kg·K); ρ is the density of water, kg/m^3; q_v is the average flow of supply and return water at the user side of the heat pump unit, m^3/s.

Load rate:

$$R = W/W_0 \tag{2}$$

Where: R is the load rate; W_0 is the refrigerating (heating) capacity under the design working condition, kW·h.

Refrigeration energy efficiency ratio of heat pump unit:

$$COP = W/\overline{W_i} \tag{3}$$

Where: the calculation formula of energy efficiency ratio of heat pump unit W is the average refrigerating (heating) capacity of the unit during the test period; $\overline{W_i}$ is the average power consumption of heat pump unit during the test period, kW·h.

Heat efficiency ratio of heat pump unit:

$$EER = W/\overline{W_i} \tag{4}$$

Accumulated refrigerating (heating) capacity during system test:

$$\sum W = \sum_{i=1}^{n} W_i \, \Delta t \tag{5}$$

Where: W_i is the refrigerating (heating) capacity of the heat pump system in the i^{th} period, kW·h.

Refrigerating (heating) capacity of the heat pump system in the i^{th} period:

$$W_i = \frac{q v_i \rho_i c_i \Delta t_i}{3\,600} \tag{6}$$

Refrigeration energy efficiency ratio of heat pump system:

$$COP_{sys} = \frac{\sum W}{\sum W_i + \sum W_j} \tag{7}$$

Where: $\sum W_i$ and $\sum W_j$ are the cumulative power consumption of all heat pump units and pumps during the system test, kW·h.

Heat efficiency ratio of heat pump system:

$$EER_{sys} = \frac{\sum W}{\sum W_i + \sum W_j} \tag{8}$$

4. Analysis of operation results

Select July in summer and January in winter as typical seasons to analyze the operation performance. Under low load rate conditions, in order to meet the requirements of air conditioning system terminal and hot water supply, the system operation time is basically 8:30 ~ 16:30 on weekdays, and shutdown on weekends. In order to avoid the large fluctuation range of test data in the startup stage and facilitate the statistical analysis of measured data, the stable operation stage of ground source heat pump system is selected for data acquisition. The instantaneous temperature of water supply and return on the user side, the instantaneous temperature of water supply and return on the ground source side, the instantaneous flow, the daily cumulative power consumption of units and pumps, etc. At 4 ~ 7 hours in the working day operation period (generally 9:00, 11:00, 14:00 and 16:00, in special cases, 7 hours are collected if the daily operation time is long or the temperature fluctuation is large) are selected for data acquisition to analyze the operation effect of the ground source heat pump system.

4.1 Operating conditions in summer

Figure 1 shows the outdoor temperature, temperature and temperature difference of supply and return water at the user side. The outdoor temperature remained at 30.00 ℃ throughout the test period, and the maximum temperature amplitude from July 20 to 31 was 4.00 ℃. The water supply temperature on the user side is basically maintained at 8.50 ℃, the average return water temperature on the user side is 12.14 ℃, and the average temperature difference of the actual supply and return level on the user side is 3.40 ℃. The supply and return water temperature at the user side decreases with the increase of outdoor temperature, and the fluctuation range of the return water temperature at the user side is greater than that of the water supply temperature. Therefore, when the outdoor temperature rises, the ground source heat pump system adopts the return water temperature control strategy on the user side, which can correspondingly reduce the water supply temperature on the user side, so as to adjust the cooling capacity of the heat pump unit to adapt to the changes of the building cooling load of the air conditioning system. The ground source heat pump system adopts intermittent operation mode, and the return water temperature on the user side shows obvious periodic intermittent changes. The system adopts the return water temperature control on the user side, which causes the intermittent change of the water supply temperature on the user side to be weaker.

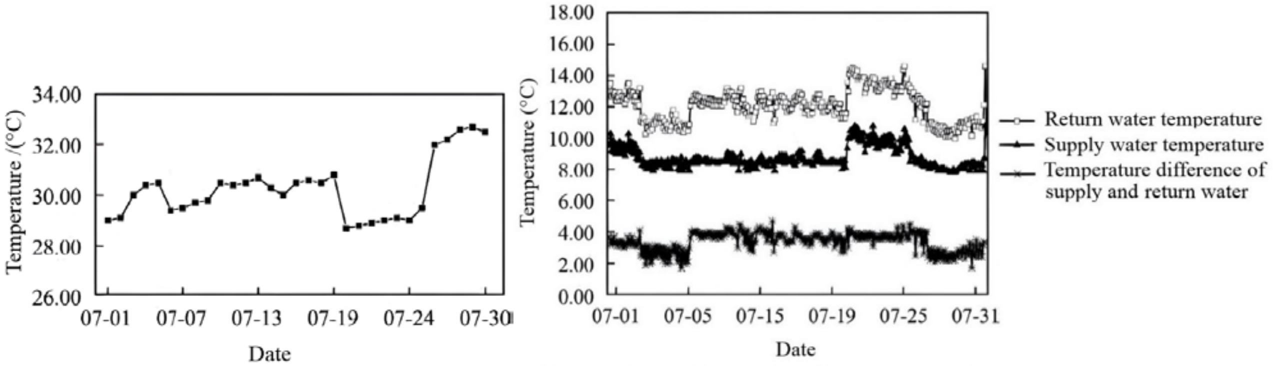

(a) Outdoor temperature (b) Temperature and temperature difference at user side

Figure 1. Summer outdoor mean temperature and temperature and temperature difference of supply and return water at user side.

Figure 2 shows the temperature and temperature difference between the supply and return water at the ground source side. The water supply temperature at the ground source side is between 31.00 and 36.00 ℃, the temperature of the return water is between 28.70 and 33.00 ℃, and the average temperature difference between supply and return levels is 3.16 ℃. The fluctuation range of outdoor temperature is small. Due to the heat storage of soil, the water supply and return temperature at the ground source side basically remains unchanged. When the outdoor temperature fluctuates greatly, such as the outdoor temperature rises to 32.00 ℃ from July 25 to 31, the building cooling load increases sharply, and the heat discharged into the soil also increases. The water supply and return temperature at the ground source side is a mirror image of the outdoor temperature. The water supply and return temperature at the ground source side shows a very obvious periodic intermittent change. During the system shutdown period, the soil temperature has a strong recovery ability, which can better alleviate the soil heat accumulation effect around the buried pipe, ensure the heat exchange capacity of the soil and the buried pipe heat exchange system, and meet the cooling capacity of the system. With the increase of operation time, the recovery ability of soil temperature decreases slightly, causing the supply and return water temperature at the source side to rise slowly.

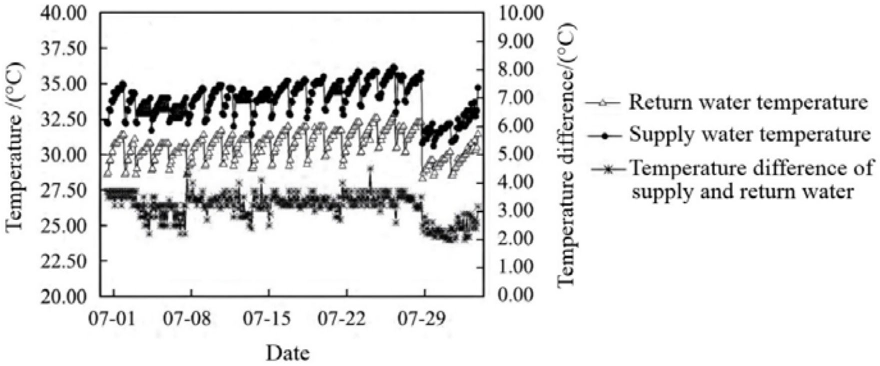

Figure 2. Temperature and temperature difference of supply and return water at source side in summer.

In areas hot in summer and cold in winter, the occupancy rate of buildings directly affects the system load rate. The operation strategy selected by the composite ground source heat pump system according to the system load rate directly affects the building energy consumption and building energy saving rate. **Figure 3** shows the load rate of the heat pump unit, system load rate, and total daily power consumption. During the whole refrigeration test of the ground source heat pump system, the system load rate is below 30.00%, but the unit load rate is 70.00% ~ 90.00%, and the total daily power consumption is between 2,800 and 5,000 kW·h. On July 16, the total daily power consumption increased due to the long operation time of the system and the increase of the system load rate on July 24.

According to the *Requirements of the Evaluation Standard for Renewable Energy Building Application Engineering*[14] and *The Guidelines for Energy Efficiency Evaluation of Renewable Energy Technology Application in Civil Buildings in Guangxi*[15], the load rate of the unit should reach more than 80.00% of the rated value, and the load rate of the system should reach more than 60.00% of the design value. The load rate of the heat pump unit meets the requirements of the evaluation guidelines. Zhu[16] studied that under the condition of extremely low occupancy (below 30.00%), the heat pump system adopts the best control strategy of single buried pipe operation, and the total energy consumption of the system is the lowest. Due to the low occupancy rate of the actual use of the building, the system load rate is below 30.00% in summer. Only the ground pipe heat pump system is operated, and the geothermal system is equipped with 37 heat pump units. 3 ~ 8 heat pump units are started and stopped according to the return water temperature at the user side, which can well meet the requirements of the unit load rate and reduce the daily power consumption of the system.

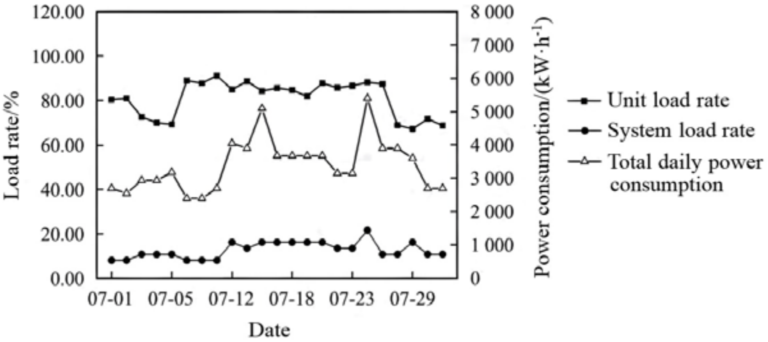

Figure 3. System load rate and heat pump unit load rate in summer.

Figure 4 shows the proportion of water pump and unit power consumption in the total daily power consumption. The daily power consumption of heat pump unit is 60.00% ~ 80.00%, basically maintained at about 65.00%, and the daily power consumption of water pump is 30.00% ~ 40.00%. According to the *Research Report on the Development of Ground Source Heat Pump in China*[17], the pump energy consumption of typical domestic ground source heat pump projects under summer conditions accounts for about 34.00% of the system energy consumption. Therefore, it can be seen that the actual energy consumption proportion of pumps in this project meets the design proportion of energy consumption of transmission and distribution system. The selection and quantity of heat pump units, circulating water pumps and hot water pumps of the ground source heat pump system are reasonable, which can choose optimal start and stop strategy of heat pump units and pumps according to the cooling capacity demand of the system, so as to improve the energy efficiency ratio of geothermal system operation under low load rate conditions.

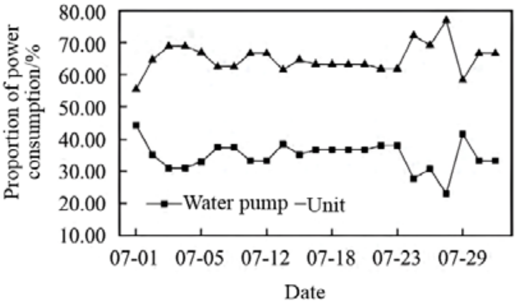

Figure 4. Power consumption ratio of water pump and unit in summer.

4.2 Operating conditions in winter

As shown in **Figure 5**, the temperature and temperature difference of water supply and return at the user's side in winter. The outdoor temperature remained at 8.00 ~ 10.00 ℃ throughout the test period, and only on January 25, the temperature suddenly fell to 5.00 ℃. The water supply temperature on the user side is 42.00 ~ 44.90 ℃, and the return water temperature is 40.00 ~ 42.50 ℃.

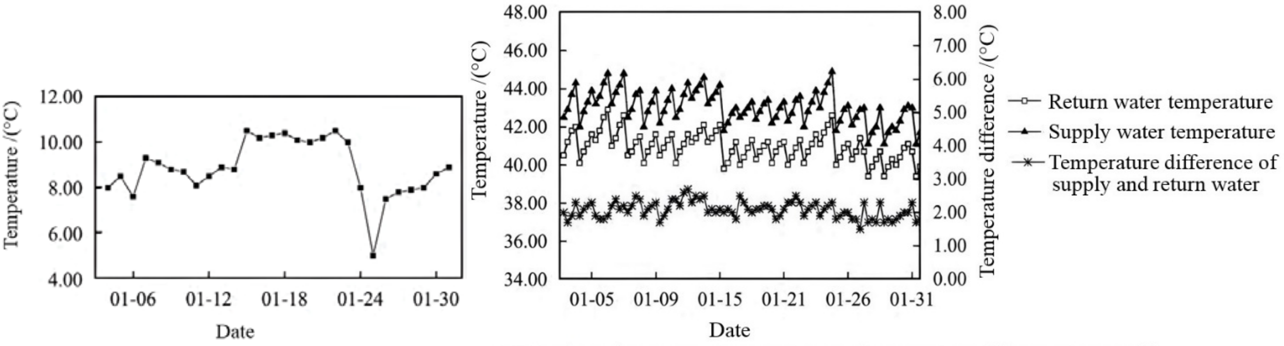

(a) Outdoor temperature (b) Supply and return water temperature and temperature difference at user side

Figure 5. Outdoor temperature in winter and temperature and temperature difference of supply and return water at the user side.

The average temperature difference is 2.00 ℃. The supply and return water temperature on the user's side fluctuates in the opposite direction with the change in the outdoor average temperature. For example, the outdoor temperature drops sharply on January 24 and 25. If the return water temperature on the user's side is lower than the set value range, increasing the number of heat pump units and water pumps, adjusting the water volume of circulating water pumps by frequency conversion, and maintaining the supply and return water temperature difference at 2.00 ℃, to increase the supply and return temperature to meet the heating demand of the system. During intermittent operation under a low load rate in winter, the supply and return water temperature on the user side show obvious periodic intermittent changes.

Figure 6 shows the supply and return water temperature at the ground source side in winter. The supply water temperature at the ground source side is 14.20 ~ 16.00 ℃, the return water temperature at the ground source side is 16.50 ~ 18.00 ℃, the supply and return water temperature difference at the ground source side is 1.70 ~ 2.50 ℃, and the average supply and return water temperature difference is 2.08 ℃. Due to the small change in outdoor temperature, the building heating capacity is relatively stable. Only on January 24 and 25, the outdoor temperature plummet, the building load increased sharply, the heat absorption of buried pipe heat exchanger increased, and the water supply temperature at the ground source side increased. The ground source heat pump system operates intermittently in winter, and the supply and return water temperature at the ground source side shows periodic intermittent changes and a slow downward trend. This is mainly because the soil temperature quickly recovers to the initial value during the system shutdown, maintaining the heat exchange capacity between the soil and the buried pipe heat exchange system. With the increase of operation time, the heat absorption gradually increases, the soil around the buried pipe forms a cold accumulation, and the heat exchange capacity of the buried pipe system decreases.

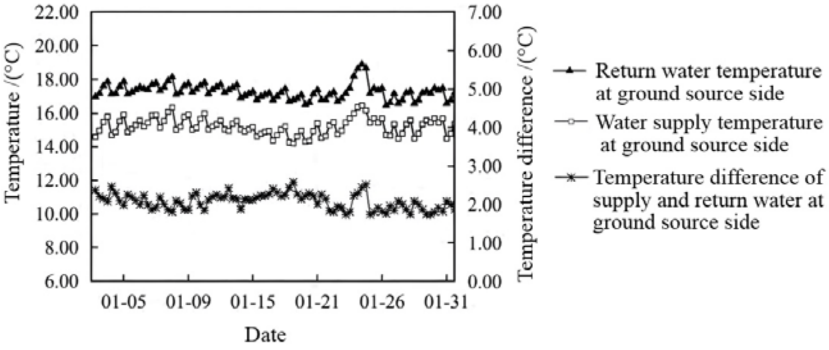

Figure 6. Temperature and temperature difference of supply and return water at source side in winter.

Figure 7 shows the unit load rate, system load rate, and total daily power consumption. When the system load rate is less than 30.00% and the unit load rate is maintained at 70.00% ~ 80.00%, the total daily power consumption in January is 2,100 ~ 5,300 kW·h. Compared with the total power consumption in July in summer, the total power consumption in winter increased by 20,670 kW·h. January was at the end of the year when the increased summary meeting and energy consumption of hot water supply cause the average total energy consumption in January to increase compared with July. **Figures 5** and **6** show that the fluctuation of outdoor temperature and supply and return water temperature difference in January is relatively small, but the range of daily total power consumption in January fluctuates significantly, which is mainly due to the increase of daily total power consumption caused by the increased performances in the grand theater, and summary meetings, the number of unit water pumps to start, the increase of system operation time and other reasons at the beginning of January, which is in line with the actual energy application.

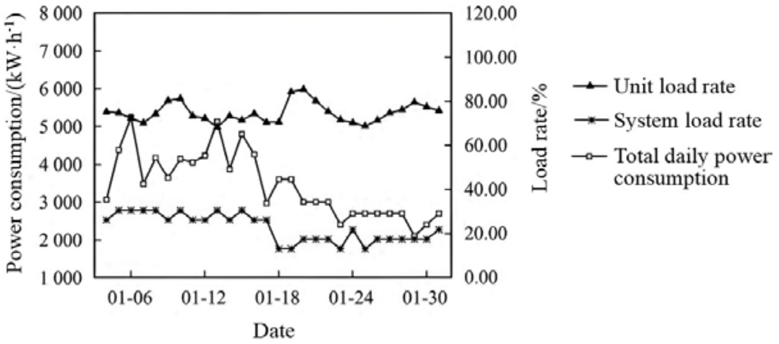

Figure 7. System load rate, heat pump unit load rate and total daily power consumption in summer.

Figure 8 shows that the power consumption of heat pump units and water pump heat pump units accounted for 55.00% ~ 75.00% and 25.00% ~ 44.00%, respectively, in January under low load operation conditions, both of which show little fluctuation. *The research report on the development of ground source heat pump in China* points out that the energy consumption of water pumps tested in the winter of domestic typical ground source heat pump system projects accounts for about 28.00% of the system energy consumption. Therefore, it can be seen that the actual proportion of water pump energy consumption under low load operating conditions meets the standard of typical demonstration projects of ground source heat pump system in Guangxi, but it is slightly higher than the requirements of the Research Report on the development of ground source heat pump. There may also be errors in the measurement of electricity due to the magnification of electric meters, leading to an error in the proportion of power consumption between the water pump and the unit.

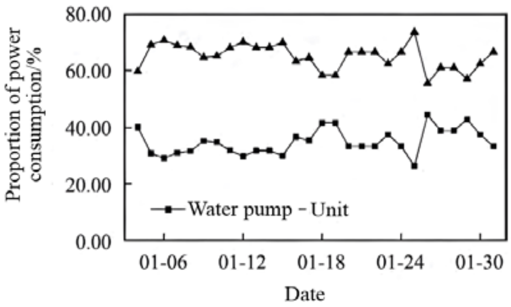

Figure 8. Power consumption ratio of water pump and unit in winter.

5. Analysis of system operation performance and energy saving rate

5.1 System operation performance analysis

It can be seen from the work of Huang and Liu[12] that with the gradual increase of the unit load rate R, the cooling performance coefficient COP of the unit increases. The random forest algorithm is used to sort the factors affecting the performance coefficient of the unit according to the importance of the mean square error Δ_{MSE} value, as shown in **Table 2**. The unit load rate R ranks first in importance, followed by the return water temperature on the ground source side under cooling conditions or the return water temperature on the user side under heating conditions, and the outdoor temperature and humidity ranks last. According to Yan *et al.*[11], with the increase of unit and system load rate, COP_{sys} increases. When the long-term system load rate is less than 30.00% based on the back-propagation network algorithm, and $R > 60.00\%$ only accounts for 30.00%, COP_{sys} and EER_{sys} are both less than 2.30. From the analysis of the influencing factors of the geothermal system, it can be seen that other influencing factors except the system load rate comply with the technical specifications of the ground source heat pump project, and only the system load rate is far from the requirements of the energy efficiency evaluation guidelines. The following will mainly study the impact of the system load rate and unit load rate on the system operation performance.

The *COP* of the local source heat pump system is 4.00 ~ 5.00, the average *COP* is 4.48, the COP_{sys} is 3.40 ~ 4.00, and the average COP_{sys} is 3.59, as shown in **Figure 9**. According to the actual *COP*, COP_{sys} and the *evaluation standard for application of renewable energy in buildings*, the ground source heat pump project can still be at level 2 energy efficiency under the conditions of system load rate <30.00% and unit load rate >80.00%. The changes of *COP* and COP_{sys} are less affected by the system load rate R_{sys}, and increase with the increase of unit load rate *R*.

As shown in **Figure 10**, in winter, when the system load rate is <30.00% and the unit load rate is about 70.00%, the unit heating performance coefficient *EER* is 3.78 ~ 4.70, the average *EER* is 4.26, the system heating energy efficiency ratio EER_{sys} is 3.07 ~ 3.70, the average EER_{sys} is 3.31, and the operation energy efficiency level is level 2. *EER* and EER_{sys} are less affected by the system load rate, which decreases with the decrease of unit load rate and increases with the increase of unit load rate. Therefore, when the load rate of the system in the early operation of the actual geothermal project is less than 30.00% for several years, the design scheme of the ground source heat pump system is set up so that the buried pipe heat exchange system can operate in different areas. The number of heat pump units equipped can select the appropriate number of operating units according to the actual building load, so that the load rate of the units can be maintained at around 80.00%, and the control strategy of heat pump units and water pump groups can be optimized to make the supply and return water temperature at the ground source side, the supply and return water temperature at the user side and the temperature difference, meet the requirements of engineering technical specifications and improve the system operation energy efficiency ratio of ground source heat pump system.

5.2 comparative analysis of unit and system performance

In order to better analyze the operation performance of the ground source heat pump system under low load rate, the unit performance coefficient and system performance coefficient tested by the geothermal research platform system of Guangxi Key Laboratory of energy conservation in Guilin in the work of Zeng *et al.*[4] and Zeng, Zhao, Lv, *et al.*[18] are compared with this project, as shown in **Figure 11**. Under the same climatic environment and karst geological conditions, the *COP* (4.48) of the project operating under low load rate conditions in summer is 4.28% higher than that of the geothermal experimental platform under normal operating conditions (4.30), and the *EER* (4.26) in winter is 18.99% higher than that of the geothermal experimental platform (3.58). In order to better study the feasibility, operating energy efficiency and energy saving rate of ground source heat pump system in karst areas, the average unit performance coefficient of 33 ground source heat pump demonstration projects in Wuhan where is hot in summer and cold in conducted by Yan *et al.*[10] is compared with this project, as shown in **Figure 11**. The *COP* (4.48) of the project in summer is 18.84% lower than the average value (5.52) of geothermal demonstration projects in Wuhan, and the *EER* of the two regions in winter is basically the same. Because the design of the buried pipe heat exchange system, the control mode of the air conditioning system, the operation management and maintenance of the experimental platform are quite different from the actual engineering projects, this paper will no longer compare with the experimental test data.

Table 2. Ranking of influence factors of heat pump unit

Influence factor	**Refrigeration condition**		**Heating condition**		**Comprehensive ranking**
	Δ_{MSE}	**Importance ranking**	**Δ_{MSE}**	**Importance ranking**	
Unit load rate	60.54	1	75.64	1	1
Return water temperature at ground source side	45.14	2	37.60	3	2
Return water temperature at user side	41.63	4	54.07	2	3
Water supply temperature at ground source side	44.65	3	24.79	5	4
Water supply temperature at user side	21.05	6	26.75	4	5
Outdoor temperature	31.30	5	16.64	6	6
Outdoor humidity	27.52	7	11.56	7	7

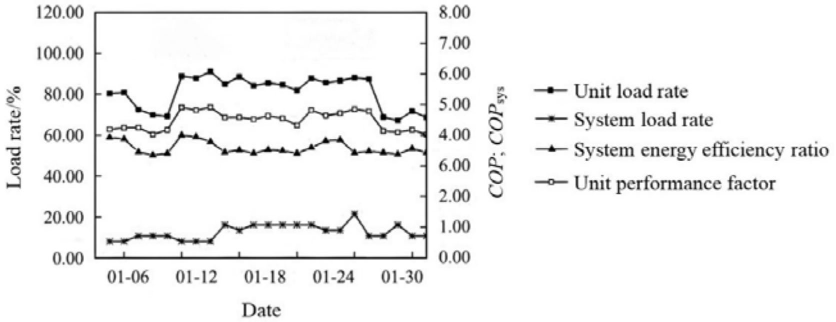

Figure 9. Load rate and performance coefficient of heat pump unit and load rate and energy efficiency ratio of system in summer.

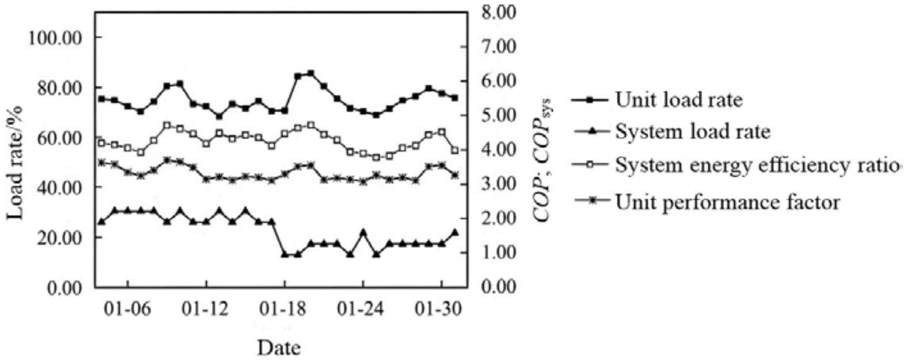

Figure 10. Load rate and performance coefficient of heat pump unit and system in winter.

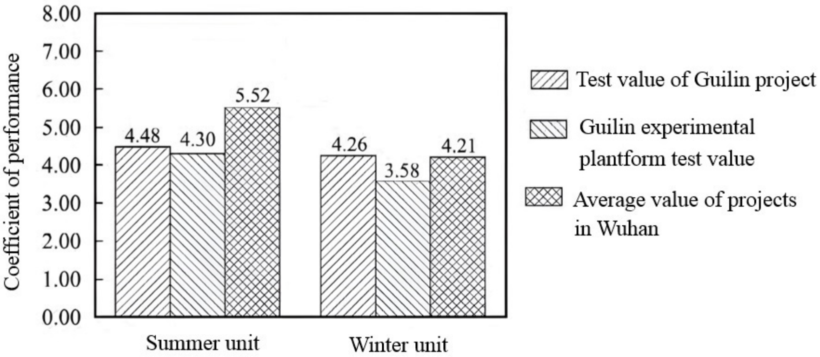

Figure 11. Comparison of unit performance coefficient.

The system energy efficiency ratio (COP_{sys}) of the project under low load rate operation in summer is 3.59, which is 8.79% higher than that of Wuhan COP_{sys} 3.30, and the system energy efficiency ratio (EER_{sys}) in winter is equal to the average EER_{sys} of Wuhan, as shown in **Figure 12**. It can be seen that the project can achieve high system energy efficiency ratio under the working condition of system load rate <30.00%, is due to the reasonable design of buried pipe heat exchange system, system equipment selection and quantity allocation, unit pump group control strategy and operation management. The karst area is particularly rich in groundwater resources, and the groundwater level is low, which can well enhance the heat exchange capacity of buried pipes and play an important role in improving the energy efficiency ratio of system operation.

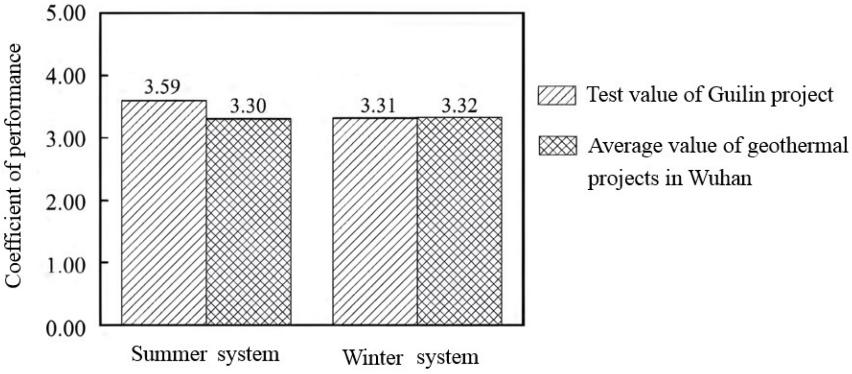

Figure 12. Comparison of system performance coefficient.

6. Conclusion

Based on the measured data of Guilin ground source heat pump demonstration project under karst geological conditions, this paper analyzes the operating parameters and effects of ground source heat pump system from the order of importance of factors affecting the operating performance of ground source heat pump system and heat pump unit, and draws conclusions.

In summer, the average water supply temperature on the user side is 8.50 ℃, the average return water temperature is 12.14 ℃, the average water supply temperature on the ground source side is 34.70 ℃, and the average return water temperature is 31.44 ℃. In winter, the average water supply temperature on the user side is 43.10 ℃, the average return water temperature is 40.99 ℃, the average water supply temperature on the ground source side is 15.14 ℃ the average return water temperature is 17.22 ℃, and the whole ground source heat pump system is in good operation.

(1) When the system load rate is <30.00% and the unit load rate is >70.00% under typical seasonal conditions, due to the reasonable system design, the total daily power consumption is less affected by the system load rate, and decreases with the increase of the unit load rate. The power consumption of the unit in summer accounts for 60.00% ~ 80.00%, the power consumption of the water pump accounts for 30.00% ~ 40.00%, the power consumption of the unit in winter accounts for 55.00% ~ 75.00%, and the power consumption of the water pump accounts for 25.00% ~ 44.00%. The proportion of power consumption of pumps and units is in line with the provisions of the *Research report* on the *Development* of *ground source heat pump in China*.

(2) The average *COP* in summer is 4.48, the average COP_{sys} is 3.59, and the average *EER* in winter is 4.26, and the average EER_{sys} is 3.31, belonging to level 2 energy efficiency. If the buried pipe heat exchange system can be operated in different areas, the selection and quantity of heat pump units and water pump equipment can be selected according to the actual building load, and the optimal pump start and stop strategy of heat pump units can be adopted to ensure that the unit load rate reaches 80.00%, the unit performance coefficient can reach more than 4.00, and the system operation energy efficiency ratio can reach more than 3.30.

(3) The *COP* of the ground source heat pump system of the project in summer is 4.28% higher than that of the experimental platform in Guilin, and the *EER* in winter is 18.99% higher; *COP* in summer is lower than that of geothermal projects in Wuhan, and *EER* in winter is basically the same; the average COP_{sys} in summer is 8.79% higher than that in Wuhan, and the average EER_{sys} in winter is

the same. The energy-saving rate of the ground source heat pump system of the project is 30.72% in summer and 35.93% in winter, which is only 9.54% lower than that of the geothermal project in Wuhan in summer and 4.14% lower than that in winter. Although the system load rate is lower than 30.00%, the energy-saving rate in typical seasons is not much different, and it still maintains a high energy-saving rate compared with the conventional air-conditioning system.

It can be seen from the conclusion that when the ground source heat pump system is under partial load condition under karst geological conditions in Guilin, the high-efficiency and energy-saving characteristics of the ground source heat pump system can still be achieved by operating part of the buried pipe heat exchange system and implementing the linkage group control strategy of the heat pump unit and the water pump to ensure that the load rate of the heat pump unit is about 80.00%. When the system load rate reaches more than 60.00%, the energy-saving effect of the system will be more significant, which is conducive to the promotion and application of ground source heat pump system in Guilin.

Conflict of interest

The authors declare that they have no conflict of interest.

References

1. Li Y, Wang Y. Present situation and trend of ground source heat pump technology in China. Industry Observation 2009; (5): 38–39.
2. Wang L, Gao W. The relationship between groundwater activity and karstic collapse in the western regions of Guilin. Journal of Guilin Institute of Technology 2000; 20(2): 106–111.
3. Dong Y, Wang L, Zeng Z, *et al*. The research on heat transfer performance of the continuous and intermittent operation condition of ground heat exchangers. Renewable Energy Resources 2014; 32(11): 1687–1693.
4. Zeng Z, Zhao Y, Lyu H, *et al*. Experimental study on operation modes impact on heat exchange performance of ground heat exchanger. Renewable Energy Resources 2016; 34(5): 737–744.
5. Zeng Z, Lyu H, Zhao Y, *et al*. Numerical stimulation of effect of ground water seepage on vertically buried tubular heat exchanger. Acta Energiae Solaris Sinica 2015; 36(12): 3007–3014.
6. Guo C, Du Q, Ma J, *et al*. Research on the influence of ground heat exchanger partition operating on soil heat accumulation. Journal of Thermal Science and Technology 2018; 17(4): 259–266.
7. Wang L, Xu Y. Operating characteristics of ground source heat pump system in non-equilibrium cooling and heating load. Journal of Thermal Science and Technology 2016; 15(2): 154–159.
8. Li H, Xu W, Wu J, *et al*. Operation performance analysis of ground source heat pump system in certain nearly zero energy building based on actual measurement data. Building Science 2015; 31(6): 124–130.
9. Wang E, Shen Y, Chen Y, *et al*. Study on the utilization mode of double buried pipe groups of solar-ground source heat pump system. Journal of Thermal Science and Technology 2020; 19(2): 103–109.
10. Yan L, Hu P, Peng B, *et al*. Research on assessment of ground source heat pump demonstration project in Wuhan. Building Science 2014; 30(12): 25–29.
11. Yan L, Hu P, Li C, *et al*. The performance prediction of ground source heat pump system based on monitoring data and data mining technology. Energy and Buildings 2016; 127: 1085-1095.
12. Huang X, Liu C. Performance test and analysis of ground source heat pump system based on data mining. Journal of Engineering for Thermal Energy and Power 2020; 35(3): 181–186.
13. Ministry of Housing and Urban-Rural Development of the People’s Republic of China. Technical code for ground-source heat pump system. Chinese patent. GB 50366-2009. 2009 Jun 1.
14. Ministry of Housing and Urban-Rural Development of the People’s Republic of China. Evaluation standard for application of renewable energy in buildings. Chinese patent. GB/T50801-2013. 2013 May 1.
15. Department of Housing and Urban-Rural Development of Guangxi Zhuang Autonomous Region. Guidelines for energy efficiency evaluation of renewable energy technology application in civil buildings in Guangxi. Available from: https://www.taodocs.com/p364030473.html.
16. Zhu L, Shi Y, Zhang X, *et al*. Analysis of operation strategies of residential Hybrid ground-coupled heat pump system on different occupancy rate. Fluid Machinery 2016; 44(3): 76–79.
17. Xu W. Research report on ground-source heat pump development in China. Beijing: China Construction Industry Press; 2013.
18. Zeng Z, Zhao Y, Lv H, *et al*. Heat and moisture migration in soils around ground heat exchangers under heating operation of ground source heat pump. Chinese Journal of Geotechnical Engineering 2017; 39(1): 145–150.

Thermal Science and Engineering (2021) Volume 4 Issue 2
doi:10.24294/tse.v4i2.1516

ORIGINAL RESEARCH ARTICLE

Study on heat transfer characteristics of flow heat coupling of horizontal spiral tube heat exchanger

Qingwen Yue, Xide Lai*, Xiaoming Chen, Ping Hu

School of Energy and Power Engineering, Xihua University, Chengdu 610039, China. E-mail: laixd@mail.xhu.edu.cn

ABSTRACT

In view of the complex structural characteristics and special operating environment of the horizontal spiral tube heat exchanger of the shaft sealed nuclear main pump, the numerical simulation method of flow heat coupling is used to analyze the influence of the flow and temperature changes of the fluid on the shell side on the flow field and temperature field of the heat exchanger, explore the influence rules of the inlet parameters on the flow and heat transfer characteristics of the fluid in the heat exchanger, and analyze the enhanced heat transfer performance of the heat exchanger by using the relevant heat transfer criteria. The results show that the horizontal spiral tube fluid generates centrifugal force under the influence of curvature, forming a secondary flow which is different from the straight tube flow heat transfer, and the velocity distribution is concave arc, which will enhance the heat transfer efficiency of the heat exchanger; with the increase of shell side velocity, the degree of fluid disturbance and turbulence increases, while the pressure loss does not change significantly, and the heat transfer performance of the heat exchanger increases; under the given structure and size, the heat transfer performance curve of the heat exchanger shows that the increase of shell side flow and Reynolds number has a significant impact on the enhanced heat transfer of the spiral tube. In practical engineering applications, the heat transfer can be strengthened by appropriately increasing the shell side flow of the heat exchanger.

Keywords: Shaft Seal Nuclear Main Pump; Horizontal Spiral Tube Heat Exchanger; Coupled Heat Transfer; Numerical Simulation; Performance Analysis

ARTICLE INFO

Received: 6 Jane 2021
Accepted: 31 August 2021
Available online: 10 September 2021

1. Introduction

Horizontal spiral tube heat exchanger has the advantages of compact structure, large heat exchange area, high temperature resistance and strong pressure bearing capacity. It is widely used in nuclear reactors, environmental engineering, power production and other engineering fields[1,2]. In the primary circuit system of the nuclear island, the spiral tube heat exchanger is installed above the impeller of the nuclear main pump, the only rotating equipment, to prevent the heat of the reactor high-temperature coolant from transmitting to the upper part of the pump and prevent the heat damage of the pump bearing and shaft seal. It can be seen that the heat transfer characteristics of the spiral tube heat exchanger directly affect the safe operation of the main pump, so it is necessary to analyze the flow and heat transfer characteristics of the heat exchanger more systematically and accurately. There are many factors that affect the flow and heat transfer of the heat exchanger. Reasonable geometric parameters, flow, temperature and working environment play an important role in improving the heat transfer efficiency of the heat exchanger and ensuring the safe operation of the unit.

At present, scholars at home and abroad have made in-depth research and elaboration on the influencing factors of flow and heat transfer in spiral tubes. For example, Vocale[3] considered the coupled heat transfer of spiral tubes and evaluated the influence of the selection of thermal boundary conditions on the local heat transfer phenomenon in coils. Ren[4], Lu[5] and Zeng *et al.*[6] analyzed the influence of different boundary conditions and different geometric parameters on the conjugate heat transfer of spiral tube heat exchangers, and concluded that curvature, pipe diameter and grid thickness are the main factors for the optimal design of heat exchangers. Sun[7] and Yu[8] explores the shell side flow and heat transfer characteristics of spiral wound heat exchangers in floating liquefied natural gas, including experimental research on the influence of tilt, yaw and pitch on the pressure drop of spiral wound heat exchangers. Chen *et al.*[9], Guo *et al.*[10] and Yu[11] studies the properties of forced convection heat transfer of helical tubes under different conditions, and obtains the distribution of local heat transfer coefficient and the empirical formula of average heat transfer coefficient under different conditions. Most of the above studies are aimed at analyzing the heat transfer characteristics of the heat exchanger in a specific working environment. For the horizontal spiral tube heat exchanger of the nuclear main pump, the high temperature and high-pressure operating environment in the pump needs higher requirements for the performance of the spiral tube heat exchanger. The research on the inlet parameters and comprehensive performance evaluation of the shell side needs to be deepened.

In view of the complexity of the fluid flow field and heat transfer process in the horizontal spiral tube heat exchanger, considering the conjugate heat transfer under the joint action of the convective heat transfer of the fluid medium and the heat conduction of the tube wall, this paper uses the numerical simulation method to comprehensively analyze the heat transfer performance of the spiral tube heat exchanger under different flow rates and different heat source temperatures on the shell side, and uses the relevant heat transfer criteria to analyze the comprehensive energy transfer performance of the heat exchanger. It provides some guidance for solving the problems of heat transfer of the heat shield heat exchanger of the shaft seal nuclear main pump.

2. Structure and model parameters of spiral tube heat exchanger

The heat exchanger of the main pump is composed of 8 groups of cooling coils located inside the heat shield cover. Each group of cooling coils is coiled by a single cooling pipe according to the spiral, and is stacked in the heat shield cover cylinder in turn. The temperature difference of each component changes greatly, and the physical parameters of materials and media change significantly with temperature. At the same time, the structural characteristic scale span of the heat exchanger is large, and the shell side channel is narrow. These factors make the heat transfer numerical simulation of the main pump heat shield heat exchanger become very complex. In order to save calculation time and resources, the solid model of spiral tube heat exchanger is reasonably simplified, and a group of horizontal spiral tubes are taken for numerical simulation research. The simplified model is shown in **Figure 1**.

The flow and heat transfer of two spiral tubes are selected for numerical analysis. In order to ensure the full development of turbulence and make it closer to the boundary conditions of the real flow field, the fluid domain at the outlet of the spiral tube shell side is appropriately extended. The calculation domain model is shown in **Figure 1(a)**. The cooling water in a single spiral pipe enters from the right side of the coil, gradually rises to the upper level after heat exchange through the lower coil, and then continues heat exchange, and finally flows out from the left spiral pipe. The spiral pipe is composed of two layers of concentric spiral coil, which is made of stainless-steel pipe with a diameter of 19 mm bent into a spiral shape. Each layer of steel pipe is bent for seven turns. The geometric model of the coil is shown in **Figure 1(b)**, and the basic parameters are shown in **Table 1**.

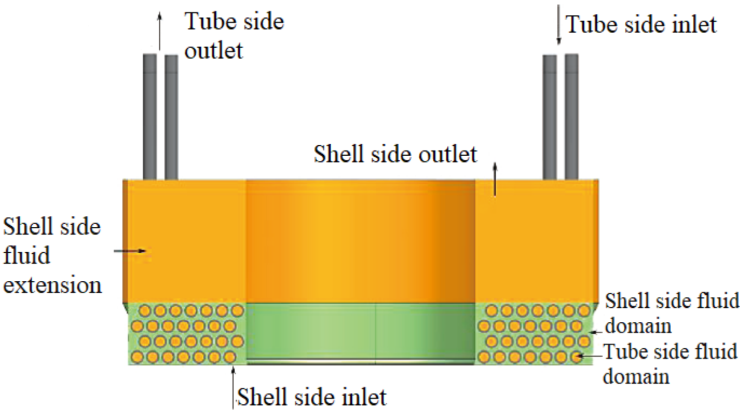

(a) Calculation domain model of spiral tube heat exchanger

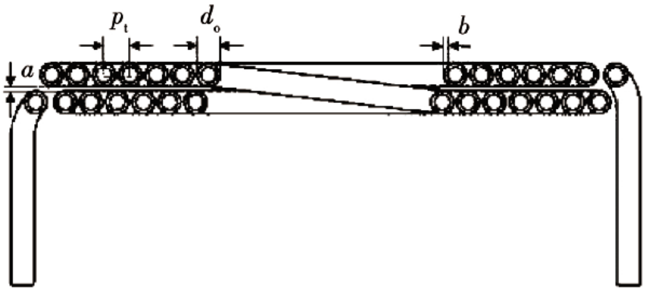

(b) Horizontal spiral coil structure

Figure 1. Schematic diagram of horizontal spiral tube heat exchanger.

Table 1. Geometric parameters of horizontal spiral tube

Parameter	**Value**
Length of heat transfer tube L/m	19
Pipe inner diameter d_i/mm	12.8
Tube outer diameter d_o/mm	19
Screw diameter d_h/mm	473.5
Wall thickness of heat transfer tube b/mm	3.1
Heat transfer tube spacing a/mm	2.5
Heat transfer tube pitch P_t/mm	21.5

3. Numerical calculation method

3.1 Grid division and boundary conditions

The structure of the fluid domain on the shell side of the spiral tube heat exchanger is complex, and the unstructured tetrahedral mesh with strong self-adaptive is used to divide its calculation domain. In order to ensure the calculation accuracy, the calculation domain of the main heat exchange zone on the shell side is encrypted. Considering the calculation equipment and calculation cycle, the total number of grids of the model is about 16 million after the grid independence test. The mesh division of fluid domain of heat exchanger is shown in **Figure 2**.

High temperature water and cooling water are used for heat exchange at shell side and tube side respectively. In view of the large temperature difference of each component and the obvious change of the physical parameters of the medium with the temperature, in order to obtain more accurate calculation results, considering that the physical parameters of the fluid will change with the temperature, thus affecting the heat transfer, the material physical variable function is added to CFX-Pre, and the physical parameters of the spiral tube metal material are shown in **Table 2**. The inlet of the working medium is the mass flow and temperature boundary condition, and the outlet is the static pressure boundary condition. The interface between the spiral coil and the fluid domain is set as the heat flow coupling interface, and the other outer walls are set as the non-slip insulation wall. The parameter settings of boundary conditions are shown in **Table 3**.

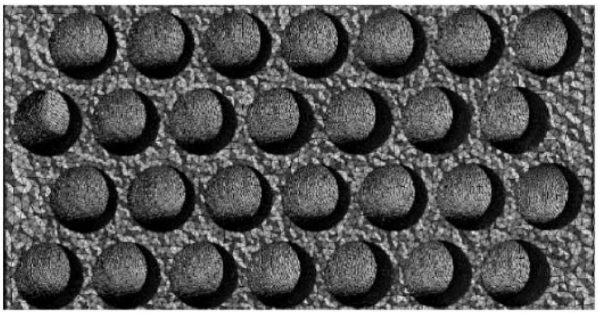

(a) Mesh generation of fluid domain on shell side

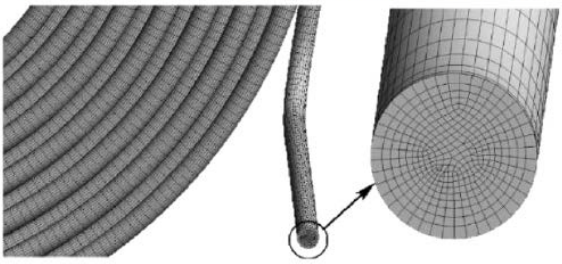

(b) Mesh generation of fluid domain on tube side

Figure 2. Schematic diagram of the fluid domain grid for spiral tube heat exchanger.

Table 2. Thermophysical properties of spiral tube

Material	**Density/kg·m^{-3}**	**Constant pressure specific heat capacity/J·kg^{-1}·°C^{-1}**	**Thermal conductivity/w·m^{-1}·°C^{-1}**
Austenitic stainless steel	7,930	502	19

Table 3. Boundary condition setting parameters

Boundary condition	**Import**		**Export**
	Flow/L·h^{-1}	**Temperature/°C**	**Static pressure/MPa**
Tube side	11,000	38	0.1
Shell side	600 ~ 1,800	150 ~ 290	0.1

3.2 Calculation method

In the process of fluid flow research, the computational domain is discretized based on the finite volume method. In order to solve the momentum and energy equations, the discrete format adopts high resolution, and the continuity equation, momentum equation and energy equation formed a control equation group for solving turbulent flow and heat transfer.

Continuity equation:

$$\frac{\partial \rho}{\partial t} + \nabla \cdot (\rho U) = 0 \tag{1}$$

Momentum equation:

$$\frac{\partial (\rho U)}{\partial t} + \nabla \cdot (\rho U U) = - \nabla p + \nabla \tau + S_{\mathrm{M}} \tag{2}$$

Energy equation:

$$\frac{\partial(\rho h_{tot})}{\partial t} - \frac{\partial \rho}{\partial t} + \nabla \cdot (\rho U h_{tot}) = \nabla \cdot (\lambda \nabla T) + \nabla \cdot (U_{\tau}) + U \cdot S_M + S_E \tag{3}$$

Among them, the total enthalpy h_{tot} is related to the static enthalpy $h(T,p)$:

$$h_{\mathrm{tot}} = h + \frac{1}{2} U^2 \tag{4}$$

Where: ρ—density, kg·m^{-3}; ∇—divergence; t

—time, s; U—velocity vector; τ—viscous stress, which is produced by the viscous action of molecules; p—pressure on fluid microelement, Pa; S_M—generalized source term; T—temperature, K; λ—second viscosity; $\nabla \cdot (U \cdot \tau)$—viscous stress does work; $U \cdot S_M$ work for external momentum heat source.

The flow velocity in the inner shell side and tube side of the spiral tube heat exchanger is small, and the pressure gradient is relatively small, so k-ε turbulent model is used to study the heat transfer and fluid characteristics of spiral tube heat exchanger[12]. The solution equation is as follows:

$$\frac{\partial(\rho k)}{\partial t} + \frac{\partial(\rho k u_i)}{\partial x_i} = \frac{\partial}{\partial x_j}\left[\left(\mu + \frac{\mu_i}{\sigma_k}\right)\frac{\partial k}{\partial x_j}\right] + G_k - \rho\varepsilon \tag{5}$$

$$\frac{\partial(\rho k)}{\partial t} + \frac{\partial(\rho\varepsilon)}{\partial t} + \frac{\partial(\rho\varepsilon u_i)}{\partial t} = \frac{\partial}{\partial x_j}\left[\left(\mu + \frac{\mu_i}{\sigma_\varepsilon}\right)\frac{\partial\varepsilon}{\partial x_j}\right] + \frac{C_{1\varepsilon}\varepsilon}{k}G_k - C_{2\varepsilon}\rho\frac{\varepsilon^2}{k} \tag{6}$$

Where: ε—turbulent dissipation rate; G_k—generation term of turbulent kinetic energy k caused by average velocity gradient, $\sigma_k, \sigma_\varepsilon, C_{1\varepsilon}, C_{2\varepsilon}$ is an empirical constant, where $\sigma_k = 1.0, \sigma_\varepsilon = 1.3, C_{1\varepsilon} = 1.44, C_{2\varepsilon} = 1.92$; μ—physical parameters; μ_i—turbulent viscosity, Pa·s. CFX solver is used for steady-state calculation. When the residual errors of continuity, momentum and energy are less than 10^{-4}, 10^{-5} and 10^{-6} respectively, it is judged that the physical quantities of flow field and temperature field of heat exchanger have converged.

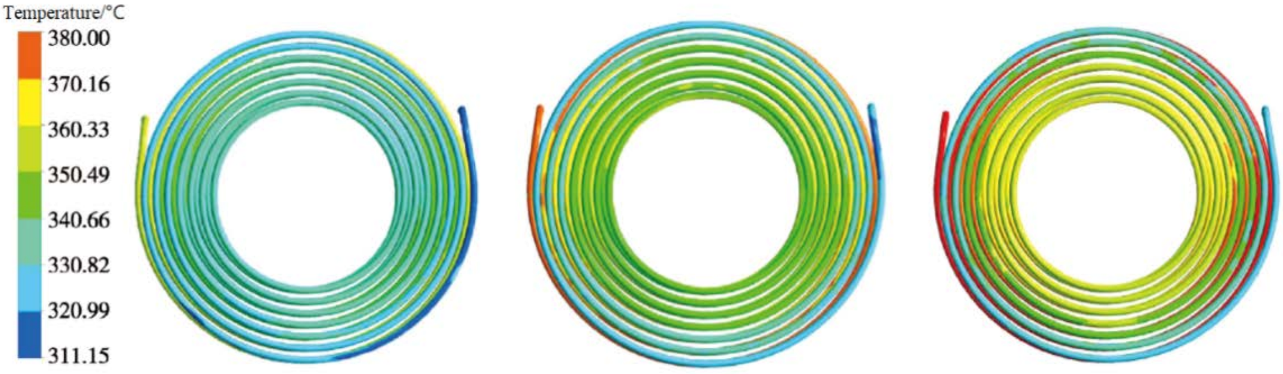

(a) Q_o=600 L/h (b) Q_o=1200 L/h (c) Q_o=1800 L/h

Figure 3. Temperature contours for lower spiral tube.

4. Calculation results and analysis

4.1 Temperature field and velocity distribution of fluid at pipe side

In order to study the influence of shell side fluid inlet parameters on the temperature distribution of fluid heat transfer, the temperature field and velocity field of fluid in spiral tube under different volume flow were numerically simulated and analyzed. By analyzing the temperature distribution nephogram of the spiral tube in **Figure 3** and **Figure 4**, it can be seen that the temperature in the lower spiral tube gradually increases from the outer ring of the coil to the inner ring, and the temperature in the upper spiral tube gradually increases from the inner ring of the coil to the outer ring. By comparing and analyzing the temperature distribution nephogram of spiral tube under different inlet flow, it can be seen that the coil temperature increases significantly with the increase of fluid flow on the shell side. Under the given structure and size, with the increase of flow rate, the surface heat transfer coefficient increases, and more heat is transferred to the spiral tube.

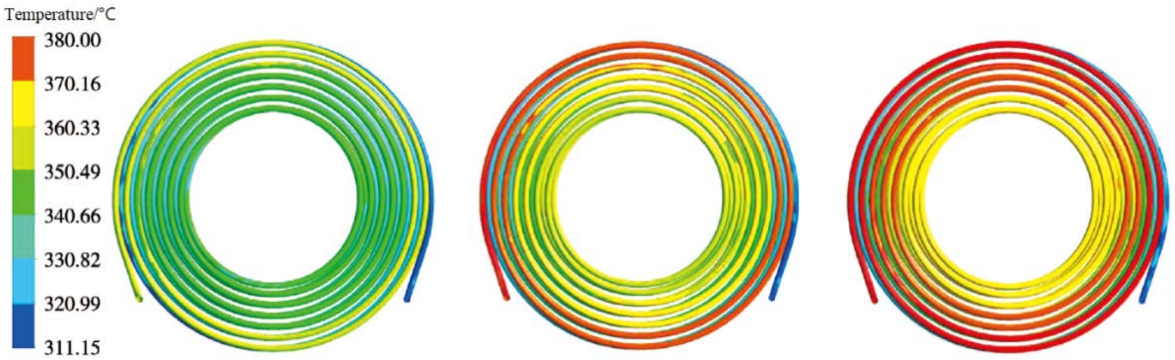

(a) Q_o=600 L/h (b) Q_o=1200 L/h (c) Q_o=1800 L/h

Figure 4. Temperature contours for upper spiral tube.

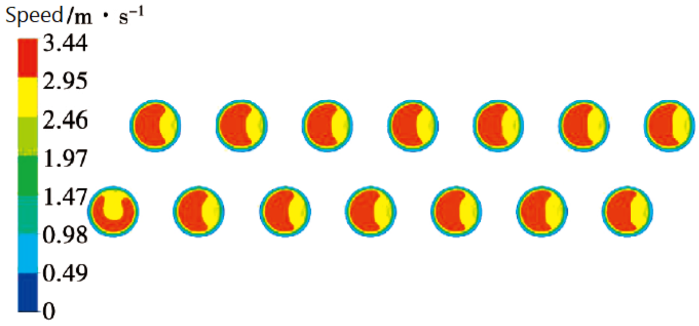

(a) Velocity distribution nephogram

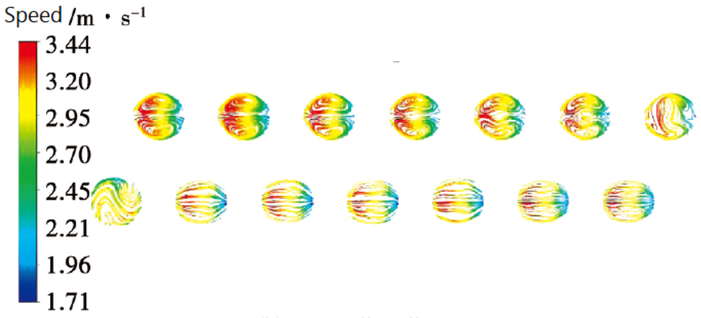

(b) Streamline diagram

Figure 5. Fluid velocity profile inside horizontal spiral tube.

In order to further understand the influence of the structural characteristics of the spiral tube on heat transfer, the velocity distribution of the spiral tube is analyzed. As the structural size of the model is large, **Figure 5** shows the velocity distribution nephogram and streamline diagram of some characteristic sections of the spiral tube. Due to the dependence of the secondary flow characteristics on the curvature of the coil, the centrifugal force generated by the bending of the spiral pipe makes the maximum velocity of the fluid close to the outside of the pipe, and the fluid flow velocity on the inner wall of the pipe is relatively small, and the velocity distribution presented the shape of concave arc. At the same time, according to the streamline diagram, the secondary flow effect of the lower coil is not obvious. When the fluid rises to the upper coil, the fluid disturbance intensifies, producing obvious secondary circulation, and enhancing the heat exchange effect of the heat exchanger.

4.2 Influence of shell side fluid inlet parameters on heat transfer characteristics of heat exchanger

Figure 6 shows the relationship of the shell side fluid heat transfer coefficient h_o and the total heat transfer coefficient K of the heat exchanger with the flow rate.

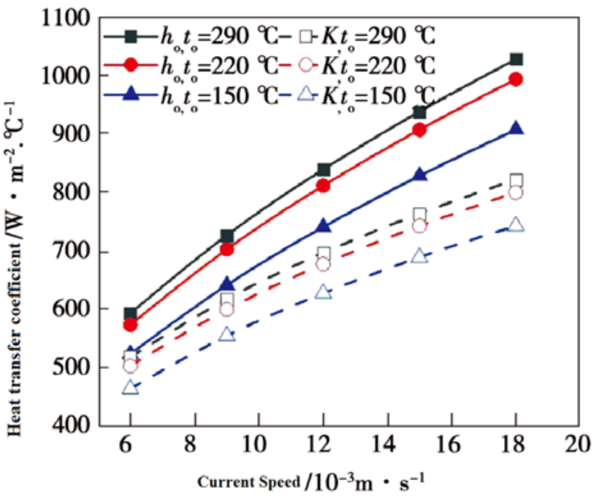

Figure 6. Heat transfer coefficient vs. flow rate of shell-side.

At different inlet temperatures, the variation trends of total heat transfer coefficient *K* and shell side fluid boundary film heat transfer coefficient h_o with the change of flow velocity are basically the same, both of which increase with the increase of shell side flow velocity *u*. Under the same shell side flow rate, the heat transfer coefficient increases with the increase of temperature, but the increase of heat transfer coefficient shows a decreasing trend. Compared with the inlet temperature of 150 ℃, the increase of total heat transfer coefficient at 220 ℃ is between 7.6% and 8.3%, and the increase value at 290 ℃ is between 2.8% and 3.0%. Therefore, improving the heat transfer coefficient of the heat exchanger by changing the inlet temperature is limited

Figure 7 shows the change curve of the heat transfer power *P* of the heat exchanger change with the shell side flow rate *u* and temperature t_o. It can be seen that with the increase of temperature, the temperature difference between the fluid inside and outside the horizontal spiral tube increases, the heat transfer per unit time increases, and the heat transfer power shows an increasing trend. The flow rate has little effect on the heat transfer power, and its change gradually decreases with the increase of flow rate.

Figure 8 shows the relationship between the pressure drop on the shell side of the heat exchanger and the flow rate. At the same flow rate, because the incompressible fluid has little dependence on pressure, the pressure drop on the shell side varies little with the fluid temperature. Although the pressure drop on the shell side gradually increases with the increase of inlet flow rate, the test flow rate is small, and the pressure drop on the shell side of the spiral tube heat exchanger does not change significantly.

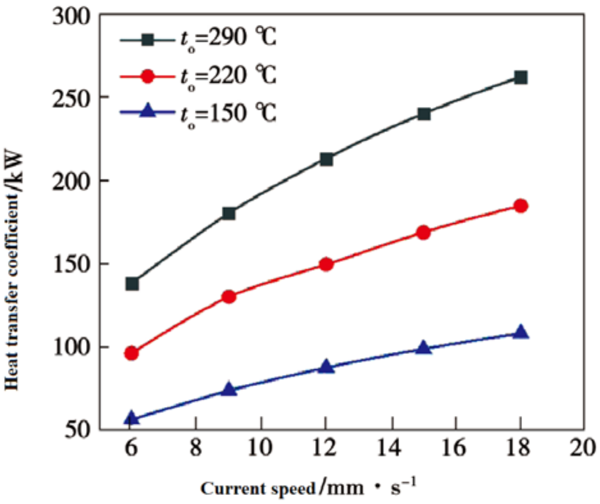

Figure 7. Heat transfer power vs. flow rate of shell-side.

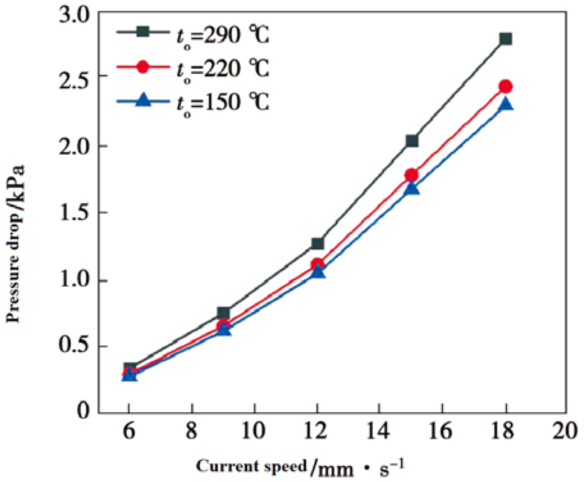

Figure 8. Pressure drop vs. flow rate of shell-side.

3.3 Comprehensive performance analysis of spiral tube heat exchanger

The flow and heat transfer of fluid in the heat exchanger is an important index to evaluate the comprehensive performance of the spiral tube heat exchanger. According to the temperature results obtained from numerical simulation research, based on the performance evaluation criteria of the first law of thermodynamics, the influence of shell side Reynolds number and temperature in the spiral tube heat exchanger on the conjugate heat transfer of the heat exchanger is analyzed.

In the comprehensive performance analysis of heat exchanger, the Nusselt number Nu_o represents the strength of the average heat transfer coefficient of the fluid, and the heat transfer factor j_H reflects the relationship between the average friction coefficient and the heat transfer coefficient of the convective heat transfer surface, and the efficiency of the heat exchanger η reflects the influence of the temperature difference between the inlet and outlet of the fluid on the heat transfer of the spiral tube heat exchanger. The expression of the number of relevant criteria is[13]:

$$Re_o = \frac{d_e G_o}{\mu_o} \tag{7}$$

$$Nu_o = \frac{h_o d_e}{\lambda_o} \tag{8}$$

$$Pr_o = \frac{c_{p,o}\mu_o}{\lambda_o} \tag{9}$$

The expression of heat transfer factor JH is[14]:

$$j_H = \frac{Nu_o}{Re_o Pr_o^{1/3}} \tag{10}$$

Where: d_e—equivalent diameter of shell side, m; λ_o—thermal conductivity of shell side fluid, W/m·K; G_o—mass flow rate of fluid at shell side, kg/(m^2·h); μ_o—hydrodynamic viscosity at shell side, PA·s; $c_{p,o}$—constant specific pressure heat capacity of shell side fluid, J/(kg·K).

The efficiency of heat exchanger is defined as[15]:

$$\eta = Q_{avg}/Q_{max} \tag{11}$$

Among them,

$$Q_{avg} = (Q_i + Q_o)/2$$

$$Q_{max} = (q_m c_p)_{min}(t_{o,in} - t_{i,in})$$

Where: Q_{avg}—average heat exchange capacity of heat exchanger, W; Q_i—heat exchange of fluid at pipe side, W; Q_0—heat exchange of fluid at shell side, W; q_m—mass flow, kg/s; $t_{i,in}$—pipe side inlet temperature, °C; $t_{o,in}$—inlet temperature at shell side, °C.

According to the analysis of the Nu_0 change curve in **Figure 9**, Nu_0 gradually increases with the increase of Re_0, and the average heat transfer coefficient of the shell side fluid gradually increases; under the same Re_0, Nu_0 increases with the increase of temperature. The temperature difference between the fluid inside and outside the tube increases, and the average heat transfer coefficient of the fluid on the shell side increases, which is conducive to the heat transfer of the fluid in the heat exchanger.

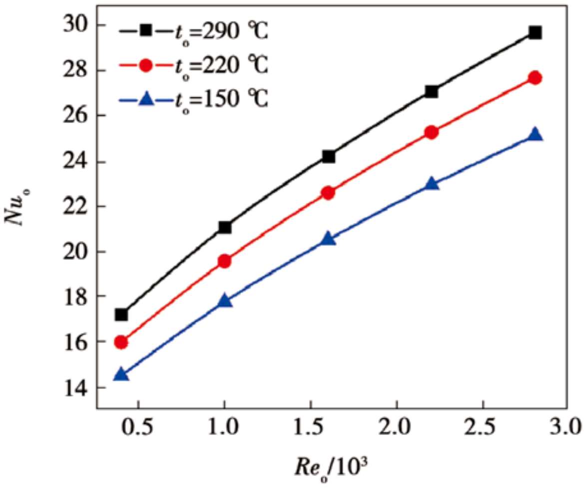

Figure 9. Nusselt number vs. Reynolds number of shell-side.

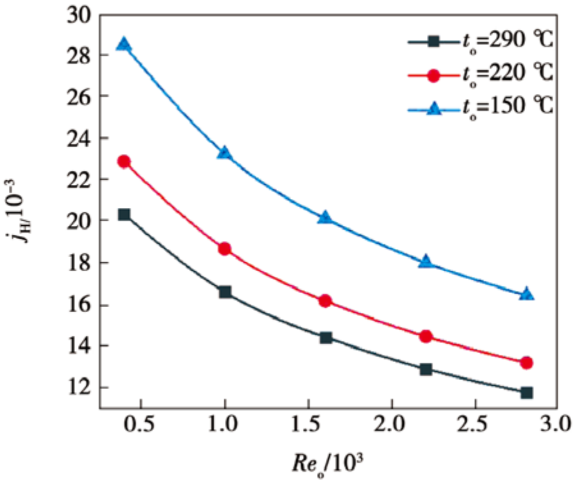

Figure 10. Heat transfer factor vs. Reynolds number of shell-side.

The heat transfer factor j_H change curve in **Figure 10** shows that j_H decreases with the increase of temperature, and the amount of change gradually decreases. This is because the physical properties of the fluid have changed significantly affected by temperature. j_H decreases gradually with the increase of Re_0, and the heat transfer coefficient of shell side fluid increases, which further improves the heat transfer performance of horizontal spiral tube heat exchanger.

Figure 11 shows the relationship between heat exchanger efficiency η and Re_0. The analysis shows that η gradually decreases with the increase of Re_0, which is attributed to the increase of q_m with the increase of Re_0, leading to the increase of Q_{max}, so the efficiency of heat exchanger η decreases. At the same time, when the flow rate is constant, the efficiency η of the spiral tube heat exchanger is slightly higher when the temperature is 220 °C, and it can be judged that the inlet temperature of the shell side has no significant effect on the enhanced heat transfer of the spiral tube.

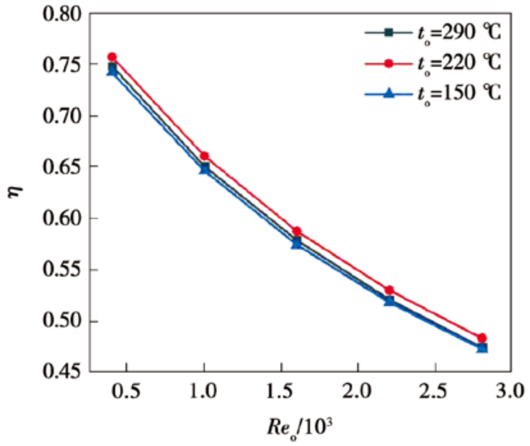

Figure 11. Efficiency vs. Reynolds number of shell-side.

5. Conclusion

(1) The fluid temperature of the spiral tube gradually increases along the flow direction, and the centrifugal force generated by its bending makes the maximum velocity of the fluid close to the outside of the tube, and the velocity is distributed in a concave arc shape. When the fluid rises to the upper coil of the spiral tube, the fluid disturbance intensifies, producing obvious secondary circulation, and enhancing the heat exchange effect of the heat exchanger.

(2) The inlet flow rate of shell side fluid is in the range of 600 ~ 1,800 L/h. With the increase of flow rate, the shell side heat transfer coefficient and total heat transfer coefficient increase by 73% and 59% respectively, which has a positive impact on the enhancement of heat transfer; the heat transfer power and pressure loss have no obvious change with the increase of fluid inlet flow on the shell side.

(3) Temperature has little effect on the heat transfer coefficient and pressure drop. The heat transfer coefficient on the shell side and the total heat transfer coefficient increased by 13% and 11% respectively, but the increase rate gradually decreased. It shows that the change of shell side inlet temperature has limited effect on improving the heat transfer capacity of the heat exchanger.

(4) In the range of Reynolds number from 400 to 2,800, the Nusselt number on the shell side increases with the increase of Reynolds number, and the heat transfer factor and efficiency show a downward trend, which is conducive to improving the heat transfer performance of the heat exchanger. Compared with Reynolds number, shell side inlet temperature has little effect on shell side Nusselt number, heat transfer factor and efficiency of heat exchanger.

Conflict of interest

The authors declared no conflict of interest.

References

1. Wu Z, Xi H, Xu P. Numerical studies on geometric parametric analysis of helical-wound tube heat exchangers. Chemical Engineering 2019; 47(9): 12–17.
2. Fsadni AM, Whitty JPM. A review on the two-phase heat transfer characteristics in helically coiled tube heat exchangers. International Journal of Heat and Mass Transfer 2016; 95: 551–565.
3. Vocale P. Influence of thermal boundary conditions on local con-vective heat transfer in coiled tubes. International Journal of Thermal Sciences 2019; 145: 106039.
4. Ren Y. Numerical study on the shell-side flow and heat transfer of superheated vapor flow in spiral wound heat exchanger under rolling working conditions. International Journal of Heat and Mass Transfer 2018; 121: 691–702.
5. Lu X. Shell-side thermal-hydraulic performances of multilayer spi-ral-wound heat exchangers under different wall thermal boundary conditions. Applied Thermal Engineering 2014; 70(2): 1216–1227.
6. Zeng M, Zhang G, Li Y, *et al*. Geometrical parametric analysis of flow and heat transfer in the shell side of a spiral-wound heat exchanger. Heat Transfer Engineering 2015; 36: 790–805.
7. Sun C. Experimental study on shell-side pressure drop and offshore adaptability of LNG-FPSO spiral wound heat exchanger. Experimental Thermal and

Fluid Science 2019; 109: 109874.

8. Yu S. Experimental and numerical investigation of two-phase flow outside tube bundle of liquefied natural gas spiral wound heat exchangers under offshore conditions. Applied Thermal Engineering 2019; 152: 103–112.
9. Chen Z, Qin C, Dai W. Experimental research on heat transfer coefficient of spiral tube and numerical simulation of temperature field. Gas & Heat 2010; 30(1): 16–18.
10. Guo L, Chen X, Zhang M. Research on the forced convective boiling heat transfer characteristics of steam-water two-phase flow in horizontal helically coiled tubes. Journal of Xi'an Jiaotong University 1994; 28(5): 120–124.
11. Yu Q. Research on calculation method for helical wound coil tube heat exchangers [MSc thesis]. Dalian: Dalian University of Technology; 2011.
12. Naphon P. Study on the heat transfer and flow characteristics in a spiral-coil tube. International Communications in Heat and Mass Transfer 2011; 38: 69–74.
13. Zhang Z, Li Y, Wang Y, *et al*. Numerical simulation of fluid enhanced heat transfer in a helical tube under constant wall temperature condition. Refrigeration and Air-Conditioning 2016; 16(2): 43–48.
14. Sharqawy MH, Saad SMI, Ahmed KK. Effect of flow configura-tion on the performance of spiral-wound heat exchanger. Applied Thermal Engineering 2019; 161: 114–157.
15. Elattar HF. Thermal and hydraulic numerical study for a novel multi tubes in helically coiled tube heat exchangers: Effects of operating/geometric parameters. International Journal of Thermal Sciences 2018; 128: 70–83.

Thermal Science and Engineering (2021) Volume 4 Issue 2
doi:10.24294/tse.v4i2.1517

ORIGINAL RESEARCH ARTICLE

Research on optimization of collector module of new flat plate heat pipe PV/T heat pump system

Hongbing Chen, Baowu Li, Congcong Wang*, Huaning Yao, Xiaokun Zhang, Rui Zhao, Junhui Sun

Beijing Key Laboratory of Heating, Gas Supply, Ventilation and Air Conditioning Engineering, Beijing University of Civil Engineering and Architecture, Beijing 100044, China. E-mail: wangcongcong@bucea.edu.cn

ABSTRACT

The mathematical model of a new flat plate heat pipe PV/T heat pump system is established. The experimental data of the system under various working conditions are obtained through experimental measurement, and the accuracy and reliability of the model are verified. Based on the verified mathematical model, the thermal performance, electrical performance and the performance of the heat pump system are simulated. The results show that under winter conditions, the daily average thermal power, electrical power and COP of the system are 274.5 W, 93.5 W and 2.7 W respectively. Due to the low outdoor ambient temperature in winter, during winter operation, the heat collection system will lose a lot of heat to the surrounding environment through the photovoltaic panel surface, resulting in the heat collection of the system cannot meet the heat demand of the heat pump side, which is intuitively shown as the water temperature of the heat collection tank on the evaporation side shows a downward trend throughout the day. Therefore, the collector module of the system is optimized by adding a collector. After optimization, the daily average thermal power of the system is increased to 654.2 W and the COP is increased to 6.9.

Keywords: Flat Plate Heat Pipe; PV/T; Heat Pump; Numerical Simulation; Performance Optimization

ARTICLE INFO

Received: 4 August 2021
Accepted: 20 September 2021
Available online: 26 September 2021

1. Introduction

As a kind of renewable energy, solar energy has the characteristics of rich reserves, clean and pollution-free, and has gradually been paid attention to and widely used[1]. The solar photovoltaic photothermal comprehensive utilization system combines photovoltaic technology and photothermal technology, and uses the circulating fluid of the photovoltaic panel backplane to take away and collect the heat generated by the photovoltaic panel. While collecting heat, it can also reduce the temperature of the photovoltaic panel to improve the photoelectric conversion efficiency of the system[2]. Compared with the separate photovoltaic system and solar collector system, the solar photovoltaic solar thermal comprehensive utilization system can share system components, reduce system costs, and save building area[3]. Therefore, the comprehensive utilization system of solar photovoltaic light and heat has broad application prospects.

Many scholars at home and abroad have simulated PV/T (photovoltaic/thermal) system. As early as 1979, Hendrie[4] proposed the mathematical theoretical model of PV/T collector based on the traditional solar collector. In 1981, Raghuraman established a mathematical model to simulate and analyze the thermoelectric performance of water-cooled PV/T collector[5], and in 1985, he simulated and studied the air-cooled PV/T system[6].

Chow[7] established the dynamic mathematical model of water-cooled PV/T collector, simulated and analyzed the energy transfer process between different components in the system, and obtained the instantaneous characteristics of the system. As the water-cooled PV/T system is easy to freeze in winter when used in high latitude areas, some scholars proposed to apply heat pipe to PV/T system, and many scholars have carried out simulation research on circular heat pipe PV/T system. Ren *et al.*[8] established the mathematical model of the circular heat pipe PV/T system, and analyzed the influence of the heat pipe spacing, the presence or absence of the air layer and the thickness of the air layer on the performance of the whole system. The results showed that with the increase of the heat pipe spacing, the photoelectric and photothermal output of the system would decrease. In order to make better use of the low-grade heat energy collected by the heat pipe PV/T collector system, some scholars proposed to apply the heat pump to the heat pipe PV/T system. Zhang and Li[9] established the mathematical model of the photovoltaic solar heat pump/ring heat pipe composite system, and used the verified mathematical model to compare and simulate the performance of the system under the two working modes of heat pump operation alone and heat pump and ring heat pipe combined operation. The simulation results show that the working mode of heat pump and ring heat pipe combined operation should be adopted when the solar radiation intensity is high. In winter or when the solar radiation intensity is low, the working mode of independent operation of heat pump should be adopted.

In the traditional circular heat pipe PV/T heat pump system, the contact part between the circular heat pipe and the photovoltaic panel backplane is linear, resulting in less contact area, which affects the heat absorption efficiency of the heat pipe. Applying the new flat plate heat pipe to the heat pipe PV/T system can greatly increase the contact area between the heat pipe and the back plate of the photovoltaic panel and enhance the heat exchange efficiency of the heat pipe. However, there is little research about this part. In order to further study the impact of the new flat plate heat pipe on the operating performance of the heat pipe PV/T heat pump system, this paper has built an experimental device of the new flat plate heat pipe PV/T heat pump system, established the mathematical model of the system, verified the accuracy of the established mathematical model using the previously measured experimental data, and simulated the typical working conditions in winter according to the verified mathematical model. According to the simulation results, the heat collection part of the system is optimized.

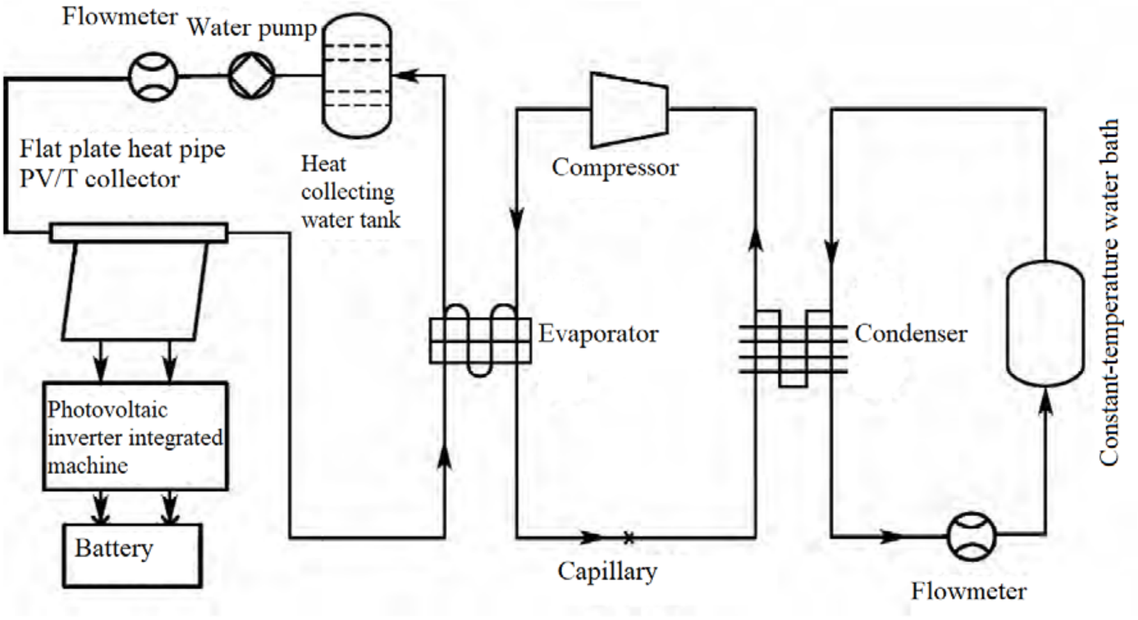

Figure 1. Schematic of the overall system.

2. Mathematical model of flat plate heat pipe PV/T heat pump system

2.1 System composition

Figure 1 is the schematic diagram of the new flat plate heat pipe PV/T heat pump system. The system is mainly composed of flat plate heat pipe PV/T heat collection system and heat pump system[10]. The main devices of the flat panel heat pipe PV/T heat collection system include: new flat panel heat pipe PV/T heat collector, heat collection water tank, expansion water tank, photovoltaic inverter control integrated machine, battery, electromagnetic flowmeter and water pump[11]. The heat pump device is mainly composed of evaporator, condenser, compressor and capillary tube[12]. The condenser and evaporator of the heat pump are plate heat exchangers, the evaporator is connected to the water tank on the evaporation side, and the constant temperature water bath is connected to the condensation side of the heat pump. The refrigerant filled in the heat pump system is R134a.

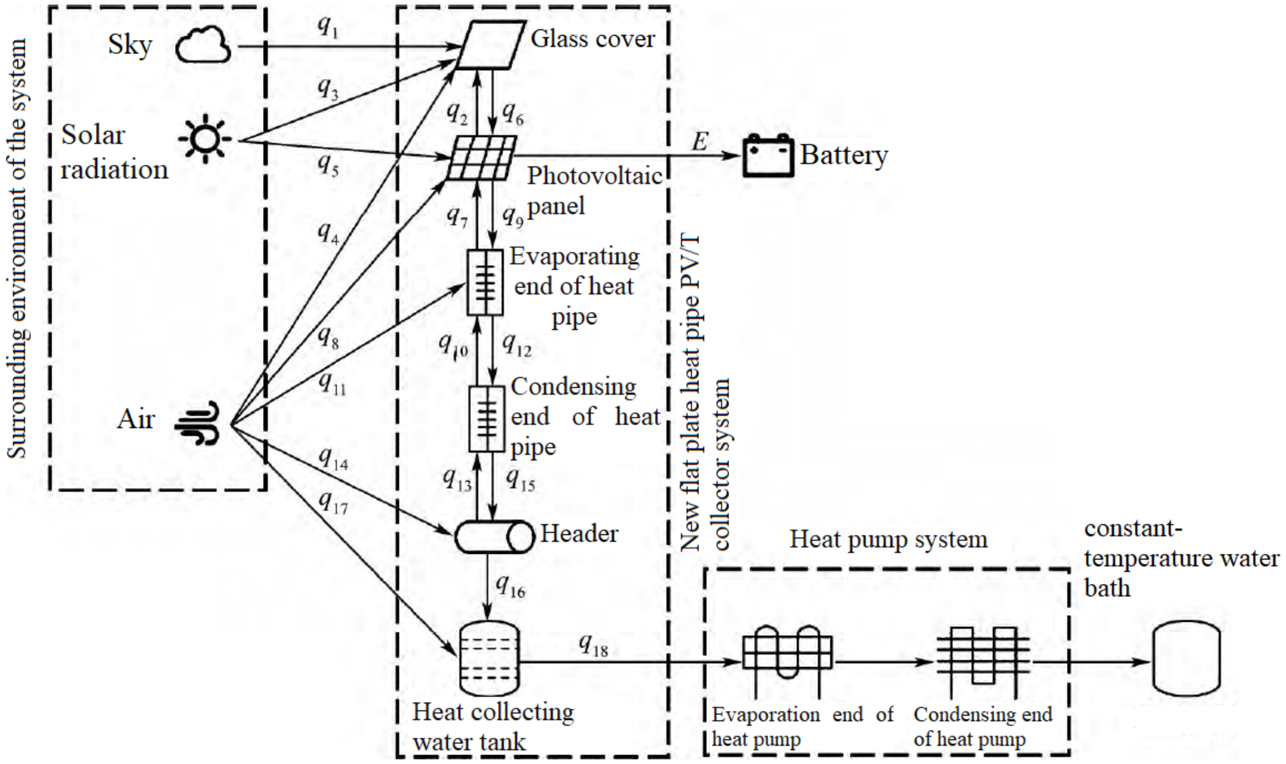

Figure 2. Energy transfer model diagram of a new flat heat pipe type PV/T heat pump system.

2.2 Establishment of system mathematical model

The energy transfer model of the new flat plate heat pipe PV/T heat pump system is shown in **Figure 2**. The sunlight shines on the photovoltaic panel through the glass cover plate, and the short-wave radiation is converted into electric energy, which is converted into AC through the photovoltaic reverse control device and stored in the battery. The long wave radiation is absorbed by the photovoltaic panel to generate heat, which is transmitted to the flat plate heat pipe on the photovoltaic panel back plate through the glass cover plate and the photovoltaic panel respectively. The liquid acetone in the evaporation end of the flat heat pipe is converted into vapor acetone after endothermic evaporation, and the acetone rises to the condensing end of the flat heat pipe after vaporization. After that, the circulating water in the header absorbs the heat at the condensing end of the flat heat pipe and the temperature rises. Under the power provided by the circulating water pump, the high-temperature water in the header is transmitted to the heat exchange coil in the heat collection tank, and the heat is released to the water in the heat collection tank through the heat exchange coil. As the low-temperature heat source of the heat pump, the heat of the heat collecting water tank is absorbed by the evaporation end of the heat pump, and then released to the constant temperature water bath pot by the condensation end of the heat pump.

Table 1. The physical meaning and formula of q_i

q_i	**Physical meaning**	**Formula**	**Physical meaning of parameters in formula**
q_1	Radiant heat transfer between glass cover and environment	$q_1 = h_{\mathrm{sky}}(t_{\mathrm{sky}} - t_{\mathrm{g}})$	h_{sky} is the radiant heat transfer coefficient between the glass cover plate and the environment, W/(m^2·°C); t_{sky} is the effective temperature, °C; t_{g} is the temperature of the glass cover plate, °C
q_2 q_6	Integrated heat transfer between glass cover and PV panel	$q_2 = h_{\mathrm{g,PV}}(t_{\mathrm{pv}} - t_{\mathrm{g}})$ $q_6 = h_{g,PV}(t_g - t_{\mathrm{pv}})$	$h_{\mathrm{g,pv}}$ are the comprehensive heat transfer coefficients between the glass cover plate and the photovoltaic panel; t_{pv} is the temperature of photovoltaic panel, °C
q_3	Solar radiation energy absorbed by glass cover plate	$q_3 = G\alpha_{\mathrm{g}}$	G is solar radiation intensity, W/m^2; α_{g} absorption rate of glass cover plate
q_4	Convection heat transfer between glass cover plate and surrounding environment	$q_4 = h_{\mathrm{a}}(t_{\mathrm{a}} - t_{\mathrm{g}})$	h_{a} is the convective heat transfer coefficient between the glass cover plate and the surrounding environment, W/(m^2·°C); t_{a} is the temperature of air, °C
q_5	Solar radiation energy absorbed by photovoltaic panels	$q_5 = G(\tau\alpha)_{\mathrm{pv}}$	$(\tau\alpha)_{\mathrm{pv}}$ is the effective absorption rate of photovoltaic panels
q_7	Heat exchange between photovoltaic panels and heat pipes	$q_7 = n\lambda\frac{1}{R_{\mathrm{ei}}}(t_{\mathrm{hpeva}} - t_{\mathrm{pv}})$	n is the total number of flat plate heat pipes on the back plate of photovoltaic panel; λ is the coverage rate of heat pipe; R_{ei} is the thermal resistance of heat conducting silica gel, (m^2·K)/W; t_{hpeva} is the temperature at the evaporation end of heat pipe, °C
q_8	Heat exchange between photovoltaic panels and the environment	$q_8 = (1 - n\lambda)h_{\mathrm{pv,a}}(t_a - t_{\mathrm{pv}})$	$h_{\mathrm{pv,a}}$ is the total heat transfer coefficient between the photovoltaic panel backplane and the surrounding environment, W/(m^2·K)
q_9	Heat absorbed by evaporation end of heat pipe	$q_9 = (t_{\mathrm{pv}} - t_{\mathrm{hpeva}})\frac{A_{\mathrm{hp,PV}}}{R_{\mathrm{ei}}}$	$A_{\mathrm{hp,\,pv}}$ is the contact area between each heat pipe and photovoltaic panel, m^2
q_{10} q_{12}	Evaporation end and cold end of heat pipe Heat exchange between condensing ends	$q_{10} = \frac{t_{\mathrm{hpcon}} - t_{\mathrm{hpeva}}}{R_{\mathrm{eva,con}}}$ $q_{12} = \frac{t_{\mathrm{hpeva}} - t_{\mathrm{hpcon}}}{R_{\mathrm{eva,con}}}$	t_{hPcon} is the temperature at the condensing end of the heat pipe, °C; $R_{\mathrm{eva,con}}$ is the thermal resistance between the evaporating end and condensing end of the heat pipe, (m^2·K)/W
q_{11}	Heat exchange between evaporation end of heat pipe and environment	$q_{11} = h_{\mathrm{hpeva}}A_{\mathrm{hp,pv}}(t_a - t_{\mathrm{hpeva}})$	h_{hpeva} is the heat transfer coefficient at the evaporation end of the heat pipe, W/(m^2·K)
q_{13} q_{15}	Condensation end and circulation of heat pipe Heat exchange of circulating water	$q_{13} = A_{\mathrm{w}}h_{\mathrm{w,con}}(t_{\mathrm{w}} - t_{\mathrm{hpcon}})$ $q_{15} = A_w h_{w,con}(t_{\mathrm{hpcon}} - t_w)$	A_{w} is the heat exchange area between condensing end and circulating water, m^2; $h_{\mathrm{w,con}}$ is the convective heat transfer coefficient between the condensing end and the circulating water, W/(m^2·K); t_{w} is the average temperature of circulating water in the header, °C
q_{14}	Heat exchange between circulating water and environment in header	$q_{14} = \frac{t_{\mathrm{a}} - t_{\mathrm{w}}}{R_{\mathrm{a,w}}}$	$R_{\mathrm{a,w}}$ is the thermal resistance between the circulating water in the header and the environment, (m^2·K)/W
q_{16}	Heat collection of header	$q_{16} = q_{m_{\mathrm{w}}}c_{\mathrm{w}}(t_{\mathrm{w,o}} - t_{\mathrm{w,i}})$	c_{w} is the specific heat capacity of water in the header, J/ (kg·°C); $q_{m_{\mathrm{w}}}$ is the mass flow of water in the header, kg/s; $t_{\mathrm{w,i}}$ and $t_{\mathrm{w,o}}$ are the inlet and outlet temperatures of water in the header respectively, °C
q_{17}	Heat exchange between collector tank and environment	$q_{17} = \frac{t_{\mathrm{a}} - t_{\mathrm{w,t}}}{R_{\mathrm{a,wt}}}$	$t_{\mathrm{w,t}}$ is the average temperature of water in the heat collection tank, °C; $R_{\mathrm{a,wt}}$ is the heat transfer resistance between the collector tank and the environment, (m^2·K)/W
q_{18}	Heat collection of heat pump	$q_{18} = q_{m_{\mathrm{r}}}(h_{\mathrm{r2}} - h_{\mathrm{r1}})$	$q_{m_{\mathrm{r}}}$ is the mass flow of refrigerant in the heat exchange element, kg/s; h_{r1} and h_{r2} are the specific enthalpy of inlet and outlet of refrigerant in the heat exchange element, J/kg

According to the energy transfer model diagram of the system, the mathematical model of the system can be established. The mathematical model of the new flat plate heat pipe PV/T heat pump system is divided into two parts, namely, the mathematical model of the new flat plate heat pipe PV/T heat collection system and the mathematical model of the heat pump system.

2.3 Verification of system mathematical model

Based on the experimental data measured before, this paper verifies the mathematical model of the new flat plate heat pipe PV/T heat pump system.

Figure 3 shows the meteorological data on the day of the test. As shown in **Figure 3**, the average solar radiation intensity of the day is 778.9 W/m^2, and the average outdoor air temperature is 31.4 ℃.

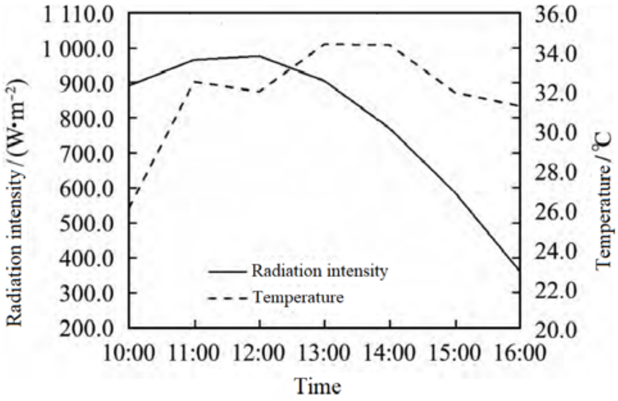

Figure 3. Variation of solar radiation and ambient temperature.

Figures 4, **5** and **6** show the comparison of measured and simulated values of the thermal performance, electrical performance and relevant parameters of the heat pump system. It can be seen from **Figure 4** that the simulated value of the system thermal power is lower than the measured value before 12:00, but higher than the measured value after 12:00, with a deviation of -1.3%–10.2%; the simulated value of the thermal efficiency of the system has been slightly higher than the measured value, and the deviation between the two is -1.0%–9.5%. It can be seen from **Figure 5** that the deviation between the simulated value and the measured value of the electric power of the system is -3.1%–2.4%; the deviation between the simulated value and the measured value of the electrical efficiency of the system is -2.1%–5.4%. It can be seen from **Figure 6** that the accuracy of the mathematical model of the heat pump system is high, and the deviation between the simulated and measured values of relevant parameters is very small. The deviation between the simulated and measured values of *COP* is only -0.4%–0.5%, and the deviation between the simulated and measured values of condensation heat exchange and compressor power is -2.4%–5.1% and 1.4%–3.3% respectively. The deviation between the simulated value and the measured value of the mathematical model of the system is within a reasonable range, and the model is more accurate.

3. System performance simulation and optimization

3.1 System performance simulation

Based on the verified mathematical model of the new flat plate heat pipe PV/T heat pump system, this paper simulates and analyzes the operation performance of the system. The meteorological data used in the simulation analysis is the previously collected measured data on December 13, 2019. In winter, generally, 40.0 ℃ domestic hot water can meet the daily needs of heat users[15], so the temperature of constant temperature water bath is set to 40.0 ℃ during simulation.

Figure 7 shows the meteorological data on the day of the test. It can be seen from **Figure 7** that the overall solar radiation intensity shows a trend of rising first and then declining, with an average of 492.5 W/m^2 and an average ambient temperature of 4.8 ℃.

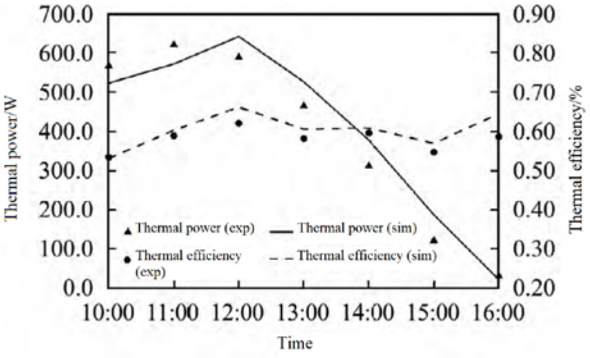

Figure 4. Comparison of measured and simulated values of thermal performance.

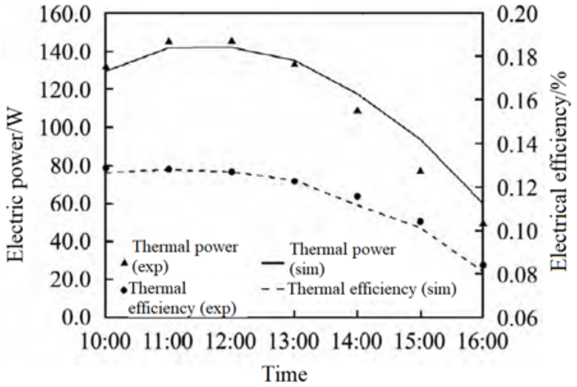

Figure 5. Comparison of measured and simulated values of electrical performance.

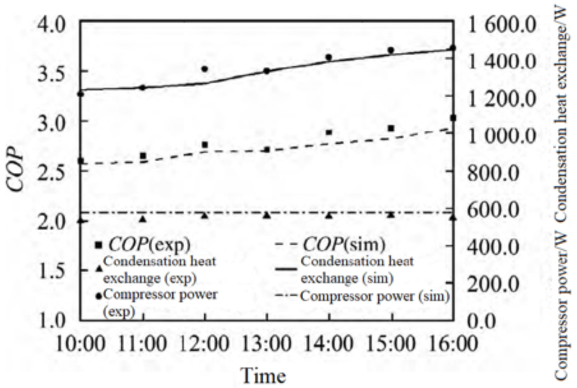

Figure 6. Comparison of measured and simulated values of the performance of heat pump system.

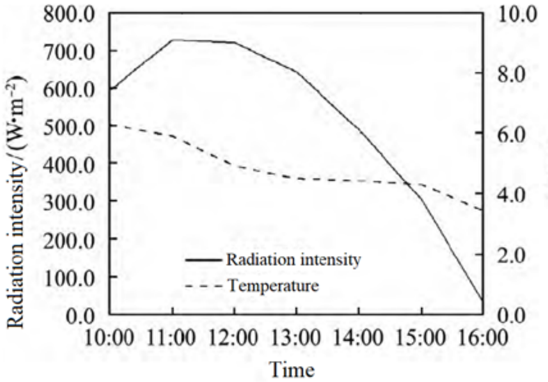

Figure 7. Variation of solar radiation and ambient temperature.

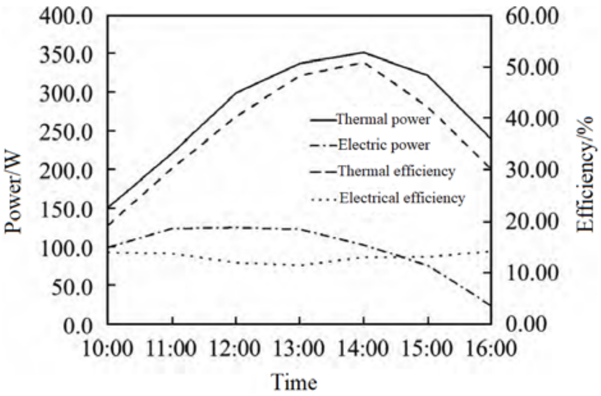

Figure 8. Variation of the thermoelectric performance.

Figure 8 shows the thermoelectric performance simulation results of the system. It can be seen from **Figure 8** that the change trend of thermal power and thermal efficiency is similar to that of solar irradiation intensity, both of which show a trend of rising first and then declining. The maximum value of thermal power appeared at 14:00, which was 351.4 W, and the daily average thermal power was 274.5 W; the maximum thermal efficiency is 48.10%, and the daily average thermal efficiency is 36.30%. It can also be seen from **Figure 8** that the overall change trend of electric power also increases first and then decreases, but the change range is small compared with thermal power and thermal efficiency. The maximum value of electric power is 123.3 W, and the daily average value is 93.5 W. Due to the high temperature of photovoltaic panels at noon, the electrical efficiency is at the lowest value, so the change of electrical efficiency shows a downward trend first and then an upward trend, but the overall change is relatively gentle, the maximum value of electrical efficiency is 14.10%, and the daily average value is 12.10%.

Figure 9 shows the simulation results of relevant parameters of the heat pump system. It can be seen from **Figure 9** that the overall change trend of *COP*, condensation heat exchange and compressor power is relatively flat. The daily average value of *COP* is 2.7, the daily average value of condensation heat exchange is 1,215.1 W, and the daily average value of compressor power is 577.9 W. It can be seen that the operation of heat pump in the whole day is relatively stable. The temperature of the heat collection tank at the evaporation side tends to decrease throughout the day. The initial temperature is set at 6.0 ℃, and the water temperature drops to the lowest value of 2.9 ℃ at the end of the simulation. It can be seen that the heat collected by the flat plate heat pipe PV/T heat collection system throughout the day does not meet the requirements of 40.0 ℃ constant temperature of water bath. This is because the capacity of the heat pump does not match the heat collection, resulting in insufficient heat collection of the flat plate heat pipe PV/T heat collection system. The heat pump needs to absorb heat from the hot water, so the water temperature will be lower and lower. Therefore, under winter conditions, the new flat plate heat pipe PV/T heat collection system using a collector cannot meet the requirements of 40.0 ℃ constant temperature of water bath, and the heat collection system needs to be optimized.

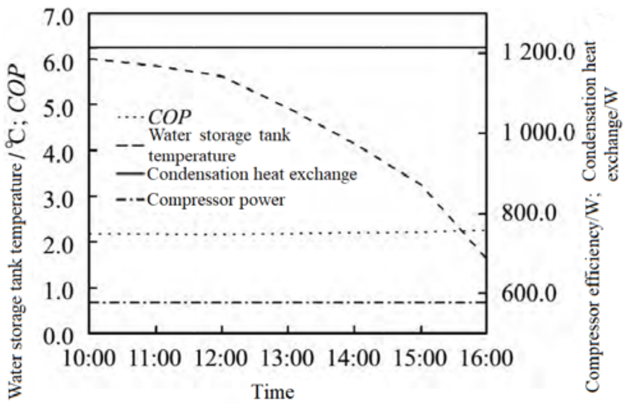

Figure 9. Variation of the performance of heat pump system.

3.2 System performance optimization

This paper aims to make the new flat plate heat pipe PV/T heat pump system designed to meet the domestic heat demand of heat users. In general, 40.0 ℃ domestic hot water can meet the daily needs of heat users in winter. Therefore, the heat collection of the optimized system should make the temperature of the constant temperature of water bath reach 40.0 ℃. Through the simulation and analysis of the system in winter, it can be seen that the system has not reached the expected requirements, so it is necessary to optimize the heat collection module of the system.

When designing a new flat plate heat pipe PV/T heat pump system, the factors such as heat pipe spacing, circulating water flow and photovoltaic cell coverage were simulated and optimized. This paper optimizes the performance of the system by changing the number of collectors. In the optimization, first increase the number of collectors to two, but through the simulation study, it is found that the results do not meet the expected goal, and then add another collector, using three collectors in series, the simulation shows that the results can meet the requirements.

Therefore, the optimization measure in this paper is to add two collectors in the heat collection system and adopt the mode of three collectors in series. The optimized simulation results are shown in **Figure 10**.

Figure 10 shows the change curve of the thermoelectric performance of the optimized system. It can be seen from **Figure 10** that the overall change trend of thermal power and thermal efficiency after optimization is similar, both rising first and then declining. The maximum value of thermal power is 882.2 W, and the daily average value is 654.2 W. The maximum value of thermal efficiency is 55.90%, and the daily average value is 35.90%. After optimization, compared with that before optimization, the thermal power is increased by 2.4 times, and the thermal efficiency remains basically unchanged. It can also be seen from the figure that the overall trend of the optimized electric power is to rise first and then decline. The maximum electric power is 340.5 W and the daily average is 252.2 W. The overall trend of electric efficiency after optimization is to decrease first and then increase. Contrary to the change trend of electric power, the lowest value of electric efficiency is 11.90%, and the daily average value is 13.00%. After optimization, the electric power is increased by 2.7 times, and the electric efficiency is basically unchanged.

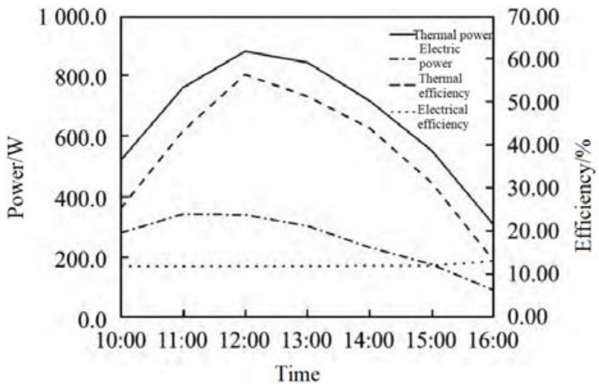

Figure 10. Variation of thermoelectric performance after optimization.

Figure 11 shows the change curve of relevant parameters of the heat pump system after optimization. It can be seen from **Figure 11** that the change trends of compressor power, *COP* and condensation heat exchange are relatively flat. The daily average value of compressor power is 581.1 W, *COP* is 6.9, and the daily average value of condensation heat exchange is 2,432.7 W. It can be seen that the performance of the heat pump has been greatly improved compared with that before optimization. The water temperature of the heat collection tank on the evaporation side generally shows a trend of rising first and then declining. At noon, the water temperature reaches the maximum value of 9.0 ℃. During the period from 10:00 to 15:30, the temperature of the heat collection tank is higher than the initial temperature. It shows that the heat collection of the new flat plate heat pipe PV/T heat collection system can meet the requirements of constant temperature of water bath at 40.0 ℃.

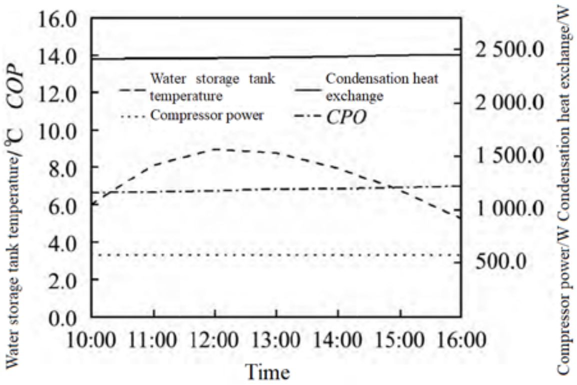

Figure 11. Variation of the performance of heat pump system after optimization.

4. Conclusion

In this paper, the mathematical model of a new flat plate heat pipe PV/T heat pump system is established, and the model is verified by experimental data. Based on the verified model, the system performance is simulated and optimized, and the conclusion is obtained.

(1) By comparing the experimental data with the simulation results, the error is -3.1%–10.2%. The mathematical model of the new flat plate heat pipe PV/T heat pump system has good reliability and accuracy.

(2) Under sunny conditions in winter, the daily average thermal power and thermal efficiency of the new flat plate heat pipe PV/T heat pump system are 274.5 W and 36.30% respectively, and the daily average electric power and electric efficiency are 93.5 W and 12.10% respectively. The average *COP* of the system is 2.7.

(3) After the optimization of the system, the daily average thermal power and electric power were increased to 654.2 W and 252.2 W respectively. At the same time, the performance of the heat pump system was also greatly improved, and its average *COP* reached 6.9.

Conflict of interest

The authors declared no conflict of interest.

References

1. Wang Y. Zhuzhai taiyangneng jizhong reshui gongying xitong qianxi (Chinese) [Brief analysis of residential solar concentrated hot water supply system]. Water & Wastewater Engineering 2008; 44(S2): 84–86.
2. Zhang Y. Experimental study of heat pipe solar photovoltaic/thermal systems utilization [MSc thesis]. Hohhot: Inner Mongolia University of Technology; 2018.
3. Yang P, Ma G. Taiyangneng redian lianyong xitong yanjiu (Chinese) [Research on solar power cogeneration system]. Automatic Application 2017; (11): 151–152.
4. Hendrie SD. Evaluation of combined photovoltaic/thermal collectors. Proceedings of ISES International Congress; 1979 May 28; Atlanta. Atlanta: ISES; 1979. p. 1865–1869.
5. Raghuraman P. Analytical predictions of liquid and air photovoltaic/thermal flat plate collector performance. Solar Energy Engineering 1981; 103: 291–298.
6. Cox CH, Raghuraman P. Design considerations for flat plate-photo voltaic/thermal collectors. Solar Energy 1985; 35: 227–245.
7. Chow TT. Performance analysis of photovoltaic-thermal collector by explicit dynamic model. Solar Energy 2003; 75: 143–152.
8. Ren Y, Yang H, Lv J, *et al*. Simulation study of heat pipe spacing and air layer on PV/T system performance. Acta Energiae Solaris Sinica 2018; 39(4): 965–971.
9. Zhang Z, Li S. Performance simulation of photovoltaic solar assisted heat pump/loop heat pipe hybrid water heater system. Journal of Central South University (Science and Technology) 2017; 48(12): 3392–3399.
10. Chen H, Niu H, Zhang L, *et al*. Experimental study on heat-pipe PV/T heat pump system under different working modes. Renewable Energy Resources 2017; 35(12): 1791–1797.
11. Chen H, Zhang L, Wang Q, *et al*. Experimental study on the performance of heat pipe PV/T hot water system. Journal of Beijing University of Civil Engineering and Architecture 2016; 32(1): 59–64.
12. Yu C. Zhileng jishu jiangzuo (wu)—Disijiang zhengqi yasuoshi zhilengji de gongzuo yuanli (Chinese) [Lectures on refrigeration technology (5)—Fourth lecture on the working principle of vapor compression refrigerator]. Refrigeration Tech-

nology 1983; (4): 52–58.

13. Chen H, Yao H, Gong Y, *et al*. Performance study of a novel flat plate heat pipe solar PV/T collector system. Renewable Energy 2019; 37(8): 1139–1145.
14. Zhang L. Performance study of heat pipe solar PV/T heat pump system [MSc thesis]. Beijing: Beijing University of Civil Engineering and Architecture; 2017.
15. Chen X, Hao B, Peng C, *et al*. Testing and investigative research of solar domestic hot water system. Building Science 2015; 31(10): 154–161.

Thermal Science and Engineering (2021) Volume 4 Issue 2
doi:10.24294/tse.v4i2.1518

ORIGINAL RESEARCH ARTICLE

Study on heat transfer characteristics of regenerative shell-and-tube heat exchangers

Xiaoze Du*, Huiqian Guo, Yu Wang, Lijun Yang

School of Energy, Power and Mechanical Engineering, North China Electric Power University, Beijing 102206, China. E-mail: duxz@ncepu.edu.cn

ABSTRACT

A new type of regenerative shell-and-tube heat exchanger is designed to solve the problems that the generation load of cogeneration units is limited by the amount of heat supply during the heating period, the peak shaving capacity of units decreases, and the phenomenon of wind and light abandonment in the power system is serious. Considering the advantages of nearly constant temperature and large potential heat release during the heat storage/release process of phase change materials, paraffin is selected as the phase change material, and the phase change area of the heat exchanger is selected as the heat exchange unit. The control variates method is used to simulate the heat storage/release process of the heat exchange unit according to the key factors such as the flow rate of heat transfer fluid, the thermal conductivity of phase change materials and the thickness of phase change layer. The results show that increasing the flow rate of heat transfer fluid can enhance the heat storage capacity of the heat exchange unit and shorten the complete melting time of phase change materials. In order to control the heat at the output end of the heat exchanger during the heat release process, the flow rate of heat transfer fluid should be appropriately selected; using composite materials to improve the thermal conductivity of phase change materials can enhance the heat transfer capacity of the heat exchange unit, and the average heat transfer coefficient of the heat exchange unit is more than 2 times higher than that of pure paraffin at the same heat transfer fluid flow rate; increasing the thickness of phase change layer can prolong the time of maintaining the outlet temperature of heat transfer fluid in the process of heat release.

Keywords: Cogeneration; Phase Change Material; Numerical Simulation; Regenerative Heat Exchanger

ARTICLE INFO

Received: 7 August 2021
Accepted: 24 September 2021
Available online: 8 October 2021

1. Introduction

The cogeneration unit adopts the operation mode of “determining electricity by heat” during the heating period, resulting in poor flexibility of peak load regulation, which will aggravate the phenomenon of wind and light abandonment in the power system. Using heat storage technology in the heating system to realize “thermoelectric decoupling” is an effective technical way to improve the load peak shaving capacity of cogeneration units during the heating period[1-5]. Local heat exchange stations generally use plate heat exchangers and shell-and-tube heat exchangers, without the ability to adjust the heat load. The regenerative heat exchanger takes the phase change material as the core, and makes use of its advantages such as large latent heat absorbed and released during the phase change process and nearly constant phase change temperature, so that the heat exchanger encapsulated with phase change material has the functions of heat storage and maintaining the stability of cold source outlet temperature, so as to improve the unit heat storage density and heat supply stability of the heat exchanger.

Domestic and foreign scholars’ research on regenerative heat exchanger mainly focuses on two parts: using CFD software to simulate the heat transfer characteristics of regenerative heat exchangers and design effective ways to enhance heat transfer; the heat transfer process in the simulation is verified by experiments, and the practical application of regenerative heat exchangers in cogeneration unit is studied. Wang *et al.*[6] established two kinds of shell-and-tube heat storage units, namely light tube and finned tube, analyzed the changes in heat transfer characteristics of phase change material after adding aluminum finned tubes, and found that using finned heat exchange tubes can shorten the complete melting and heat release time to 68.0% and 85.5% of that of light tube heat exchange units, respectively. Zhang and Zheng[7] studied the heat transfer behavior on the paraffin side of phase change material through experiments and found that when the heat source temperature is 65 ℃, the total heat storage time of finned tubes is 22.5% of that of smooth tubes. Murray and Groulx[8] used dodecanoic acid as phase change material to establish a shell-and-tube phase change heat storage unit, and studied the effect of the speed of heat transfer fluid on the heat storage and release performance. It was found that the melting time decreased with the increase of flow rate during the heat storage process, and the flow rate did not affect the solidification time during the heat release process. Liu and Groulx[9] conducted experimental research on a cylinder latent heat storage system and found that heat conduction was the main heat transfer mechanism at the initial stage of heat storage, and natural convection was dominant when enough phase change material melted. Wang *et al.*[10] designed a vertical shell-and-tube heat storage device using erythritol as phase change material. The experiment shows that increasing the inlet temperature and mass flow of the heat transfer fluid during the heat storage and release process can significantly enhance the internal heat transfer of the phase change material and shorten the heat storage and release time. Yang *et al.*[11,12] proposed to fill the phase change material into foam metal copper and conduct numerical simulation of the heat storage system encapsulated with composite materials in view of the low thermal conductivity of phase change materials. The research shows that adding fins and foam metal can significantly accelerate the melting process and alleviate the phenomenon of overheating at the top and non-melting at the bottom caused by natural convection. Xu *et al.*[13] added an energy storage device to the cogeneration unit and established a new thermoelectric integrated system, which realized thermoelectric decoupling and improved the flexibility of peak load regulation of the cogeneration unit. Haeseldonckx *et al.*[14] proposed a scheme for the combined use of multiple small-scale cogeneration devices and heat storage tanks. Through simulation, it was found that the installation of heat storage tanks can prolong the service life of cogeneration devices, and the use of small-scale heat storage devices can reduce CO_2 emissions to 1/3 of ordinary cogeneration units. Zhang *et al.*[15] proposed to install heat storage devices in the combined electric heating system and wind power heating system at the same time, and formulate a reasonable start-up and stop control strategy considering the comprehensive coordination of the power grid, the lagging characteristics of the thermal parameters of the heat storage system and the daily regulation plan.

The literature review found that regenerative heat exchangers used in the thermoelectric decoupling of cogeneration process can be further optimized in terms of structural design and operation mode. Based on the existing work, this article proposes a new type of regenerative shell-and-tube heat exchanger suitable for the heating network of thermal power stations, and carries out performance simulation research for the structure and process design.

2. Design and physical model of the regenerative heat exchanger

As shown in **Figure 1**, the regenerative heat exchanger is divided into the phase change zone and heat exchange zone by the shunt. During heat storage, the hot fluid flows into the heat flow tube, and the heat is transferred to the phase change material through the wall and fins as the heat source in the phase change area. After the phase change material melts, the hot fluid flows into the heat exchange zone to exchange heat with the cold fluid. During heat release, due to the reduction of hot fluid flow, the heat exchange of cold fluid in the heat exchange zone is insufficient, and the outlet temperature is lower than the solidification temperature of phase change material. Phase change material exchanges heat with cold fluid through pipe wall and fins in the phase change zone. Considering the heating temperature of the heating station, latent heat of phase change material, thermal conductivity, chemical stability, whether it is non-toxic, corrosive, cheap and easy to obtain and easy to package, paraffin is selected as the phase change material of the heat storage heat exchanger.

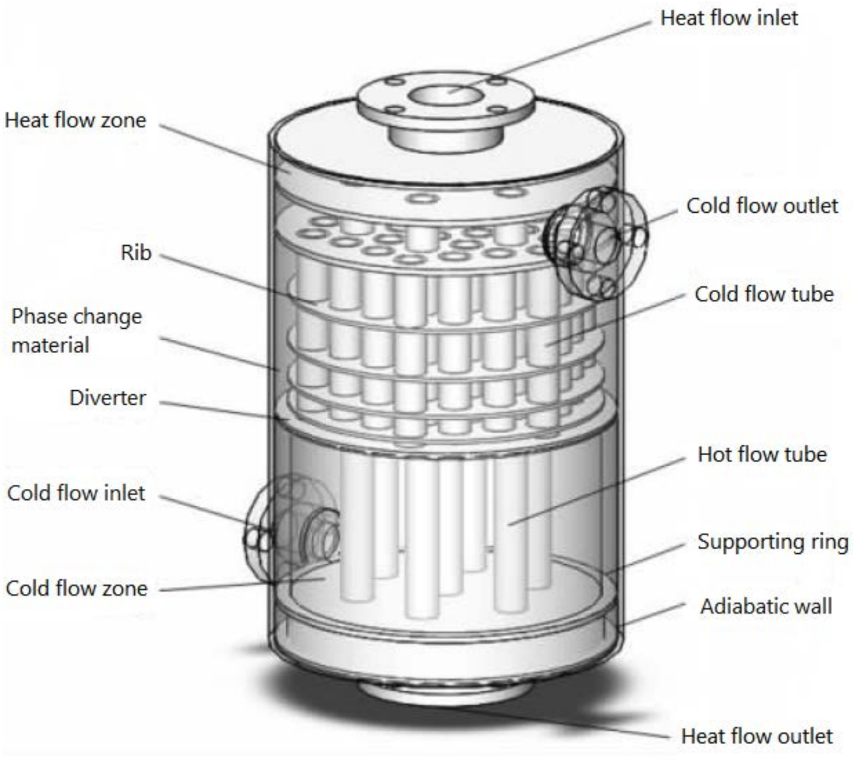

Figure 1. Schematic diagram of the regenerative heat exchanger.

Take the partial structure of the phase change zone of the regenerative heat exchanger to establish the regenerative heat exchange unit, as shown in **Figure 2(a)**. The outer annular ribs of the circular tube wall are arranged parallel to the upper end face and the bottom face with unequal spacing[16], and the closer to the inlet end of the heat fluid, the greater the spacing of the adjacent fins. In the traditional equidistant rib heat accumulator, due to that the heat transfer temperature difference along the flow direction of high-temperature heat transfer fluid is becoming smaller and smaller in the heat storage process, the phase change material in the inlet section is easy to overheat, the phase change material in the outlet section cannot be completely melted, and the overall utilization rate of phase change material is low. The resulting uneven distribution of temperature and thermal stress reduces the service life of phase change material and container material. The arrangement of ribs with unequal spacing is adopted to make the overall heat exchange temperature difference of the heat exchange unit close, and the heat exchange effect is uniform, so as to alleviate the overheating of the phase change material at the inlet of the hot fluid, reduce the local overheating of the phase change material and the excessive thermal stress of the heat storage container, and improve the overall utilization rate of the phase change material. According to the adiabatic characteristics of the symmetrical boundary, the intercepted regenerative heat exchange unit is a regular hexagonal prism. Considering the periodicity of the equipment, the interaction between the unit structure and the heat storage unit in the direction of gravity, the 1/6 structure of the intercepted heat exchange unit is taken as the simulation calculation domain. As shown in **Figure 2(b)**, in the central 1/6 cylinder is the heat transfer fluid, and the phase change material is stored between the two adjacent ribs. In the process of heat storage/release, because the thermal resistance of the circular tube wall is much smaller than that of the phase change material, the thickness of the circular tube wall is ignored to simplify the structure of the heat exchange unit and the complexity of the simulation operation.

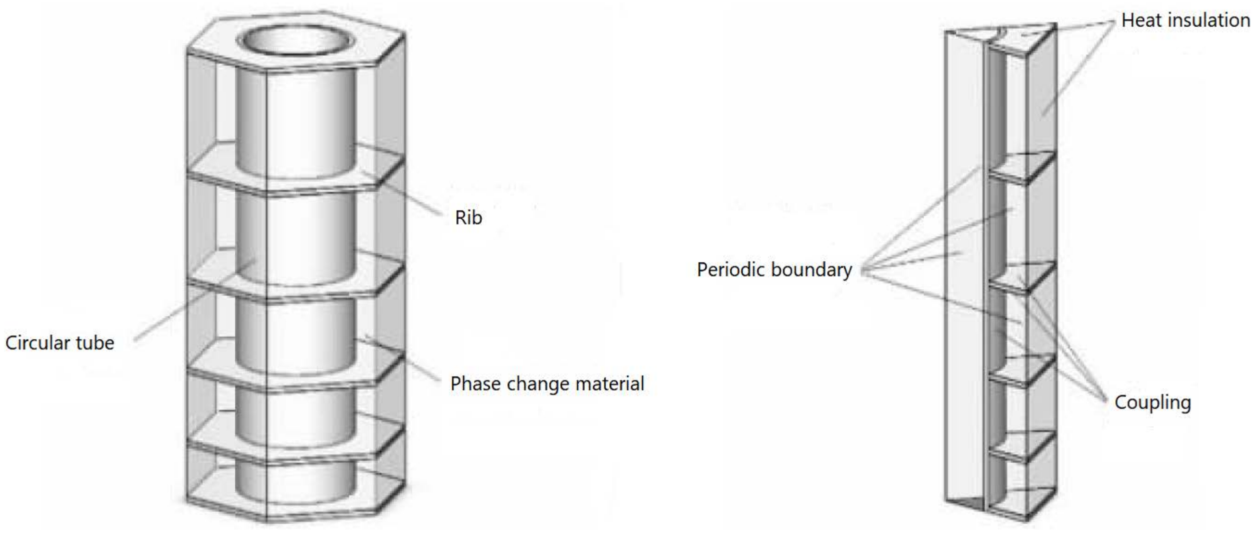

(a) (b)

Figure 2. Schematic diagram of the regenerative heat transfer unit.

Table 1. Material physical properties of the heat transfer unit[17]

	Density/(kg·m^{-3})	**Specific heat capacity/(J·kg^{-1}·K^{-1})**	**Thermal conductivity/(W·m^{-1}·K^{-1})**	**Latent heat of phase change/(kJ·kg^{-1})**	**Dynamic viscosity/(kg·m^{-1}·s^{-1})**
Phase change material	760	2,100.00	0.25	170	0.00324
Water	1,000	4,182.00	0.60	-	0.00100
Rib	2,179	871.00	202.40	-	-
Side plate	8,030	502.48	16.27	-	-

The regenerative heat exchanger designed in this article is mainly used in the secondary heat supply network heater. When the heat is sufficient, the phase change material absorbs the heat of the primary heat supply network water for heat storage; when peak shaving is required, the phase change material releases heat to maintain the water outlet temperature of the secondary heat supply network. The phase change material selected in the simulation is paraffin, the heat transfer fluid is tap water, the installed annular rib is aluminum rib, and the side plate is steel. The physical parameters are shown in **Table 1**.

3. Mathematical model

3.1. Numerical methods and control equations

The phase change regenerative heat exchange unit is established, and the unsteady phase change heat transfer is simulated by FLUENT software. The solidification and melting processes of the heat storage medium are simulated mainly by using the solidation/melting model, VOF method and "enthalpy porosity" model. The porosity is used to represent the volume share of liquid phase material in the calculation domain, and the porosity is 1 when it is completely melted. The enthalpy method model is used to calculate, and the continuity equation, momentum equation and energy equation are solved to track the phase interface. In order to simplify the calculation, assumptions are made for the model: (1) the paraffin filled into the heat exchange unit is evenly distributed and isotropic; (2) the density of paraffin phase change material is constant and does not change with temperature. Both solid and liquid paraffin are considered as constant physical properties; (3) paraffin, cold and hot fluids have no axial heat conduction; (4) ignoring the natural convection of paraffin in the process of heat storage/release; (5) paraffin does not have supercooling and overheating during solid-liquid phase transition; (6) neglecting viscous dissipation effect; (7) there is no internal heat source and internal heat sink.

According to the assumption, the control equations of the regenerative heat exchange unit are as follows.

Continuity equation:

$$\nabla(\rho v) = 0 \tag{1}$$

Momentum equation:

$$\frac{\partial(\rho v)}{\partial t} + \nabla(\rho v v) = -\nabla p + \nabla(\mu v) \tag{2}$$

Energy equation:

$$\rho \frac{\partial h_i}{\partial t} = \lambda \nabla^2 T \tag{3}$$

Where

$$h_i = h + \Delta h_i \tag{4}$$

$$h = h_{\mathrm{ref}} + \int_{T_{\mathrm{ref}}}^{T} c_p \, \mathrm{d}T \tag{5}$$

$$\Delta h_i = \varphi L \tag{6}$$

In equtations (1)–(6): ρ is the density, kg/m^3; V is the material flow rate, m/s; T is the temperature, K; t is the occurrence time of phase transition, s; p is pressure, N/m^2; μ is the dynamic viscosity, kg/(m·s); λ is the thermal conductivity, W/(m·K); h_i is the specific enthalpy of the material at any time, J/kg; h_{ref} is the initial specific enthalpy, J/kg; T_{ref} is the initial temperature, K; c_p is the specific constant pressure heat capacity, J/(kg·K); L is the latent heat of phase transition, J/kg; φ is the volume fraction of liquid phase, specifically defined as

$$\varphi = \begin{cases} 0 & T < T_{\mathrm{s}} \\ \dfrac{T - T_{\mathrm{s}}}{T_{\mathrm{l}} - T_{\mathrm{s}}} & T_{\mathrm{s}} < T < T_{\mathrm{l}} \\ 1 & T > T_{\mathrm{l}} \end{cases} \tag{7}$$

Where: T_{s} is the melting point of the material, K; T_{l} is the freezing point of the material, K.

3.2 Boundary conditions and initial conditions

In the simulation of heat storage shell-and-tube heat exchange unit, during heat storage, the inlet boundary condition of water is velocity inlet boundary condition; the velocity is 0.300 m/s, the turbulence intensity is 4.67%, the hydraulic diameter is 0.02 m, and the inlet temperature is 363.15 K; during heat release, the flow rate of water is 0.030 m/s, and the inlet temperature is 293.15 K.

The initial conditions are as follows: setting the temperature of paraffin and ribs at 324.15 K during heat storage; setting the temperature of paraffin and ribs at 330.15K during heat release.

3.3 Model validation

In this article, the heat storage experiment of the tube-rib phase change regenerator in [7] is selected for simulation verification. The temperature of the heat transfer fluid is 338.15 K, and the initial temperature of paraffin and ribs is 298.15K. The temperatures of the experimental measurement points R2 and R3 are selected as the simulation monitoring values, and the influence of natural convection is ignored in the simulation. **Figure 3** shows the curve of the simulated value and the experimental measured value of the temperature of tube-rib phase change accumulator points R2 and R3 calculated by the numerical model with time, as shown in **Figure 3**, the relative error between the simulated calculation results and the experimental results is less than 5%, and the change trend of the simulated value and the experimental measured value is basically consistent, which verifies the accuracy of the numerical model selected in this article. The grid sensitivity test is carried out for the exothermic process of the regenerative heat exchange unit. **Figure 4** shows the time-varying curve of the liquid volume fraction of phase change material in the exothermic process. From **Figure 4**, we can see 7.0611 × 10^5 is the optimal grid number.

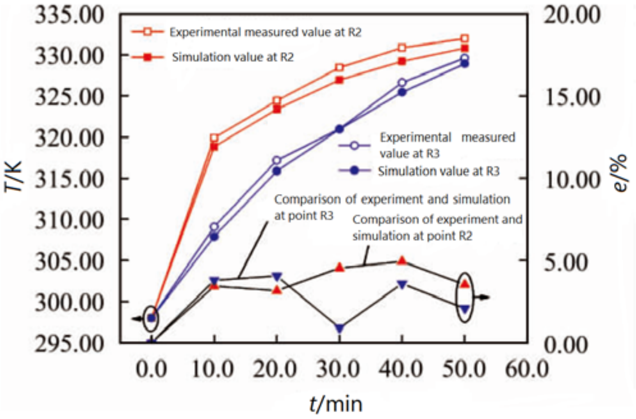

Figure 3. Comparison of the experimental results and numerical simulation results.

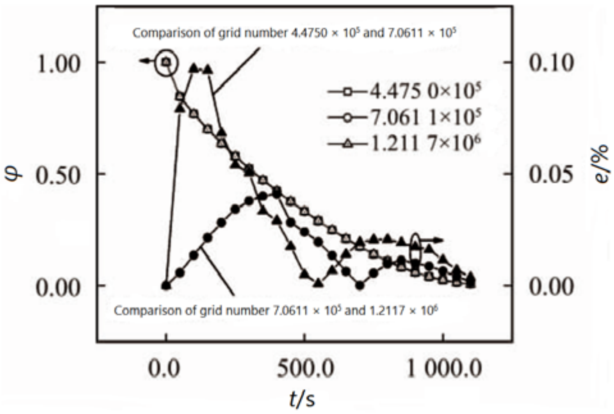

Figure 4. Results of the grids sensitivity test.

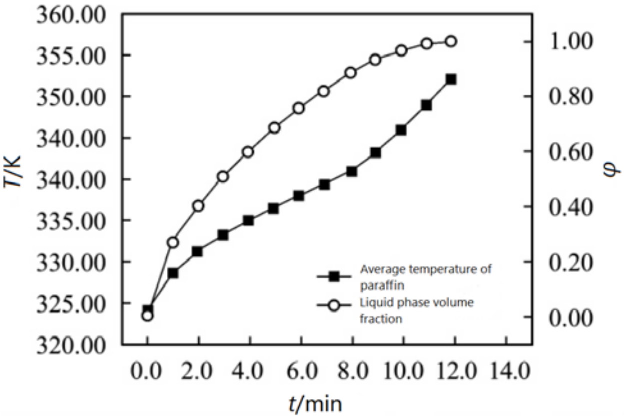

Figure 7. Variations of average temperature of paraffin and liquid phase volume fraction with time.

4. Results and discussion

Using FLUENT software and single variable method, the heat transfer characteristics of heat exchange unit under different working conditions are simulated by changing the flow rate of heat transfer fluid, the thermal conductivity of phase change materials and the structural size of equipment.

4.1 Simulation of heat storage/release process of heat exchange unit

In the process of heat storage, as shown in **Figures 5** and **6**, the inlet temperature of the heat transfer fluid is 363.15 K and the speed is 0.300 m/s. It flows in the circular tube from top to bottom and releases heat to the phase change area. The phase change layer is heated and melted, the solid-liquid phase change interface moves to the backheat area, and the temperature and volume integral number of the liquid paraffin continue to rise. With the continuous enlargement of the liquid phase area of paraffin and the continuous increase of temperature, the heat transfer temperature difference between paraffin and hot fluid decreases, the heat transfer intensity decreases, and the volume fraction of liquid paraffin and the temperature rise rate decrease, as shown in **Figure 7**. Until the paraffin is completely melted, the total heat storage capacity of the heat storage and heat exchange unit is 255.01 kJ.

During the exothermic process, the inlet temperature of the cold fluid is 293.15 K, and the flow rate is 0.030 m/s. As shown in **Figures 8** and **9**, the paraffin solidification releases the latent heat of phase change, and the temperature gradually decreases. Due to the enhanced heat transfer effect of the fins, the solidification process of the liquid paraffin near the fins progresses rapidly. As can be seen from **Figure 10**, with the passage of time, the cold fluid continuously absorbs heat, the average outlet temperature increases, and the maximum temperature reaches 307.14 K; then the solidification process advances, and the solid-liquid phase transition interface moves away from the cold fluid until the paraffin is completely solidified, and the average outlet temperature of the cold fluid drops to the initial temperature.

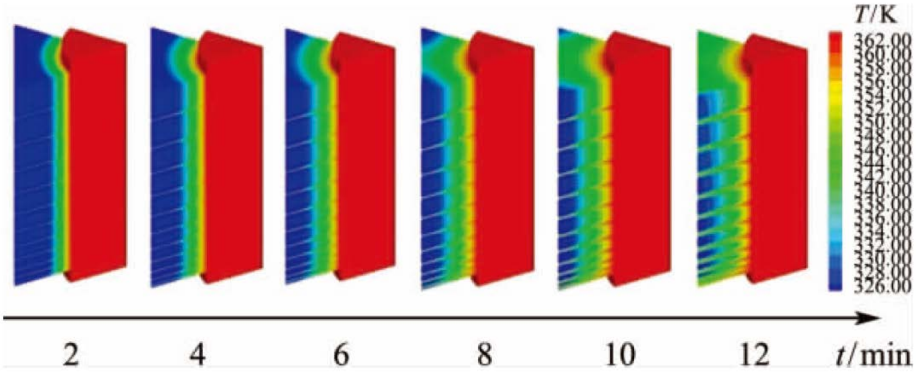

Figure 5. Temperature nephogram of heat transfer unit.

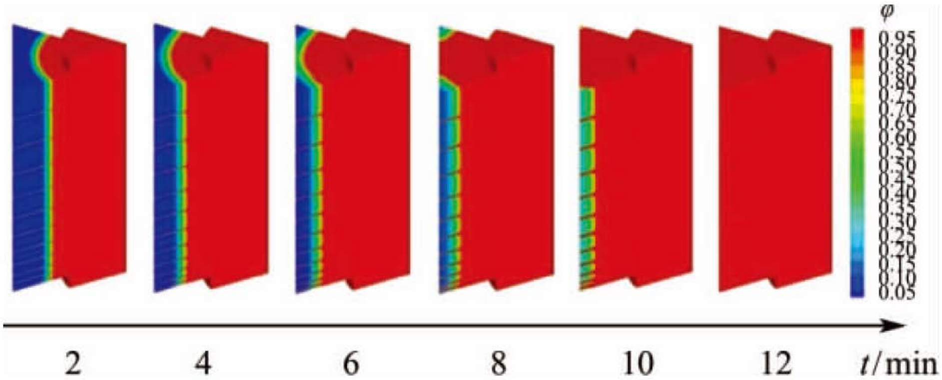

Figure 6. Liquid phase volume fraction nephogram of paraffin.

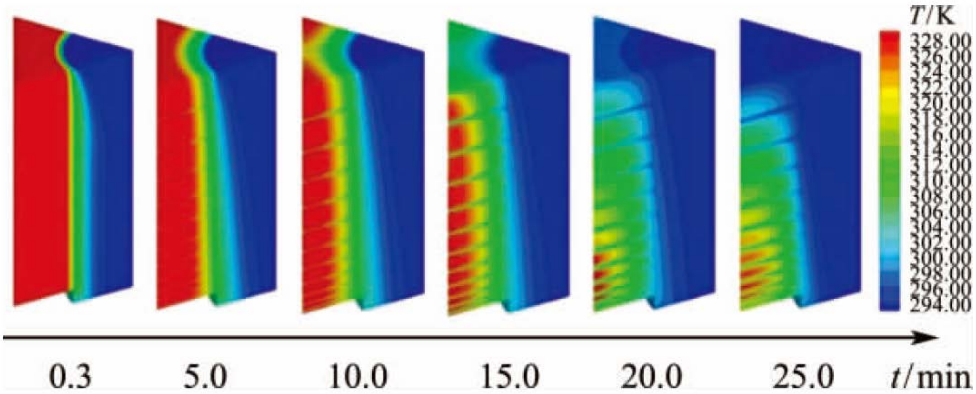

Figure 8. Temperature cloud diagram of heat exchange unit.

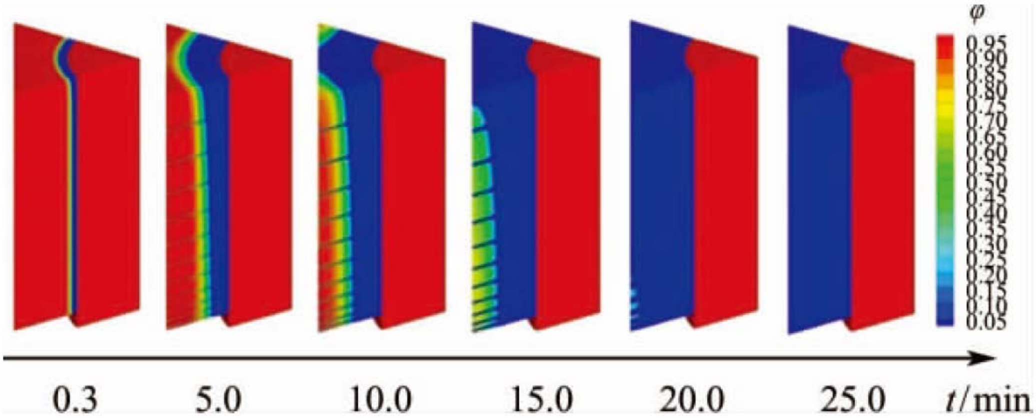

Figure 9. Liquid phase volume fraction nephogram of paraffin.

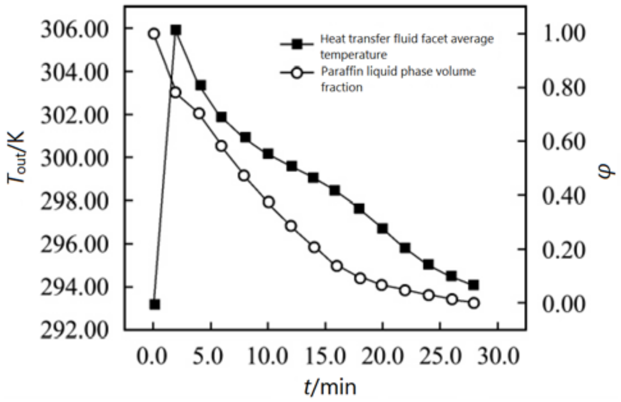

Figure 10. Variations of heat transfer fluid facet average temperature and paraffin liquid phase volume fraction with time.

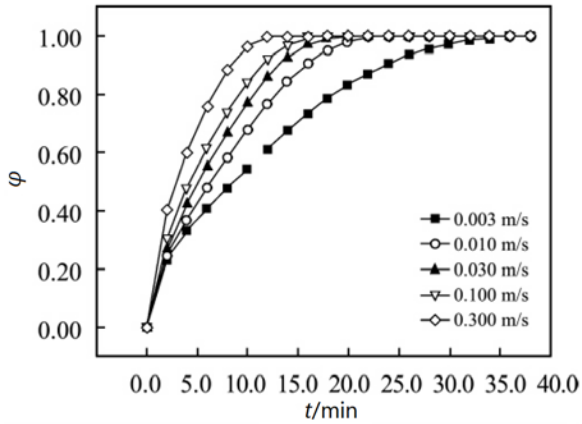

Figure 11. Variations of paraffin liquid volume fraction with different heat transfer fluid velocity.

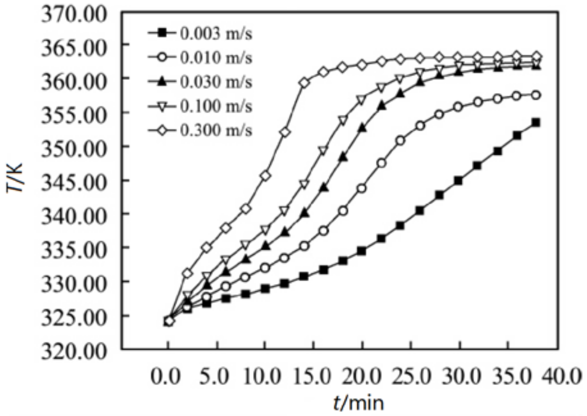

Figure 12. Variations of paraffin average volume temperature with different heat transfer fluid velocity.

4.2 Effect of heat transfer fluid flow rate on heat transfer capacity of heat exchange unit

Figure 11 shows that the flow rate of heat transfer fluid has a great influence on the heat storage process. The faster the flow rate of heat transfer fluid, the shorter the time required for the complete melting of paraffin. The time required for the complete melting of paraffin at the flow rate of 0.300 and 0.030 m/s is 0.32 and 0.53 times that at the flow rate of 0.003 m/s, respectively.

It can be seen from **Figure 12** that at the initial stage of heat storage, the exothermic temperature of hot fluid decreases, the heat absorption temperature of paraffin melting rises, the heat transfer temperature difference between the two gradually decreases, and the temperature rise rate of paraffin gradually decreases; with the expansion of the liquid region, the effect of the increase of the temperature in the liquid region on the increase of the average temperature rise rate in the phase change region is more than that of the decrease of the heat transfer temperature difference on the inhibition of the average temperature rise rate in the phase change region, and the temperature rise rate of paraffin gradually increases; finally, when the temperature difference between paraffin and heat transfer fluid is small enough, the temperature rise rate of paraffin decreases further.

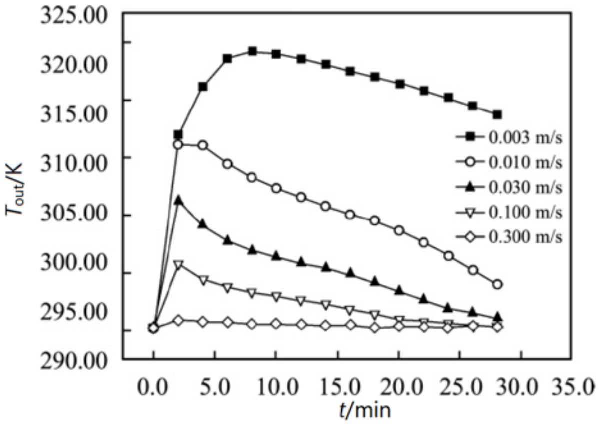

Figure 13. Variations of heat transfer fluid facet average temperature with different velocity.

During the heat release process, the average outlet temperature of the heat transfer fluid is greatly affected by the fluid flow rate, and the outlet temperature increases with the decrease of the fluid flow rate, as shown in **Figure 13**. When the flow rate is 0.003 m/s, the maximum temperature rise of the heat transfer fluid is 5.79 times that of 0.300 m/s. Because the lower the flow rate of heat transfer fluid, the longer the heat absorption time in the heat exchange unit, and the problem of reducing the mass flow of fluid and the total heat provided by the output end of the heat exchanger, it is necessary to reasonably select the flow rate of heat transfer fluid according to the actual situation to ensure the optimization of system performance.

Figure 14 shows that the paraffin solidification process is greatly affected by the flow rate of heat transfer fluid. It can increase the average outlet temperature by reducing the fluid speed, but the heat carried by the cold fluid decreases at the same time. As the reduction of heat transfer temperature difference and convective heat transfer coefficient weakens the heat transfer capacity of the heat exchange unit, the paraffin solidification process slows down and the released latent heat decreases.

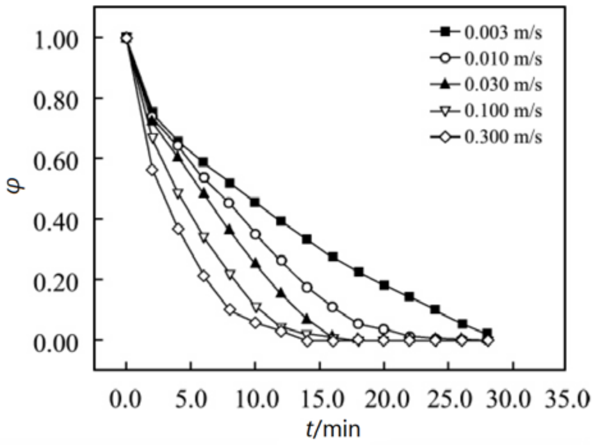

Figure 14. Variations of paraffin liquid volume fraction with different heat transfer fluid velocity.

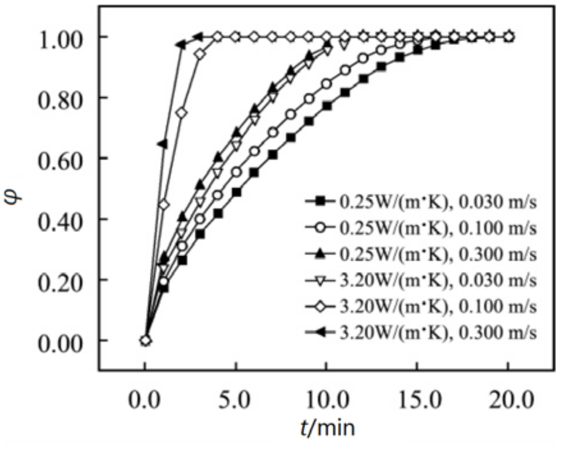

Figure 15. Variations of paraffin liquid volume fraction.

4.3 Effect of thermal conductivity of phase change material on heat transfer capacity of heat exchange unit

It can be seen from section 4.2 that the heat transfer fluid can get a good temperature rise only under the condition of low flow rate in the process of heat release, which is unrealistic in actual working conditions. The composite material of expanded graphite and paraffin in document[18] is selected as the heat storage medium, and the thermal conductivity is increased from 0.25 of pure paraffin to 3.20 W/(m·K).

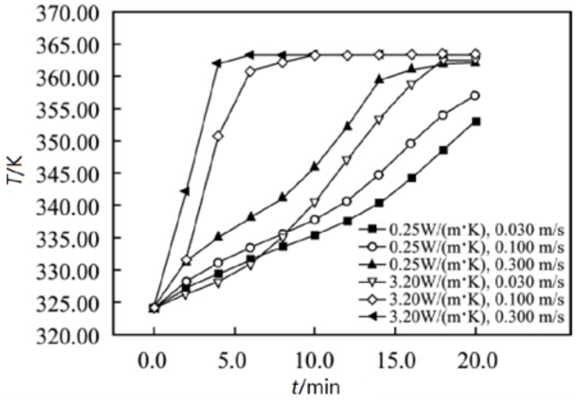

Figure 16. Variations of paraffin average volume temperature.

In the process of heat storage, three different flow rates are selected at the inlet of the heat transfer fluid: 0.030, 0.100 and 0.300 m/s. It can be seen from **Figures 15** and **16** that the completion time of the heat storage process of the heat exchange unit installed with composite materials at the same flow rate is much shorter than that of the pure paraffin heat exchange unit. In the three working conditions with flow rates of 0.030, 0.100 and 0.300 m/s, the time for the complete melting of the composite is 0.46, 0.40 and 0.33 times that of pure paraffin, respectively.

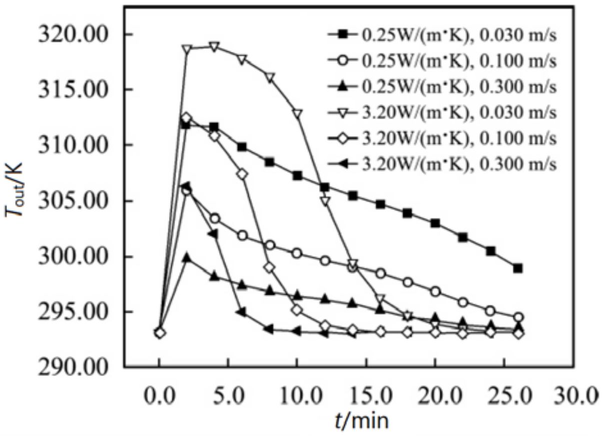

Figure 17. Variations of heat transfer fluid facet average temperature.

It can be seen from **Figure 17** that in the early stage of the heat release process, under the same flow rate and time, the average temperature of the heat transfer fluid outlet under the condition of high thermal conductivity is higher than that under the condition of low thermal conductivity。 In the three working conditions of flow rate of 0.030, 0.100 and 0.30 m/s, the maximum outlet temperature of the heat exchange unit installed with composite material is 6.50, 6.70 and 6.40 K higher than that installed with pure paraffin. With the advance of the exothermic process, the phase change material with high thermal conductivity solidifies rapidly, the solid layer thickens, the heat transfer resistance increases, the heat transfer temperature difference decreases, and the heat flow decreases due to the depletion of phase change latent heat. At the same flow rate and time, the average outlet temperature of the heat transfer fluid is gradually lower than that of pure paraffin.

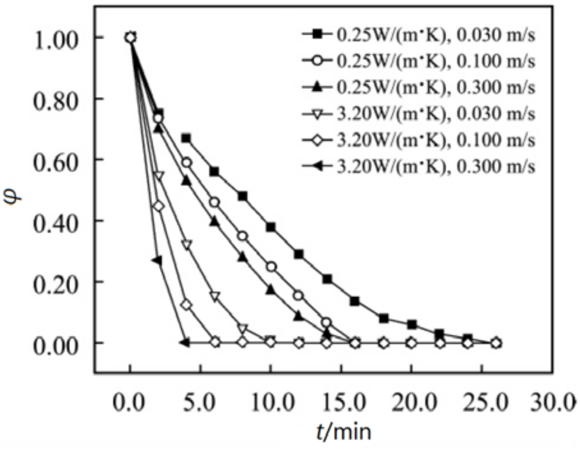

Figure 18. Variations of paraffin liquid volume fraction.

Figure 18 shows the change trend of paraffin liquid volume fraction during the exothermic process. It can be seen from **Figure 18** that phase change material with high thermal conductivity solidifies faster at the same flow rate and time. Use equations (8)–(10) to calculate the average heat transfer coefficient of the regenerative heat exchange unit.

$$\dot{Q} = c_{\mathrm{p}}\Delta\bar{T} + m_{\mathrm{p}}\Delta L \tag{8}$$

$$q = Q/\Delta t \tag{9}$$

$$q = \bar{k}\Delta T_m A \tag{10}$$

Where: $\dot{Q}$ is the heat release of the heat exchange unit in the calculation period, kJ/kg; c is the specific heat capacity of paraffin, kJ/(kg·K); m_{p} is the mass of paraffin, kg; $\bar{T}$ is the average heat exchange temperature difference of paraffin, K; ΔL is the latent heat released during paraffin solidification, kJ/kg; Δt is the time interval, s; k is the average heat transfer coefficient of the heat exchange unit, W/(m^2·K); ΔT_m is the average heat exchange temperature difference, K; A is the area of heat exchange surface, $\bar{k}$.

In the calculation, the time of completing the solidification process is rounded, and the maximum error is 2.0 min. After calculation, the average heat transfer coefficient of the heat exchange unit with composite material is more than twice that of the heat exchange unit with pure paraffin at the same flow rate.

4.4 Effect of phase change layer thickness on heat transfer capacity of the heat exchange unit

Improving the thermal conductivity of phase change material plays a great role in strengthening the heat transfer capacity of the heat exchange unit, but in the process of heat release, the solidification of phase change material is too fast, resulting in the decrease of heat output at the outlet of heat transfer fluid.

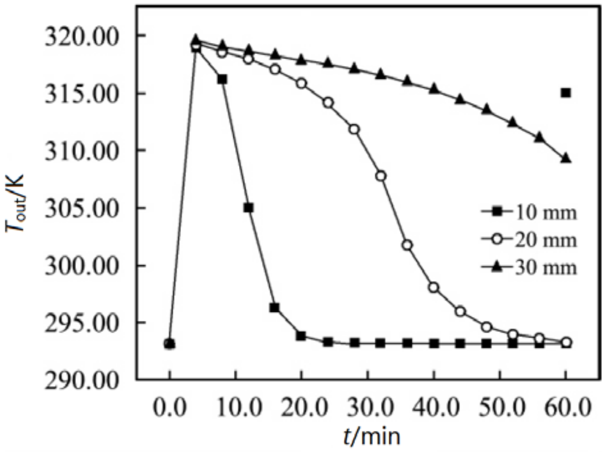

Figure 19. Variations of heat transfer fluid facet average temperature.

As shown in **Figure 19**, considering the heat supply quality at the outlet of the heat exchange unit, the heat transfer fluid flow rate of 0.030 m/s and the thermal conductivity of phase change material of 3.20 W/(m·K) are selected to simulate the heat release process. The results show that the thickness of the phase change layer has little effect on the heating stage of heat transfer fluid; in the cooling stage, the greater the thickness of the phase change layer, the more latent heat of phase change that can be provided to the heat transfer fluid, and the slower the temperature decay of the heat transfer fluid. For heat exchange units with phase change layers of 10, 20 and 30 mm, the average temperature of the heat transfer fluid outlet is maintained above 315.00 K for 9.5, 20.3 and 38.7 minutes respectively, effectively ensuring the heating quality of the output end of the regenerative heat exchanger.

5. Conclusion

In this article, a regenerative shell-and-tube heat exchanger is designed. In order to alleviate the uneven heat exchange temperature difference of the traditional equidistant rib structure heat exchanger and the high thermal stress of the heat storage container, the unequal spacing rib arrangement structure is adopted, the phase change area of the heat exchanger is selected as the heat exchange unit, and the control variates method is used to discuss the heat transfer characteristics of the heat exchange unit and draw a conclusion.

(1) The velocity of heat transfer fluid has a great influence on the heat storage process. The faster the velocity of heat transfer fluid is, the shorter the time for paraffin to melt completely.

(2) Improving the thermal conductivity of phase change materials plays a great role in strengthening the heat transfer capacity of the heat exchange unit. Under the three working conditions of flow velocity of 0.030, 0.100 and 0.300 m/s, the time of complete melting of the composite is 0.46, 0.40 and 0.33 times that of pure paraffin respectively; at the same flow rate in the exothermic process, the average heat transfer coefficient of the heat exchange unit with composite material is more than 2 times higher than that with pure paraffin.

(3) Increasing the thickness of the phase change layer can prolong the maintenance time of the average outlet temperature of the heat transfer fluid, and effectively ensure the heating quality in the process of heat release.

Conflict of interest

The authors declared no conflict of interest.

References

1. Chen L, Xu F, Wang X, *et al.* Implementation and effect of thermal storage in improving wind power accommodation. Proceedings of the CSEE 2015; 35(17): 4283–4290.
2. Yang L, Liu Y, Fang W, *et al.* Operation optimization of cogeneration unit equipped with heat accumulator. Thermal Power Generation 2020; 49(4): 70–76.
3. Yang Y, Liang Y, Zhou J, *et al.* Research of heat transfer efficiency in phase change thermal storage. Journal of Thermal Science and Technology 2011; 10(3): 226–230.
4. Cui H, Zhou H, Jiang J. Numerical simulation on heat storing performances of phase-change thermal storage for solar energy. Renewable Energy Resources 2013; 31(12): 17–20.
5. Ma Z, He Y, Yuan F, *et al.* Experimental study on the thermal performance of high-temperature shell-and-tube molten salt phase-change thermal energy storage. Journal of Xi'an Jiaotong University 2017; 51(5): 1–8.
6. Wang M, Tian S, Han Q, *et al.* Numerical simulation and optimization of heat storage unit of shell and tube heat exchanger. Energy Conservation 2016; 35(8): 11–15.
7. Zhang Y, Zheng D. Heat transfer performance of paraffin as a phase change material (PCM) in a concentric annulus. Journal of Beijing University of Chemical Technology (Natural Science Edition) 2006; 34(2): 5–8.
8. Murray RE, Groulx D. Experimental study of the phase change and energy characteristics inside a cylindrical latent heat energy storage system, Part 1: Consecutive charging and discharging. Renewable Energy 2014; 62(63): 571–581.
9. Liu C, Groulx D. Experimental study of the phase change heat transfer inside a horizontal cylindrical latent heat energy storage system. International Journal of Thermal Sciences 2014; 82(1): 100–110.
10. Wang Y, Wang L, Xie L, *et al.* Experimental study on the melting and solidification behavior of erythritol in a vertical shell-and-tube latent heat thermal storage system. International Journal of Heat & Mass Transfer 2016; 99(1): 770–780.
11. Yang J, Du X, Yang L, *et al.* Tianchong paomo jinshu de rongyan xiangbian xure guocheng moni (Chinese) [Numerical analysis of molten salt phase-change process in metal foams]. Journal of Engineering Thermophysics 2014; 35(11): 2256–2260.
12. Yang J, Du X, Yang L, *et al.* Visualized experiment on dynamic thermal behavior of phase change material in metal foam. CIESC Journal 2015; 66(2):

497–503.
13. Xu F, Min Y, Chen L, *et al.* Combined electricity-heat operation system containing large capacity thermal energy storage. Proceedings of the CSEE 2014; 34(29): 5063–5072.
14. Haeseldonckx D, Peeters L, Helsen L, *et al.* The impact of thermal storage on the operational behavior of residential CHP facilities and the overall CO_2 emissions. Renewable & Sustainable Energy Reviews 2007; 11(6): 1227–1243.
15. Zhang LP, Chen L, Wang X, *et al.* Study on thermal storage device model and control strategy for cogeneration and wind power heating system. Applied Mechanics and Materials 2015; 740: 460–465.
16. Xu H, Du X, Yang J, *et al.* (inventors). Zhu K (assignee). A cylindrical structure gradient fin phase change regenerator. Chinese patent. 201510303521.9. 2015 Aug 26.
17. Ke B. Numerical simulation and heat transfer enhancement of paraffin phase change heat transfer process at outer tube [Master's thesie]. Zhenjiang: Jiangsu University; 2016.
18. Sun W, Han L, Wu Z. Numerical calculation of effective thermal conductivity coefficients of expanded graphite/paraffin phase change composites. Acta Materiae Compositae Sinica 2015; 32(6): 1596–1601.

Thermal Science and Engineering (2021) Volume 4 Issue 2
doi:10.24294/tse.v4i2.1519

ORIGINAL RESEARCH ARTICLE

Analysis of influence of ripple parameters of heat storage elements on flow and heat transfer performance

Yuzhen Yu, Haikuan Di*, Bo Zhao, Haiying Li

School of Mechanical Engineering North China University of Technology, Tangshan 063210, China. E-mail: dihaikuan_1996@163.com

ABSTRACT

In order to study the influence of the corrugated angle and width of enamel heat storage element on the flow and heat transfer performance, a certain enamel heat storage element was numerically simulated by FLUENT software, and the variation curves of internal flow field velocity, temperature distribution, Nusselt number and drag coefficient with Reynolds number were obtained when the corrugated angle and width of the heat storage element were different. The simulation results show that when the ripple inclination increases from 20° to 60°, the resistance coefficient of the heat storage element increases, and the Nusselt number increases, and the increase of the resistance coefficient is greater than that of the Nusselt number; when the ripple width increases from 6 mm to 10 mm, the increase of resistance coefficient is small, and the increase of Nusselt number is large.

Keywords: Rotary Air Preheater; Heat Storage Element; Resistance Coefficient; Nusselt Number

ARTICLE INFO

Received: 1 September 2021
Accepted: 8 October 2021
Available online: 19 October 2021

COPYRIGHT

1. Introduction

Rotary air preheater is a kind of heat exchange device, which is widely used in thermal power plants. Its core component is the heat storage elements arranged in the rotor. The flow and heat transfer characteristics of the heat storage elements determine whether the rotary air preheater can operate safely and efficiently[1,2]. Therefore, studying the heat transfer and resistance characteristics of heat storage elements and the distribution of internal temperature field under different structural parameters is of great significance to improve the flow and heat transfer performance of rotary air preheater and ensure the safe and efficient operation of boiler. Scholars at home and abroad have studied the flow and heat transfer performance of heat storage elements. Wang[3] found that controlling the frictional resistance along the way is the key to reducing the flow resistance of heat storage elements through a large-scale hot air tunnel experimental system. Chi[4] proposed a scheme to measure the temperature of the low-temperature heating surface of the rotary air preheater. Mohammed[5] found that the effect of convective heat transfer can be enhanced by adding ripple to the heat storage element. Focke[6] found that when the corrugation angle is large, the increase of the corrugation angle is small, and the increase of the convection heat transfer coefficient is small. Yang[7] conducted enamel transformation on the heat storage element and found that the comprehensive convective heat transfer performance was significantly improved.

This paper studies the heat storage elements with different corrugated structure parameters by numerical simulation, analyzes the temperature and velocity distribution of the internal flow field, and obtains the influence of the corrugated inclination and width on the flow and heat transfer performance of the heat storage elements.

2. Numerical simulation

2.1 Rotary air preheater

Rotary air preheater is mainly composed of rotor, heat transfer element, shell, beam, sector plate and sealing device[8]. The boiler flue gas flows in through the flue gas channel from top to bottom, and the air flows out of the primary air and secondary air outlets from bottom to top. Each revolution of the rotor, the heat storage element absorbs and releases heat once[9,10]. There are two 30° transition zones in the rotor, in which neither flue gas nor air passes through, which plays the role of separating flue gas and air. The structure is shown in **Figure 1**.

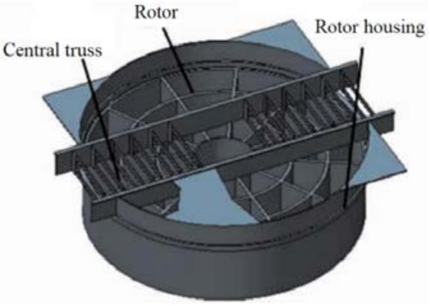

Figure 1. Structure of rotary air preheater.

2.2 Simulation objects and model assumptions

2.2.1 Simulation object

The simulation object is an enamel heat storage element, the structure is shown in **Figure 2**, and the structural parameters are shown in **Table 1**.

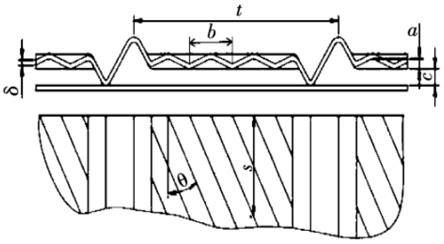

Figure 2. Structure of enamel heat storage element.

Table 1. Structural parameters of heat storage elements

Plate thickness δ/mm	Equivalent diameter *d*/mm	Span *t*/mm	Ripple gap *c*/mm	Surface density/m^{-1}	Corrugated plate corrugated wave height *a*/mm	Ripple width of corrugated plate *b*/mm
1.15	12.54	65.9	5.3	398.8	3.03	8

Table 2. Structural parameters for different inclination of corrugation

Corrugation inclination *θ*/(°)	Equivalent diameter *D*/mm	Ripple axial pitch *s*/mm
20	12.48	8.62
30	12.54	9.35
40	12.60	10.51
50	12.64	12.6
60	12.75	16.2
70	12.27	23.68

Table 3. Structural parameters for different ripple width

Ripple width *b*/mm	Equivalent diameter *D*/mm	Ripple axial pitch *s*/mm
6	12.27	12.1
7	12.53	14.3
8	12.75	16.2
9	12.9	18.1
10	13	20.4

Under the condition that the ripple width and height of the heat storage element remain unchanged, change the ripple inclination angle to 20°, 30°, 40°, 50°, 60° and 70° in turn, and the changed structural parameters are shown in **Table 2**.

When the corrugation angle of the heat storage element is 60° and the height remains unchanged, the corrugation width is changed to 6, 7, 8, 9 and 10 mm in turn. The changed structural parameters are shown in **Table 3**.

When changing the ripple parameters, the equivalent diameter of the heat storage channel will change, and the calculation formula[11] is:

$$D = \frac{4A}{L} \tag{1}$$

Where: A—sectional area of flow channel between corrugated plate and flat plate of heat storage element, mm^2; L—wet perimeter of flow channel between corrugated plate and flat plate of heat storage element, mm.

2.2.2 Model assumptions and simplification

For the convenience of numerical simulation, the following assumptions and simplifications are made:

Because the internal structure of the heat storage element is complex, and the waveform changes periodically. Therefore, a flow unit of heat storage element is taken as the research object[12]; the wall thickness of heat storage element is 0[13]; air is regarded as compressible Newtonian fluid; the heat storage element is simplified into a constant wall temperature model; the length of the heat storage element is 500 mm (the inlet effect can be ignored)[14].

2.3 Physical model and boundary conditions

2.3.1 Physical model and grid division

The required model is established in CREO software, tetrahedral mesh division is adopted for all plate heat storage elements, and an expansion layer is set near the wall to solve the high gradient flow change and complex physical characteristics near the wall. When the inclination is 20°, the number of grid units is 1.1962 million, when the inclination is 50°, the number of grid units is 1.097 million, and when the inclination is 70°, the number of grid units is 1.054 million, which has passed the verification of grid independence. The grid division is shown in **Figure 3**.

Figure 3. Grid division.

2.3.2 Boundary conditions and model settings

Fluent software is used for three-dimensional numerical simulation, using mass conservation equation, momentum conservation equation, and slip free boundary conditions. The inlet temperature is 293 K, the wall temperature is 373 K, and air is used as the flowing medium (density ρ 1.225 kg/m^3, dynamic viscosity μ is 1.75 × 10^{-5} Pa·s, thermal conductivity λ is 0.0242 W/(m·K)), and other parameter settings are shown in **Table 4**.

Table 4. Parameter settings

Parameter	**Settings**
Viscous model	k-ε Model
Near wall treatment	Enhanced wall treatment
Pressure velocity coupling	Simple format
Discretization of momentum equation and energy equation	Quick format
Wall thermal boundary condition	Constant temperature
Inlet boundary conditions	Speed inlet
Exit boundary conditions	Free outflow

2.3.3 Evaluation method

The flow and heat transfer performance of the regenerative element of the rotary air preheater mainly depends on the resistance coefficient and convection heat transfer coefficient between the medium and the regenerative plate[15]. The greater the resistance coefficient is, the worse the flow performance of the heat storage element will be. The convective heat transfer coefficient of the heat storage element refers to the heat transfer capacity between the air and the surface of the heat storage element. The higher the value, the better the heat transfer performance of the heat storage element. Further, the variation law of Nusselt number Nu with Reynolds number Re can be used to indicate the intensity of convective heat transfer of the heat storage element[16,17]. The resistance coefficient[18] is:

$$f = \frac{2d\Delta p}{l\rho v^2} \tag{2}$$

Where: Δp—frictional resistance of air flowing through the heat storage element, Pa; ρ—air density, kg/m^3; v—actual flow speed of air flowing through the element, m/s; d—equivalent diameter of heat storage element, m; l—length of heat storage element, m.

The Nusselt number formula[19] is:

$$Nu = \frac{a d_{\mathrm{dl}}}{\lambda} \tag{3}$$

Where: a—Convective heat transfer coefficient, W/(m^2·K); d_{dl}—equivalent diameter of heat storage element, m; λ—Thermal conductivity of fluid medium, W/(m·K).

Reynolds number is calculated as:

$$Re = \frac{\rho v d}{\mu} \tag{4}$$

Where: v—actual flow speed of air flowing through the flow channel of the element, m/s; μ—Dynamic viscosity of air, Pa·s.

3. Results and analysis

3.1 Influence of corrugation angle

3.1.1 Velocity nephogram

When the inlet wind speed is 10 m/s, the outlet velocity nephogram of the heat storage element with the wavy inclination of 20°, 30°, 40°, 50°, 60° and 70° is shown in **Figure 4**.

It can be seen from **Figure 4** that the maximum speed at the outlet of the heat storage channel is the maximum when the ripple angle is 20°, and the value is 31.118 m/s. The maximum speed at the outlet of the heat storage channel with the ripple angle of 70° is the minimum, and the value is 17.539 m/s. According to the report function in **Figure 4** in fluent software, the average speed at the outlet of 20°–70° heat storage channel is 10.48, 10.09, 10.05, 9.91, 9.87 and 9.99 m/s respectively.

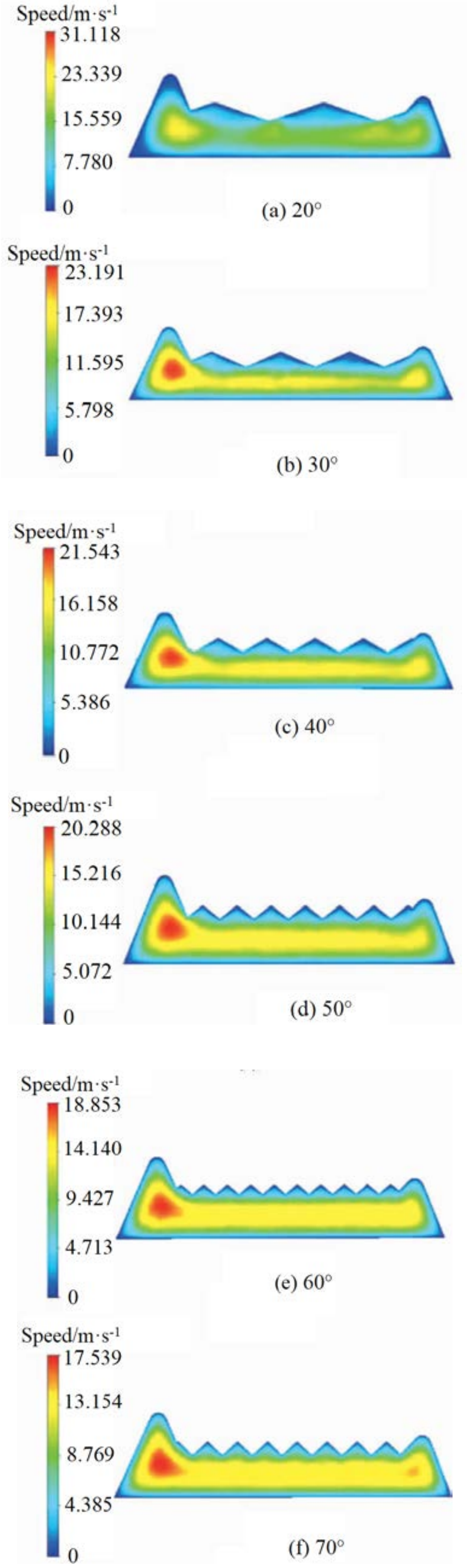

Figure 4. Contour of outlet velocity of thermal storage element.

When the ripple angle increases from 20° to 60°, the average speed at the outlet of heat storage channel decreases in turn. With the increase of corrugation angle, the number of oblique corrugations decreases, the resistance of heat storage channel to air decreases, and the speed gradually decreases. The corrugated channel of the 70° corrugated heat storage element is narrow and close to vertical, and part of the air flows directly from the channel, so the speed increases.

3.1.2 Temperature nephogram

When the inlet wind speed is 10 m/s, the temperature nephogram at the inlet of the heat storage channel with different corrugated inclination is shown in **Figure 5**.

Using the report function in **Figure 5** in fluent software, the average temperature at the 16 mm section at the inlet of the heat storage element with a ripple inclination of 20°–70° is 318.84, 319.90, 320.75, 321.68, 323.58 and 320.10 K respectively. The heat exchange performance of the heat storage element is the best when the ripple angle is 60°, and the worst when the ripple angle is 20°. When the wavy angle is 20°, the disturbance in the direction of temperature gradient is very small, and there is not enough convective heat transfer between the air and the wall. When the corrugated angle is 60°, the contact area between the air and the heat storage element is the largest, which is conducive to enhancing convective heat transfer.

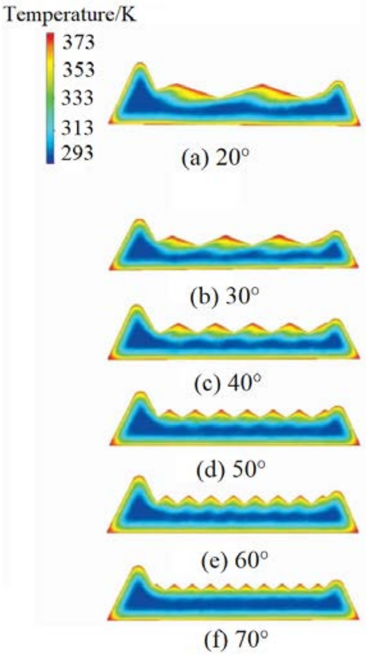

Figure 5. Temperature contour at 16 mm from the inlet of thermal storage element.

3.2 Influence of ripple width

3.2.1 Velocity nephogram

When the inlet wind speed is 10 m/s, the ripple angle is 60°, and the outlet velocity nephogram of the heat storage channel when the ripple width is 6, 7, 8, 9 and 10 mm is shown in **Figure 6** respectively.

It can be seen from **Figure 6** that with the increase of ripple width, the outlet velocity of the heat storage channel increases. When the ripple width is 6–10 mm, the average velocity of the outlet section of the heat storage channel is 9.48, 9.64, 9.87, 9.98 and 10.01 m/s respectively.

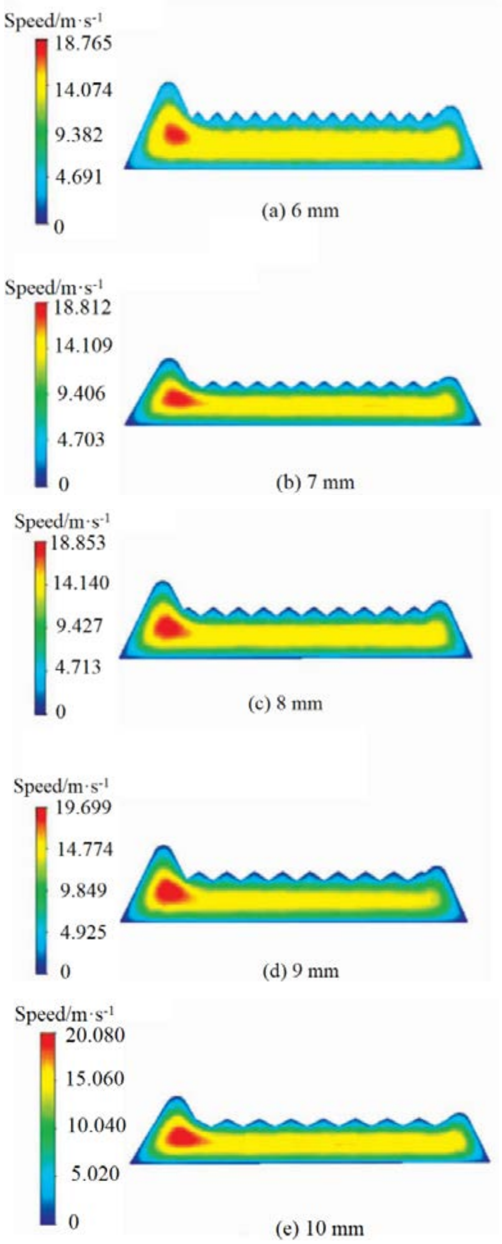

Figure 6. Contour of lateral velocity at the outlet of thermal storage element.

When the ripple width is 10 mm, the outlet speed of the heat storage channel is the highest, because the heat transfer effect is good, the air volume expands more, and the cross-sectional flow rate increases. According to the field synergy theory[20], compared with other ripple widths, the velocity field and temperature gradient field of the 10 mm width heat storage element have better coherence and stronger convective heat transfer performance.

3.2.2 Temperature nephogram

When the inlet wind speed is 10 m/s, the corrugated angle is 60°, and the corrugated width of the heat storage element is 6, 7, 8, 9 and 10 mm, the 14 mm temperature cloud diagram at the inlet of the heat storage channel is shown in **Figure 7**.

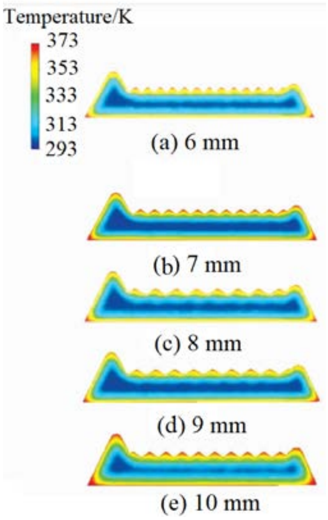

Figure 7. Temperature contour at 14 mm of the inlet of thermal storage element.

In fluent software, using the report function in **Figure 7**, the average temperature at the 14 mm section at the inlet of the heat storage channel with a ripple width of 6, 7, 8, 9 and 10 mm is 316.80, 318.78, 319.00, 319.44 and 319.75 K respectively. When the ripple width is 10 mm, the heat exchange performance of the heat storage element is the best, and the heat exchange performance of the 6 mm heat storage element is the worst. Increasing the ripple width can increase the contact area between air and heat storage elements, which is conducive to enhancing convective heat transfer.

4. Heat transfer and flow characteristics

4.1 Influence of corrugation angle on heat transfer coefficient and resistance coefficient

Numerical simulation is carried out by changing the inlet velocity of the heat storage element with a corrugated inclination of 20°–70°. Then use the report function in fluent software to obtain the parameters such as pressure loss and convective heat transfer coefficient of all heat storage elements.

The variation of resistance coefficient of heat storage elements with different corrugated inclination with Reynolds number is shown in **Figure 8**. It can be seen from **Figure 8** that the resistance coefficient of heat storage elements with different corrugated angles decreases with the increase of Reynolds number. When the corrugated angle is 20°–60°, the resistance coefficient of heat storage elements increases with the increase of the degree of corrugated angle, of which 40° and 50° increase relatively more. The drag coefficient decreases when the ripple angle is 70° compared with 60°, less at low Reynolds number and more at high Reynolds number. When the corrugated angle is 70°, the internal structure of the heat storage channel is not easy to cause air vortex, and the local pressure loss is small. Therefore, the resistance coefficient is reduced. The flow performance of the heat storage element is the best when the ripple angle is 20° and the worst when it is 60°. Comparing **Figure 8** with moody figure, the results are consistent, which proves that the results are reliable.

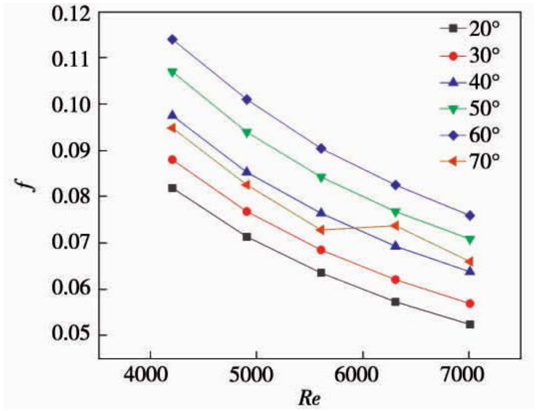

Figure 8. Relationship between resistance coefficient and corrugation angle.

The variation of Nusselt number with Reynolds number of heat storage elements with different corrugated inclination is shown in **Figure 9**. It can be seen from **Figure 9** that the Nusselt number of heat storage elements with different corrugated inclination increases with the increase of Reynolds number. When the corrugated inclination is 20°–60°, with the increase of the degree of corrugated inclination, the Nusselt number of heat storage elements increases and the convective heat transfer performance improves. Taking the working condition of inlet speed of 10 m/s as an example, compared with 20°, the Nusselt number of 30°–70° corrugated heat storage elements increases by 1.22%, 5.01%, 8.62%, 12.37% and 2.33% respectively. When the corrugated angle is 70°, part of the air flows directly from the heat storage channel, with less heat exchange, so the Nusselt number increases less. The heat transfer performance is the best when the wavy angle is 60°. The wavy angle is more conducive to the disturbance of the air, making the boundary layer smaller and the heat transfer more sufficient.

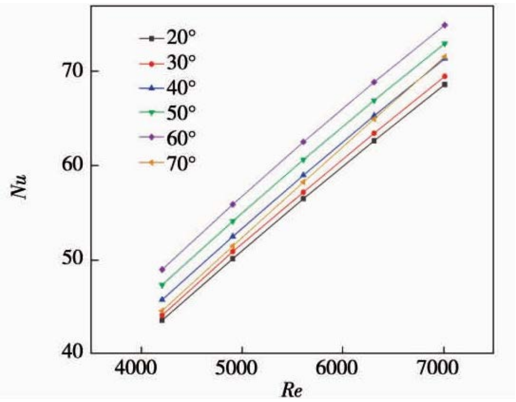

Figure 9. Relationship between Nusselt number and corrugation angle.

4.2 Effect of ripple width on heat transfer coefficient and resistance coefficient

Change the inlet velocity of heat storage elements with different ripple widths, and conduct numerical simulation respectively. The change of resistance coefficient of heat storage elements with different ripple widths with Reynolds number is shown in **Figure 10**. It can be seen from **Figure 10** that the resistance coefficient of the heat storage element increases with the increase of the ripple width. Taking the inlet speed of 10 m/s as an example, compared with the ripple width of 6 mm, the resistance coefficient of 10 mm heat storage element increases by only 0.83%, indicating that the ripple width has little effect on the flow resistance of heat storage element.

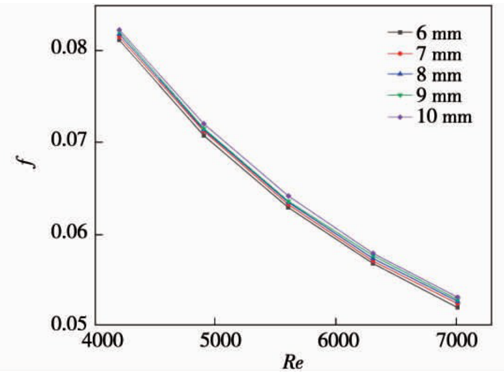

Figure 10. Relationship between resistance coefficient and ripple width.

The relationship between Nusselt number and Reynolds number of heat storage elements with different ripple widths is shown in **Figure 11**. It can be seen from **Figure 11** that with the increase of ripple width, the Nusselt number of heat storage elements increases, especially when it increases from 6 mm to 7 mm, an increase of 23.9%.

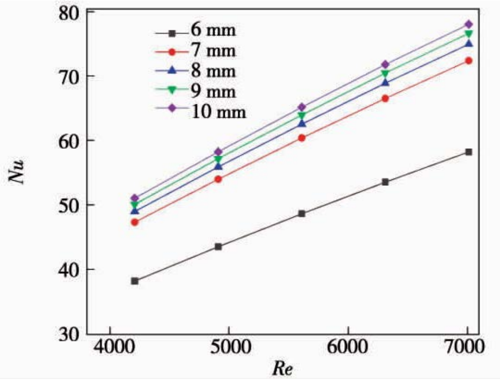

Figure 11. Relationship between Nusselt number and ripple width.

4.3 Numerical simulation reliability verification

In order to verify the reliability of the numerical simulation, the simulation results are compared with the simulation experimental results in literature[12]. When the ripple angle increases from 15° to 60°, the resistance coefficient increases and the Nusselt number increases. The simulation results are basically consistent with this paper, indicating that the conclusion is reliable.

5. Conclusion

(1) When the corrugation angle increases from

20° to 60°, the resistance coefficient increases, the Nusselt number increases, and the heat transfer performance of the heat storage element improves. When the inlet speed is 6 m/s, compared with the ripple inclination of 60°, the resistance coefficient of 70° is reduced by 11.3%, and the Nusselt number is reduced by 9.81%.

(2) When the ripple angle is 60°, when the ripple width of the heat storage element increases from 6 mm to 10 mm, the resistance coefficient increases and the Nusselt number increases, and the increase of Nusselt number is much higher than that of the resistance coefficient.

(3) Both the corrugation angle and the corrugation width are important factors affecting the Nusselt number of heat storage elements. Compared with the corrugation width, the corrugation angle has a greater impact on the resistance coefficient.

Acknowledgement

This work was supported by Hebei Natural Science Foundation Project (E2019209522), Hebei Provincial Professional Degree Teaching Case (Library) Project (KCJSZ2018059).

Conflict of interest

The authors declared no conflict of interest.

References

1. Shu S. Huizhuanshi kongqi yureqi huanre yuanjian shouming yingxiang yinsu (Chinese) [Factors affecting the life of heat exchange elements of rotary air preheater]. Science and Technology Innovation and Application 2019; (19): 74–76.
2. Wang Y, Chen G, Wang Z, *et al.* A review on seal technology of rotary air preheaters. Thermal Power Generation 2015; 44(8): 1–7.
3. Wang Q, Wang E, Mao M. Experimental research on friction characteristics of heat transfer elements of rotary air preheater. Boiler Technology 2011; 42(6): 10–12.
4. Chi Z, Pan W. Experimental studies on measuring the cold end metal temperature of 600mw rotating air heater. Proceedings of the CSEE 2002; 22(11): 129–131.
5. Mohammed HA. The effect of geometrical parameters of a corrugated channel with in out-of-phase arrangement. International Communications in Heat and Mass Transfer 2012; 19 (23): 1044–1051.
6. Focke WW, Zachariades J. The effect of the corrugation inclination angle on the thermohydraulic performances of the heat exchangers. Hear Mass Transfer 1985; 28(8): 1469–1479.
7. Yang X, Gao J, Wei R. Experimental study on heat transfer and fluid flow characteristics of cold and elements in air preheater before and after enamel retrofit. Boiler Technology 2016; 47(1): 22–25.
8. Cai M. Comparison of different manners for air preheater leakage control. Boiler Technology 2011; 42(2): 8–13.
9. Wang H, Bi X, Si F, *et al.* Comprehensive air leakage distribution models for rotary air preheaters of 300 MW units. East China Electric Power 2006; 34(1): 44–48.
10. Chen X, Wang L, Yang Y. Influence of flow arrangement pattern on thermal performance of tri-sector rotary regenerative air preheater and deposition rule for ammonium bisulfate. Journal of Engineering for Thermal Energy and Power 2019; 34(8): 102–108.
11. Wang J. Calculation of equivalent diameter in the pipeline. Journal of Liaoning University of Petroleum and Chemical Technology 2005; 25(3): 69–70.
12. Gao J, Zhang L, Wei R, *et al.* Analysis of influence of structure parameters of enamel heat storage elements on their heat transfer and flow characteristics. Journal of North China Electric Power University 2016; 43(3): 76–80.
13. Wei R, Yang X, Gao J, *et al.* Three-dimensional numerical study on the heat transfer and fluid flow of the heat transfer elements of rotary air preheater. Journal of North China Electric Power University 2015; 42(1): 58–62.
14. Qu Z. Numerical simulation of rotary air preheater [PhD thesis]. Beijing: North China Electric Power University; 2014.
15. Zhang Q, Jin X, Wang E, *et al.* Experimental research on thermal performance of heat transfer elements in rotary air preheater. Boiler Technology 2011; 42(3): 6–8.
16. Zhan H, Zhang X, Li Y, *et al.* Fundamentals of engineering heat transfer. Beijing: Sinopec Press; 2014.
17. Zhang L, Nie P, Liu W, *et al.* Single-blow transient test on the thermal-hydraulic performance of the composite corrugated plate. Proceedings of the CSEE 2017; 37(22): 6675–6680.
18. Mao M, Wang E, Wang Q. Experimental research on friction characteristics of the heat transfer elements of rotary air preheater. Boiler Technology 2012; 43(4): 13–15.
19. Gu X. Numerical simulation and experimental study on heat transfer and flow of enamel heat storage element of rotary air preheater [MSc thesis]. Beijing: North China Electric Power University; 2015.
20. Nolan M. Molecular adsorption on the doped (110) ceria surface. Journal of Physical Chemistry C 2009; 113(6): 2425–2432.

Thermal Science and Engineering (2021) Volume 4 Issue 2
doi:10.24294/tse.v4i2.1520

ORIGINAL RESEARCH ARTICLE

Study on combustion characteristics of swirl premixed combustor

Zhihao Zhang, Xiao Liu*, Tiezheng Zhao, Gang Liu, Guangpu Lv, Hongtao Zheng

College of Power and Energy Engineering, Harbin Engineering University, Harbin 150001, China. E-mail: Liuxiao_heu@163.com

ABSTRACT

Taking a certain type of combustion chamber as the research object, the numerical simulation is carried out by using RANS (Reynolds averaged Navier-stokes) and LES (large eddy simulation), and the simulation results of the two numerical methods are compared and analyzed. The research results show that the RANS calculation results can reflect the main flow field characteristics in the combustion field, and have certain engineering significance. LES can reproduce specific flow field details such as the weak axial flow region, accurately simulate the location and strength of the shear layer, simulate the dynamic development process of flame, and capture the dynamic characteristics of the combustion flow field. Compared with RANS, LES has more obvious advantages in numerical simulation of the combustion flow field. Through calculation, the precessing vortex core under this working condition is composed of three relatively independent spiral vortex branches, which excites periodic velocity pulsation and pressure pulsation in the combustion chamber. LES captures the dominant frequency with the precession vortex core of 156 Hz.

Keywords: Swirl Premixed Combustion Chamber; Partial Premixed Combustion; Large Eddy Simulation; Precessing Vortex Core

ARTICLE INFO

Received: 12 September 2021
Accepted: 1 November 2021
Available online: 13 November 2021

1. Introduction

With the increasingly prominent problem of environmental pollution and the increasing awareness of environmental protection around the world, international organizations have Formulated strict air pollutant emission standards for combustion systems, requiring gas turbines and aero-engines to continuously reduce pollutant emission levels. Therefore, low pollutant emission technology has become one of the key technologies with great development prospects. When designing and developing a new generation of gas turbines, manufacturers often adopt lean premixed combustion technology to replace the traditional diffusion combustion[1,2]. The characteristic of lean burn premixed combustion technology is that the fuel and oxidant have been fully mixed before entering the combustion chamber. By controlling the mixing ratio of fuel and oxidant, the flame temperature can be reduced to achieve the purpose of reducing pollutant emissions. However, lean premixed combustion is close to the lean flameout boundary, which is prone to combustion instability[3], so the swirl generated by the cyclone is needed to stabilize the flame. As a typical representative of an advanced combustion chamber, the combustion characteristics of swirl premixed combustion chambers have attracted extensive attention of experts and scholars all over the world.

With the continuous improvement of computer ability, computational fluid dynamics (CFD) has become an indispensable means in practical engineering design and application, playing a huge role. Aiming at the complex physical and chemical process of swirl and combustion coupling in an advanced combustion chamber, the coupling analysis method of turbulence model and combustion model in CFD method can effectively analyze this complex process. Turbulence numerical simulation methods are mainly divided into three categories: direct numerical simulation method (DNS), Reynolds average (RANS) statistical method, and large eddy simulation (LES) method. Limited by the amount of calculation, DNS is mainly applied to the theoretical research of low Reynolds numbers at this stage. RANS method has been widely used in engineering because of its small amount of calculation, but because its calculation results have no time correlation, it cannot capture the dynamic information of a swirling combustion field. LES method is between the two. It uses a low-pass filter function to filter small-scale turbulent motion and directly solve unsteady large-scale vortex motion. It can reproduce the real process of swirl combustion to a certain extent and has broad application prospects.

Wang[4] took the round hole jet as the model and compared the calculation results of DNS, LES, and RANS models for turbulence. The research showed that RANS simulated the first-order statistics (such as the length of the recirculation core) more accurately, but the prediction accuracy of the peak value of the second-order stress was poor. DNS could provide model correction for LES and RANS. He *et al.*[5] used RANS coupling different combustion models to conduct numerical analysis of gas turbine combustion. Yang and Zheng[6] used the RANS model to conduct numerical research on the combustion process of the chemical regenerative cycle combustion chamber, and the calculation results have certain engineering significance.

Balut *et al.*[7] successfully applied LES to the numerical study of industrial gas turbines. The experimental study shows that LES can not only well reproduce the details of the combustion flow field, but also accurately calculate a variety of intermediates in the combustion process, pointing out the direction for the dynamic simulation of the combustion process. Han *et al.*[8] used the LES method to simulate stratified swirl flame, and successfully captured the details of combustion flow field such as vortex breaking and central recirculation zone.

Most studies at home and abroad simply described that the LES numerical method is more accurate than the RANS numerical method, and did not compare the calculation results of the two models in detail. Taking the combustion chamber of an industrial gas turbine as a model for numerical analysis, this paper compares and discusses in detail the simulation of the swirl combustion chamber by RANS and LES, analyzes the reproduction ability of the two numerical simulation methods on the swirl combustion information, summarizes the application scope of the two models, and deeply analyzes the LES numerical results to obtain the transient structure of the combustion flow field and the pressure pulsation information. This method can be used in the later numerical research of the combustion chamber.

2. Mathematical model

In this paper, k-ε model and LES-WMLES model are coupled with the FGM combustion model to simulate the swirling combustion process.

2.1 Realizable k-ε model

Compared with the standard k-ε model, the realizable k-ε model improves the calculation Formula and ε equation of turbulent viscosity, which is suitable for simulating the flow problems such as strong streamline bending, vortex and rotation。 Therefore, the realizable k-ε model turbulence model is applied in the RANS simulation of the combustion chamber in this paper.

The realizable k-ε equation of the model is

$$\frac{\partial(\rho k u_j)}{\partial x_j} = \frac{\partial}{\partial x_j}\left[\left(\mu + \frac{\mu_t}{\sigma_k}\right)\frac{\partial k}{\partial x_j}\right] - \rho\epsilon + S_k \tag{1}$$

$$\frac{\partial(\rho\varepsilon u_j)}{\partial x_j} = \frac{\partial}{\partial x_j}\left[\left(\mu + \frac{\mu_t}{\sigma_\varepsilon}\right)\frac{\partial\varepsilon}{\partial x_j}\right] - \rho C_1 S_\varepsilon - \rho C_2 \frac{\varepsilon^2}{k + \sqrt{v\varepsilon}} + C_{1\varepsilon}\frac{\varepsilon}{k} C_{3\varepsilon} G_b + S_\varepsilon \tag{2}$$

Where: $\sigma_k = 1.0$, $\sigma_\varepsilon = 1.2$, $C_2 = 1.9$, $C_1 = max\left(0.43, \frac{\eta}{\eta+5}\right)$, $\eta = S\frac{k}{\varepsilon}$, $S = \sqrt{2S_{ij}S_{ij}}$.

Where: ρ is the density, kg/m^3; k is turbulent kinetic energy, W/(m·K); ε is turbulent dissipation rate; u_i, u_j are speed, m/s; x_i, x_j are the unit length in each direction; S_k is the source item; μ_t is turbulent viscosity, (N·s)/m^2.

2.2 LES model

Compared with RANS model, LES can capture flow field information more accurately. LES directly solves the large-scale turbulence, and uses the sub-grid model to solve the remaining small-scale turbulence. The filtered N-S equation can be expressed as

$$\frac{\partial\bar{\rho}}{\partial t} + \frac{\partial\bar{\rho}\tilde{u}_i}{\partial x_i} = 0 \tag{3}$$

$$\frac{\partial\bar{\rho}\tilde{u}_i}{\partial t} + \frac{\partial(\bar{\rho}\tilde{u}_i\tilde{u}_j)}{\partial x_j} = -\frac{\partial\sigma_{ij}}{\partial x_j} - \frac{\partial\bar{p}}{\partial x_i} + \frac{\partial^{sgs}_{ij}}{\partial x_j} \tag{4}$$

$$\frac{\partial\bar{\rho}\widetilde{Y_K}}{\partial t} + \frac{\partial(\bar{\rho}\widetilde{Y_K}\tilde{u}_j)}{\partial x_j} = \frac{\partial}{\partial x_j}\left(\bar{\rho}\widetilde{D_k}\frac{\partial\widetilde{Y_k}}{\partial x_j}\right) - \frac{\partial}{\partial x_j}\left(\bar{\rho}\widetilde{u_j Y_k} - \bar{\rho}\tilde{u}_j\widetilde{Y_k}\right) + \overline{\omega_k}, k = 1, \dots, N \tag{5}$$

$$\frac{\partial\bar{\rho}\tilde{h}}{\partial t} + \frac{\partial(\bar{\rho}\tilde{u}_j\tilde{h})}{\partial x_j} = \frac{D\bar{p}}{Dt} - \frac{\partial}{\partial x_j}\left(\bar{\rho}\widetilde{u_j h} - \bar{\rho}\tilde{u}_j\tilde{h}\right) + \frac{\partial}{\partial x_j}\left(\overline{\rho a}\frac{\partial\tilde{h}}{\partial x_j}\right) + \overline{\tau_{ij}\frac{\partial u_i}{\partial x_j}} \tag{6}$$

In LES model, Bossinesq hypothesis τ_{ij}^{sgs} is used to describe:

$$\tau_{ij}^{sgs} = \bar{\rho}\left(\widetilde{u_i u_j} - \tilde{u}_i\tilde{u}_j\right) = -2\mu_{sgs}\widetilde{S_{ij}^{D}} + \frac{2}{3}\bar{\rho}k\delta_{ij} \tag{7}$$

The algebraic wall modeled LES model (WMLES) uses the Reynolds average method to simulate the convection field in the boundary layer, while the large eddy simulation method is used outside the near wall region, and its eddy viscosity is defined as

$$\mu_{\mathrm{t}} = \min\left[(\kappa d_{\mathrm{w}})^2, (C_{\mathrm{Smag}}\Delta)^2\right] \cdot S\left\{1 - e^{[-(y^+/25)^3]}\right\} \tag{8}$$

Where: d_{w} is the distance between the point and the wall, S is the strain rate, parameter κ = 0.41, C_{smag} = 0.2 and filter size Δ is selected according to specific flow field conditions:

$$\Delta = min\left(max(C_w \cdot d_w \cdot C_w \cdot h_{max}; h_{wn}\right); h_{max} \tag{9}$$

Where: h_{wn} is the grid step along the normal direction of the wall, h_{max} is the maximum step of the wall grid, and C_{w} is the fixed value of 0.15.2.3 FGM (flamelet generated manifold) model

The FGM model refers to the laminar flame surface method, and considers that the three-dimensional flame has a one-dimensional structure in essence, and the turbulent flame surface is the statistical average of the laminar flame surface, so the one-dimensional flame can be used to construct the reaction mechanism subspace. FGM model can consider the influence of convection and diffusion, and it has good accuracy in both high-temperature and low-temperature regions. In addition, FGM can also be naturally extended from premixed combustion model to partial premixed combustion model, rather than rough and simple combination[9], so its applicability is wider and closer to reality. FGM partial premixed combustion model is adopted in this paper.

In order to use FGM method to simulate the combustion flow field, it is necessary to use chemical reaction mechanism to establish laminar small flame form. In this paper, GRI 3.0 mechanism (detailed chemical reaction mechanism of methane) is used; the mixed score can be defined as[10]:

$$Z = \frac{Z_i - Z_{i,ox}}{Z_{i,fuel} - Z_{i,ox}} \tag{10}$$

Where: Z_i is the relative atomic mass of component i, and the subscripts OX and fuel represent oxidant and fuel, respectively. The mixing fraction is a conservative scalar, which is only affected by diffusion and convection. Its transport equation is

$$\frac{\partial}{\partial t}(\rho Z)+\frac{\partial}{\partial_{xi}}(\rho u_i Z)=\frac{\partial}{\partial_{xi}}(\rho D\frac{\partial Z}{\partial_{xi}}) \tag{11}$$

Where, D is the laminar diffusion coefficient.

The selection of reaction progress variable C is defined based on components, as shown in Formula (12):

$$C=\frac{\sum_k \alpha_k (Y_k - Y_k^{\mathrm{u}})}{\sum_k \alpha_k (Y_k^{\mathrm{eq}} - Y_k^{\mathrm{u}})}=\frac{Y_C}{Y_C^{\mathrm{eq}}} \tag{12}$$

3. Physical model and boundary conditions

3.1 Introduction to a model combustion chamber

The central section of a model combustion chamber is shown in **Figure 1**. In order to facilitate the installation and testing of test equipment, the model combustion chamber simplifies the flame tube of the prototype combustion chamber[11]. The length and width of the cross section of the combustion chamber are 0.165 m, and the length of the transition section is 0.188 m. The radial hydro cyclone is installed at the head of the combustion chamber and is composed of 12 fixed wedges with a swirl number of 1.3. The premixed fuel nozzle is located in the rectangular channel near the inlet of the hydro cyclone. The fuel is injected into the inter blade channel to mix with the incoming air, and then flows into the combustion chamber for combustion after passing through the premixed section.

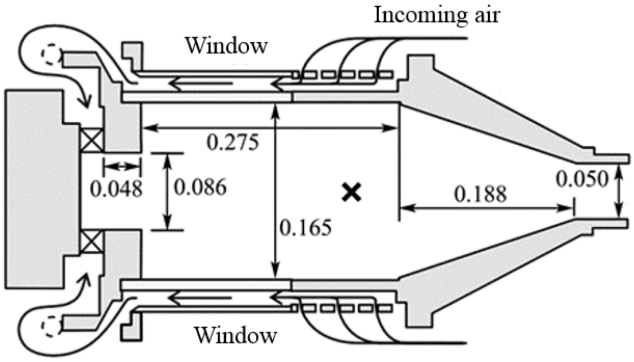

Figure 1. Combustor[11] (unit: m).

3.2 Grid division

As shown in **Figure 2**, the CFD pre-processing software ICEM is used to divide the global structured grid of the calculation domain, which includes the radial hydro cyclone, the premixed section, the model combustion chamber and the outlet of the transition section. The hydro cyclone and the shear layer area are meshed to increase the simulation accuracy, and the rougher mesh is used in the outlet area of the combustion chamber to improve the calculation efficiency. In this paper, the same set of grids is used to simulate RANS and LES, and the results of the two turbulence simulation methods are compared. The specific parameters of the grid are shown in **Table 1**:

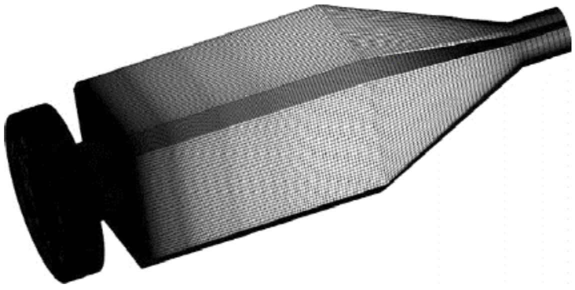

Figure 2. Grid of combustor calculation domain.

Table 1. Grid parameters

Grid quantity/pc	$\Delta x_{\min}$/mm	$\Delta x_{\max}$/mm	$\Delta y_{\min}$/mm	$\Delta y_{\max}$/mm	$\Delta z_{\min}$/mm	$\Delta z_{\max}$/mm
7,315,859	0.053	4.340	0.053	4.340	0.125	6.210

3.3 Boundary conditions

The inlet section of air and fuel is defined as the mass flow inlet, and the test fuel is German natural gas[11] The fuel composition is shown in **Table 2**. Inlet air pressure p = 0.3 MPa, air mass flow 175.0 g/s, fuel mass flow 6.2 g/s. The air temperature is 685.0 K and the fuel temperature is 319.8 K. The outlet adopts the boundary condition of pressure outlet, and the pressure loss is 1%.

Table 2. Components in German natural gas

Component	**Mole fraction/%**
CH_4	96.970
C_2H_6	1.553
C_3H_8	0.400
CO_2	0.270
N_2	0.753

4. Result analysis

4.1 Comparison of numerical simulation results between LES and RANS

Stopper *et al.*[11] monitored the speed, temperature and mixed scores etc. of the four positions. The distances between different straight lines and the duty plane are 1.21 *D*, 1.44 *D*, 1.66 *D* and 2.00 *D*, respectively, and *D* is the diameter of the premixed section. **Figures 3** and **4** show the numerical results of RANS and the comparison of LES time average velocity and temperature distribution with experimental data.

It can be seen from **Figure 3** that the calculated results better reflect the time average axial velocity distribution in the combustion chamber, and the calculated value of the velocity peak $u_{\max}$ is close to the experimental value. There is a big difference between the axial velocity test value and the numerical simulation result at position 3, and the calculation error is about 5%. The center and corner vortex recirculation region in the combustion flow field are accurately reproduced. There is a symmetrical central recirculation zone in the center of the combustion chamber, and the width of the central recirculation zone obtained by simulation is slightly wider than that of the test. The calculation error of RANS in the width of the recirculation zone is about 7%, and the calculation error of LES is small, about 2%. Due to the high swirl intensity, a local negative velocity zone appears near the central axis. This strong swirl in the combustion field will cause a large number of high-temperature burned products to reflux, and preheat and ignite the premixed gas upstream of the combustion chamber.

It can be clearly seen from **Figure 3** that, compared with RANS, LES is in good agreement with the experimental data, which can well reflect the details of the velocity field, well predict the range and strength of the shear layer, and also capture the weak central recirculation zone near the central axis downstream of the combustion field, which is consistent with the results of the boundary limited swirl test observed in the early test[12]. However, RANS can only roughly describe the shape of the central recirculation zone and the angular vortex recirculation zone, the distribution law and development trend of rough reaction speed, temperature and other parameters, and cannot accurately reproduce the internal details and recirculation characteristics of the central recirculation zone, which will have a great impact on the prediction of the combustion field and the distribution of components in the combustion chamber, especially the time independent calculation method of RANS cannot reflect the details of the combustion dynamic process. The dynamic process of flame stability and ignition flameout cannot be captured, and the degree of application is limited.

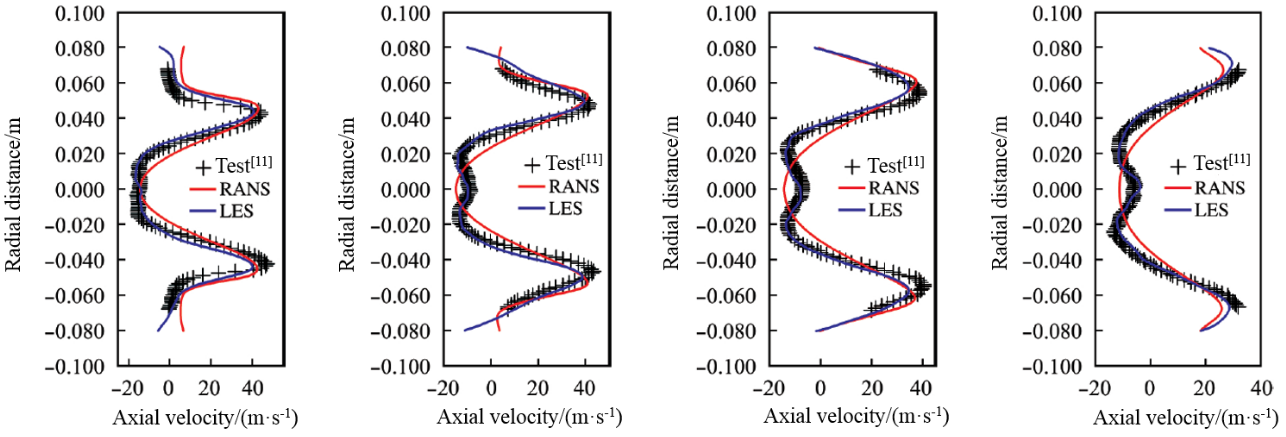

(a) Position 1 (b) Position 2 (c) Position 3 (d) Position 4

Figure 3. Axial velocity indifferent positions.

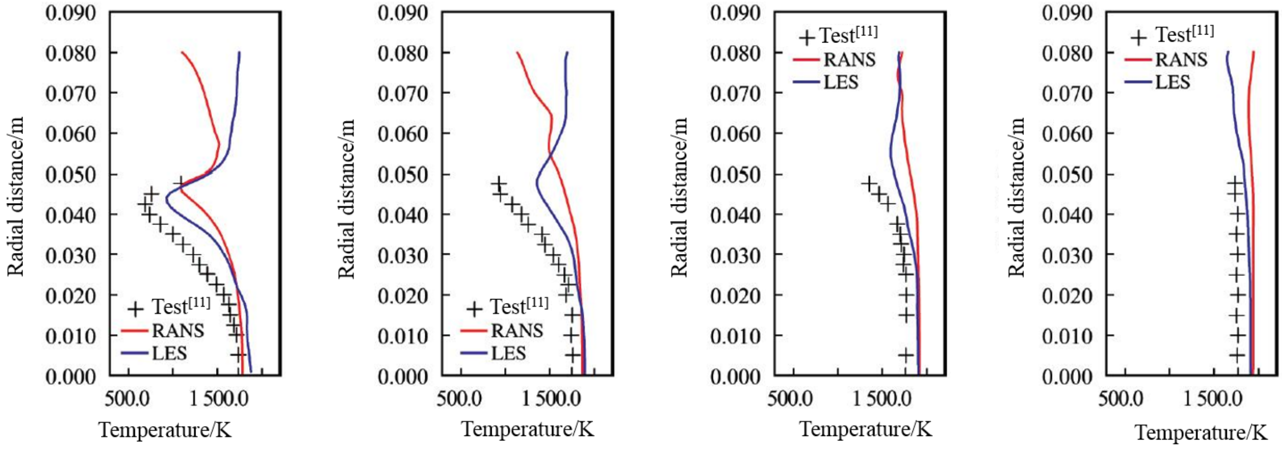

(a) Position 1 (b) Position 2 (c) Position 3 (d) Position 4

Figure 4. Temperature indifferent positions.

4.2 Reproduction of flow field details

Figure 5 shows the instantaneous combustor head velocity, mixing fraction and temperature simulated by LES. The air carries the fuel injected into the inter blade passage through the cyclone into the combustion chamber, and forms a shear layer along the wall of the premixed chamber. As shown in **Figure 5(b)**, the vortex generated by the strong momentum exchange in the shear layer carries the fuel downstream of the combustion chamber. The fuel and air are strongly mixed in the shear layer to form a premixed gas and flow downstream. When the premixed gas meets the high-temperature products entrained back downstream, it begins to burn rapidly. The recirculation effect of strong swirling flow and strong velocity pulsation in the shear layer stabilize the flame position near the shear layer. From the mixture fraction distribution diagram and temperature cloud diagram, it can be seen that the combustion mainly occurs at the position where the equivalence ratio is less than 1 (the mixture fraction is less than 0.055), and the combustion chamber is mainly in lean combustion state.

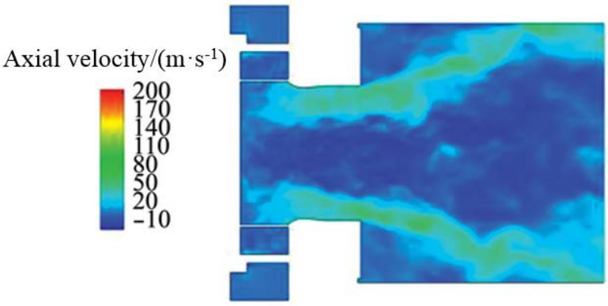

(a) Axial velocity

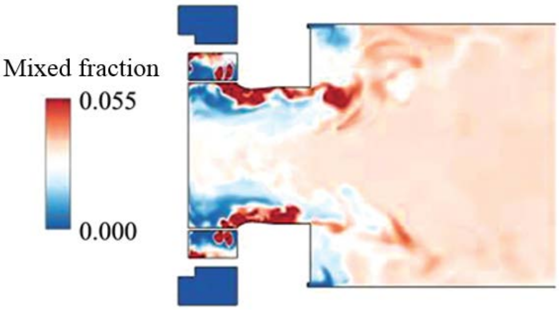

(b) Mixed fraction

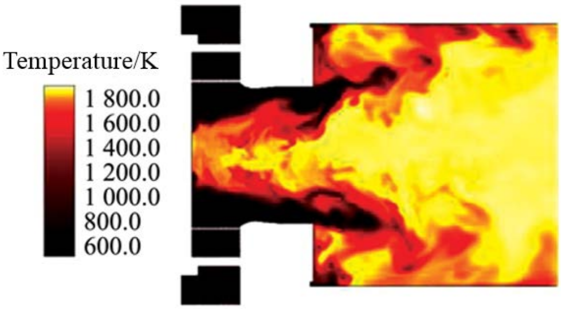

(c) Temperature

Figure 5. Contour of axial velocity mean mixture fraction and temperature in the combustor.

High swirling flow is often accompanied by the formation of precession vortex core. The vortex moves periodically around the central axis, which will cause velocity and pressure pulsation in the combustion chamber, affect the combustion process, and easily cause combustion oscillation, which will not only increase the emission of pollutants in the combustion process, but also have an adverse impact on the combustion equipment.

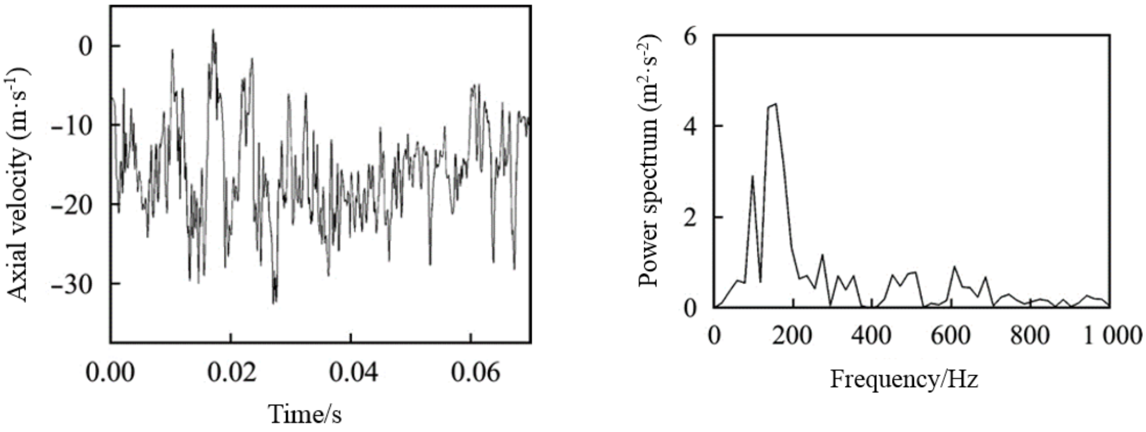

(a) Axial velocity time series distribution

(b) Axial velocity power spectral density

Figure 6. Axial velocity at the inner shear layer.

LES simulates the premixed combustion flow field instantaneously, and selects a point on the inner shear layer to monitor the change of its axial velocity with time. As shown in **Figure 6(a)**, the FFT transformation of the axial velocity time series distribution is carried out to obtain the axial velocity power spectral density. According to **Figure 6(b)**, the main frequency of the axial velocity fluctuation is 156 Hz, which is the frequency of the precession vortex core of a certain combustion chamber under this working condition. The axial velocity fluctuation in the combustion flow field is caused by the periodic falling off of the precession vortex core. The main difference between the precession vortex core and the spiral vortex is that the precession vortex core rotates around the central axis, the fluid around the vortex core rotates around its internal vortex axis, and the spiral vortex only makes a spiral motion around its own axis.

Figure 7 shows the spatial three-dimensional structure of the precession vortex core using the pressure contour method. The precession vortex core is composed of the core of the main spiral vortex and the branches of the spiral vortex. The main spiral vortex starts from the duty plane of the premixed combustion chamber and develops downstream. With the increase of distance, the main spiral vortex splits into several branches, that is, multiple relatively independent small spiral vortices, which rotate around the central axis to form a precession vortex core structure. As shown in **Figure 8**, there are three low-pressure areas in the throat of the combustion chamber, namely the three branches of the main spiral vortex. The vortex centers of the three places are all off-axis and located near the inner shear layer. These three independent small spiral vortices spiral along their respective central axes and rotate around the central axis of the combustion chamber, causing periodic pressure and velocity pulsations in the combustion flow field, making the velocity pulsation and mixing transportation process of the shear layer more intense. Therefore, the capture of precession vortex core is very important for the study of combustion characteristics of swirling combustion field, especially for the study of flame dynamic characteristics.

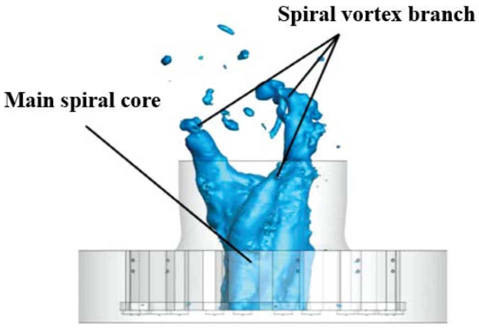

Figure 7. Precessing vortex core structure.

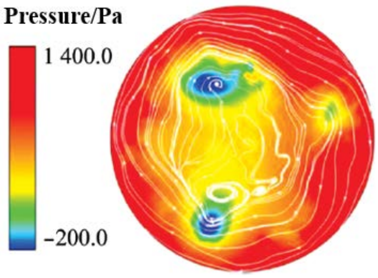

Figure 8. Pressure contour and streamlines of the combustor throat.

5. Conclusion

Based on CFD numerical simulation technology, this paper studies the numerical simulation of the combustion field of the swirl premixed combustion chamber. For a certain type of combustion chamber, the test results of the combustion chamber are reproduced by using the coupling calculation method of LES, RANS and FGM combustion model, respectively. The calculation results of the two numerical methods are compared, and the conclusion is obtained.

(1) The results of RANS can roughly describe the development trend of velocity field and temperature field, and can accurately calculate the size of velocity value, the location and strength of shear layer. It has certain engineering value.

(2) LES can accurately reproduce the detailed structure of the combustion flow field, and can capture the weak central recirculation zone at the axis of the restricted flow field. It is more accurate to calculate the range of shear layer. The dynamic calculation results of LES can capture the dynamic characteristics of combustion flow field, which is more in line with the needs of basic researchers.

(3) LES instantaneous numerical simulation can capture the precession vortex core in the strong swirl combustion flow field and analyze the dynamic characteristics of the flame. The numerical simulation shows that the dominant frequency of the precession vortex core is 156 Hz.

Acknowledgement

The National Science and Technology Major Special Fund Project (2017-III-0006-0031); the Central University Fundamental Research Fund Special Fund Project (3072019CFJ0307).

Conflict of interest

The authors declare that they have no conflict of interest.

References

1. Luciano E, Ballester J. Analysis of the dynamic response of premixed flames through chemiluminescence cross-correlation maps. Combustion and Flame 2018; 194: 296–308.
2. Patel N, Menon S. Simulation of spray–turbulence–flame interactions in a lean direct injection combustor. Combustion and Flame 2008; 153(1–2): 228–257.
3. El-Asrag HA, Iannetti AC, Apte SV. Large eddy simulations for radiation-spray coupling for a lean direct injector combustor. Combustion and Flame 2014; 161(2): 510–524.
4. Wang X. Investigation on the turbulance characteristics in the near field of round jet flow with DNS and RANS LES [MSc thesis]. Hangzhou: Zhejiang University; 2010.
5. He W, Zheng H, Cai L.Analysis of turbulent combustion model on numerical simulation of combustion chamber. Journal of Thermal Science and Technology 2011; 10(4): 360–365.
6. Yang H, Zheng H. Structural design and numerical simulation of dual-fuel gas turbine nozzle. Journal of Thermal Science and Technology 2010; 9(3): 78–85.
7. Bulat G, Jones WP, Marquis AJ. NO and CO formation in an industrial gas-turbine combustion chamber using LES with the Eulerian sub-grid PDF method. Combustion and Flame 2014; 161(7): 1804–1825.
8. Han X, Laera D, Morgans AS, *et al*. Flame macrostructures and thermoacoustic instabilities in stratified swirling flames. Proceedings of the Combustion Institute 2019; 37(4): 5377–5384.
9. Fluent Inc. Fluent user's guide.Canonsburg: PA: Ansys; 2017.
10. Bilger RW. Future progress in turbulent combustion research. Progress in Energy and Combustion Science 2000; 26(4–6): 367–380.
11. Stopper U, Meier W, Sadanandan R, *et al*. Experimental study of industrial gas turbine flames including quantification of pressure influence on flow field, fuel/air premixing and flame shape. Combustion and Flame 2013; 160(10): 2103–2118.
12. Syred N, Beer JM. Combustion in swirling flows: A review. Combustion and Flame 1974; 23(2): 143–201.

Thermal Science and Engineering (2021) Volume 4 Issue 2
doi:10.24294/tse.v4i2.1521

CASE REPORT

Thermo-exergetic evaluation of a compact pyrotubular steam generator

Velázquez-González Alejandro*, Corrales-Suárez Jorge Michel, Pérez-Molina Leonardo Rafael

Centro de Estudios de Eficiencia Energética y Procesos Tecnológicos, Universidad de Las Tunas, Cuba. E-mail: alevel2014@gmail.com

ABSTRACT

One of the most important variables to know how efficient a thermal machine is the exergy. In practice, it is one of the least controlled variables. In this research, a thermal exergy study was carried out in a compact pyrotubular steam generator. To achieve this, an energy mass balance and entropy balance were carried out. The energy balance was carried out by direct and indirect methods. The percentages of the exergies of each working substance in the process are specified. The energy yield by the direct method was 0.901 and by the indirect method was 0.882, since each method has its role in the energy analysis. The irreversibilities in the process were 26%. The exergetic efficiency was 0.39, conditioned by a complete combustion in the hearth. It was demonstrated that the steam generator for the real operating conditions is oversized.

Keywords: Pyrotubular Steam Generator; Energy; Entropy; Exergy; Irreversibilities; Performance

ARTICLE INFO

Received: 25 September 2021
Accepted: 6 November 2021
Available online: 28 November 2021

1. Introduction

In the early 1960s, there was a growing worldwide awareness that industrial growth and energy production from fossil fuels are accompanied by the release of potentially harmful pollutants into the environment[1].

There is a strong relationship between energy efficiency and environmental impact, since for the same services or products, lower resource use and pollution are usually associated with higher energy efficiency[2].

The growing concern for energy savings has encouraged a critical examination of the methods used to evaluate and increase the efficiency of industrial processes. In response, attention has recently focused on analysis techniques based on the Second Principle of Thermodynamics, in particular, on the concept of exergy[3]. Exergy is fundamentally the property of the system that provides the maximum potential that can be extracted from the system when brought to a thermodynamic equilibrium state from a reference state[4,5].

In recent years, due to the scarcity of fossil fuels and their logical increase in price, the importance of developing thermal systems that make effective use of these non-renewable energy resources such as oil, natural gas and coal has become evident. The method of exergetic analysis is particularly suitable to achieve an efficient use of energy resources, since it allows determining the location, type and real magnitude of their loss and waste. A pyro-tube or fire-tube steam generator is a thermal machine that produces steam. This steam is generated when the combustion gases pass through the inside of the tubes, which are bathed in water, from where the saturated steam is produced, which is conducted through the distribution lines to the consumers, which are generally: kitchens, dry cleaners, hospitals, among others.

The efficient use of energy resources will be achieved by reducing as much as possible the destruction of exergy in the systems, i.e., reducing the irreversibilities of the processes occurring within the systems. This will allow focusing attention on those aspects of the operation of the system under analysis that offer the greatest opportunities for improvement.

The objective of the research was to determine if the steam generator is adequate for the real operating and process conditions, as well as the opportunities to increase its efficiency. It was hypothesized that by determining the energetic and exergetic performances of the steam generator, it is possible to know the magnitude of the influence of the operational variables that affect it.

2. Materials and methods

The investigation was carried out on a compact pyrotubular steam generator model CMS-660. This works with regular diesel fue[6] and its gravimetric composition was obtained from the data sheet provided by the supplier. It has a nominal capacity for steam production of 660 kg/h, produces saturated steam with a pressure of 0.49 MPa and has a heat exchange surface with the fluid to be heated of 19.6 m^2. The cylindrical outer walls have an operating temperature of 34 ℃ and the rest of the walls 42 ℃. The feedwater is preheated by saturated steam extraction and enters the generator at 80 ℃. Condensate from the process is not recovered due to a design error in the plant. The exhaust gas temperature is 200 ℃. The properties of all working substances entering and leaving the steam generator must be known in order to perform mass, energy, entropy and exergy balances (**Figure 1**).

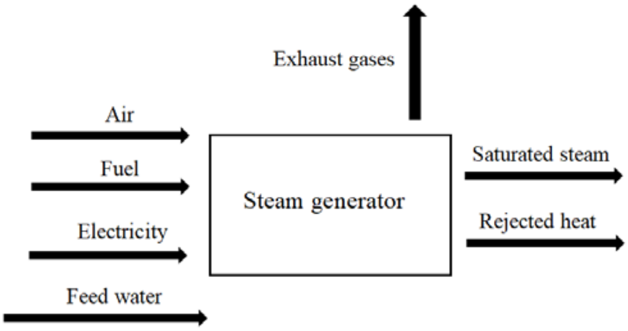

Figure 1. Basic scheme of the system to be studied.

2.1 Mass balance

Fuel, feedwater and saturated steam flows were obtained from direct measurements and others by applying mass balance. To determine the mass flow of air, the combustion was considered to be complete, the actual excess air coefficient was measured and the theoretical air volume to combust one kilogram of fuel was determined. By multiplying the theoretical air volume by the excess air coefficient, the actual air volume was obtained. The actual air volume was multiplied by the mass flow of the fuel entering the boiler and the volumetric air flow was obtained. This volumetric flow rate is multiplied by the air density to obtain the air mass flow rate. The exhaust gas mass flow is obtained by equation (1):

$$G_{aire} + G_{aa} + G_{comb} = G_{vap} + G_{esc} \tag{1}$$

2.2 Energy balance

Applying the law of conservation of energy, equation (2) is obtained:

$$G_{aire} \cdot h_{aire} + G_{aa} \cdot h_{aa} + G_{comb} \cdot PCI + Pelect = + \dot{q}_{rech} + G_{vap} \cdot h_{vap} + G_{esc} \cdot h_{esc} \tag{2}$$

The enthalpy of air was obtained from Cengel table A17[1,7], those of feed water and water vapor were obtained from table A4 of the Cengel book[7]. The enthalpy of the exhaust gases was determined from gas analyzer measurements. The lower heating power (LHP) of the fuel was checked by equation (3)[8,9].

$$PCI = 339.2C + 1030.4H - 108.9(0 - S) - 25.14W \tag{3}$$

The rejected heat was calculated by Newton's cooling equation (equation 4). The boiler walls are at relatively low temperatures, therefore, only the heat rejected by the natural convection mechanism was taken into account (equation 4)[7,10].

$$\dot{q}_{rech} = h \cdot A_s\,(T_s - T_f) \tag{4}$$

Where:

h = Overall heat emission coefficient (W/(m^2·K))

A_s = Heat exchange surface with the environment (m^2)

T_s = Surface temperature (K)

T_f = Surface surroundings temperature(K)

2.2.1 Calculation of energy yield by the direct method

The calculation of the energy efficiency of the steam generator was calculated by equation (5)[11]:

$$\eta_{gv} = \frac{G_{vap} \cdot h_{vap} - G_{aa} \cdot h_{aa}}{G_{aire} \cdot h_{aire} + G_{comb} \cdot PCI + P_{elect}} \tag{5}$$

2.1.2 Calculation of energy yield by the indirect method

This method can be applied without the need to know steam production and fuel consumption[12].

The yield η_{gv}^{bruto} in this case was determined by equation (6):

$$\eta_{gv}^{\text{bruto}} = 100 - (q_2 + q_3 + q_4 + q_5 + q_6 + q_7), \% \tag{6}$$

Table 1. Equations used to test the different types of losses[9]

Type of loss	Equation	
q_2	$q_2 = \dfrac{(h_{esc} - \alpha_{ge} \cdot h_{af})(100 - q_4)}{Q_d}$	(7)
q_3	$\dfrac{V_{gs} \cdot (126 \cdot CO + 108 \cdot H_2 + 358.2 \cdot CH_4)(100 - q_4)}{Q_d}$	(8)
q_4	This loss is due to the fact that sometimes, in a real combustion, a small part of the combustible substances do not combust.	
q_5	$q_{5\text{ nom}} \dfrac{D_{nom}}{D_{\text{real}}}$	(9)
q_6	This loss generally occurs when solid fuels are burned and to a lesser extent in liquid fuels.	
q_7	This loss is disregarded, since for pyro-tubular steam generators it does not reach 2% of the total losses.	

Where[13]:

q_2 = Heat losses with exhaust gases

q_3 = Heat losses due to incomplete chemical combustion

q_4 = Heat losses due to incomplete mechanical combustion

q_5 = Radiation and convection heat losses to the environment

q_6 = Losses with the physical heat of the ashes

q_7 =Losses due to purging

The equations used to determine the energy losses are shown in **Table 1**.

(1) Energy balance

It was carried out to know the irreversibilities of the system. The reference environment is 298.15 K temperature and one technical atmosphere pressure.

$$\sum B_{ent} = \sum B_{sal} = I \tag{10}$$

The exergy of a matter flow can be divided into different components[14-16]:

$$B = B_C + B_P + B_F + B_Q \tag{11}$$

Where:

B, B_C, B_P, B_F and B_Q equal the total exergy of the substance, kinetic exergy, potential exergy, physical exergy and chemical exergy respectively (kW).

For the installation to be analyzed, the resulting equation (12) is:

$$B_{\text{aire}} + B_{\text{aa}} + B_{\text{comb}} + B_{\text{elect}} = B_{\text{qrech}} + B_{\text{esc}} + B_{\text{vap}} + I \tag{12}$$

For air, the physical exergy was neglected because it has practically the same properties as the reference environment (**Table 2**). With the outlet pressure of the saturated steam and with the title, the entropy of the feedwater is located in Table A4 of the book by Çengel and Boles[7]. In fuel**,** for the specific chemical exergy**,** there is a general expression given in Annex C of the book of Kotas[15]. Szargut and Styrylska[17] assume that the ratio of chemical exergy to the net calorific value of solid and liquid industrial fuels, is the same as that of pure chemicals having the same proportions of chemical components[15]. For exhaust gases (**Table 2**). The equations used to determine the exergies of each substance are presented in **Table 2**.

Table 2. Equations used to determine the different types of exergies of working substances[15]

Working substance	**Equation**	
Air	$b_{aire}^{q} = \sum (n_i b_{xi}^{q}) + RT_0 \sum x_i \, ln \, x_i$ $b_{aa} = b_{aa}^{q} + b_{aa}^{f}$	(13)
Feed water	$b_{aa}^{f} = h_{aa} - h_0 - T_0(s_{aa} - s_0)$ $b_{aa}^{q \text{ st corrg}} = b_{aa}^{qst} \frac{T}{T_0} - h^{st} \frac{T - T_0}{T_0}$	(14)
Saturated steam	$b_{\text{vap}} = b_{vsat}^{q} + b_{\text{vap}}^{f}$	(15)
Fuel	$\varphi = \frac{b_{\text{comb}}^{q}}{PCI}$ $b_{\text{comb}}^{f} = c_{pcomb} \left[(T - T_0) - T_0 \, ln \left(\frac{T}{T_0} \right) \right] + v_m (P - P_0)$	(16)
Electrical power	Electrical energy can be completely converted into work[18].	
Rejected heat	$b_{rech} = b_{pl} + b_{ff}$ $b_{pl} = \dot{q}_{pl} \left(1 - \frac{T_0}{T_{pl}} \right)$ $b_{ff} = \dot{q}_{ff} \left(1 - \frac{T_0}{T_{ff}} \right)$	(17)
Exhaust gases	$b_{esc}^{q} = \sum (n_i b_{xi}^{q}) + RT_0 \sum x_i \, ln \, x_i$	(18)

Note: The values of b_{aa}^{qst} and h^{st} are obtained from Table A.3 of the book by Kotas[15].

Table 3. Equations used to determine the different types of entropies of working substances[7]

Working substance	**Equation**	
Air	$s_{\text{aire}} = s^0 + c_p \, ln \left(\frac{T}{T_0} \right)$	(20)
Feed water	Table A-4	
Saturated steam	Table A-4	
Fuel	$s_{comb} = c_{p \text{ comb}} \, ln \left(\frac{T_{\text{combustion}}}{T_0} \right)$	(21)
Rejected heat	$\frac{\dot{q}_{pl}}{T_1} + \frac{\dot{q}_{ff}}{T_2}$	(22)
Exhaust gases	$s_{esc} = \frac{h_{esc}}{T_{esc}}$	(23)

(2) Entropy balance

It was carried out to determine the irreversibilities from the entropy generated in the process.

$$\dot{S}_{aire} + \dot{S}_{aa} + \dot{S}_{comb} + \dot{S}_{Gen} = \dot{S}_{esc} + \dot{S}_{vap} + \frac{\dot{q}_{pl}}{T_1} + \frac{\dot{q}_{ff}}{T_2} \quad (19)$$

The equations used to determine the entropy of each substance are shown in **Table 3**.

Table 3. Equations used to determine the different types of entropies of working substances[7]

Working substance	**Equation**	
Air	$s_{\text{aire}} = s^0 + c_p \, ln\left(\frac{T}{T_0}\right)$	(20)
Feed water	Table A-4	
Saturated steam	Table A-4	
Fuel	$s_{comb} = c_{p\,\text{comb}} \, ln\left(\frac{T_{\text{combustion}}}{T_0}\right)$	(21)
Rejected heat	$\frac{\dot{q}_{pl}}{T_1} + \frac{\dot{q}_{ff}}{T_2}$	(22)
Exhaust gases	$s_{esc} = \frac{h_{esc}}{T_{esc}}$	(23)

According to Gouy[19] irreversibilities of the process:

$$I = T_O \cdot S_{Gen} \quad (24)$$

Exergetic performance was determined ε_{GV}:

$$\varepsilon_{GV} = \frac{B_{\text{vap}} - B_{aa}}{B_{\text{aire}} + B_{\text{comb}}} \quad (25)$$

3. Results and discussion

The plant has an actual steam production of 457.2 kg/h with a fuel consumption of 0.008 kg/s. The steam demand of the process was 114.3 kg/h (**Table 4**).

The substances that had the greatest impact on the energy and energy yields of the process were fuel and saturated steam (**Table 4**). The energy yield of the generator calculated by the direct method was 0.901 and by the indirect method was 0.882 (**Table 4**). The error between the results for both methods was 2.11%, which was negligible.

The most significant substance in the exergy yield is fuel with 46%; this is due to its high energy content (**Figure 1**). Feedwater, when its temperature was varied from 80 °C to 151 °C to become saturated steam at a pressure of 0.49 MPa, increased its exergy potential by 18%; it is the second most important substance in the exergy yield (**Figure 1**). The effects of the remaining substances are practically negligible, although they must be taken into account when the air is not preheated. Irreversibilities represent 26% of the exergies, mostly due to transformations occurring in combustion and heat transfer processes (**Figure 1**)[20].

It is known that the exergy efficiency for such a steam generator should be close to 0.27[21]. For the actual operating conditions of the steam generator the exergy efficiency is 0.39. As can be observed, the exergy efficiency calculated for the steam generator studied has a value above that published in the literature[21]. When comparing the values of the measurements of this research with the reviewed one, it can be noted that for values of 2.012 of the coefficient of excess air at the exhaust gas outlet and the presence of gases such as carbon monoxide, which indicates incomplete combustion, an exergetic efficiency of 0.27 is obtained. Therefore, it is concluded that, for the operational variables and the conditions of complete combustion, the efficiency of the steam generator is higher.

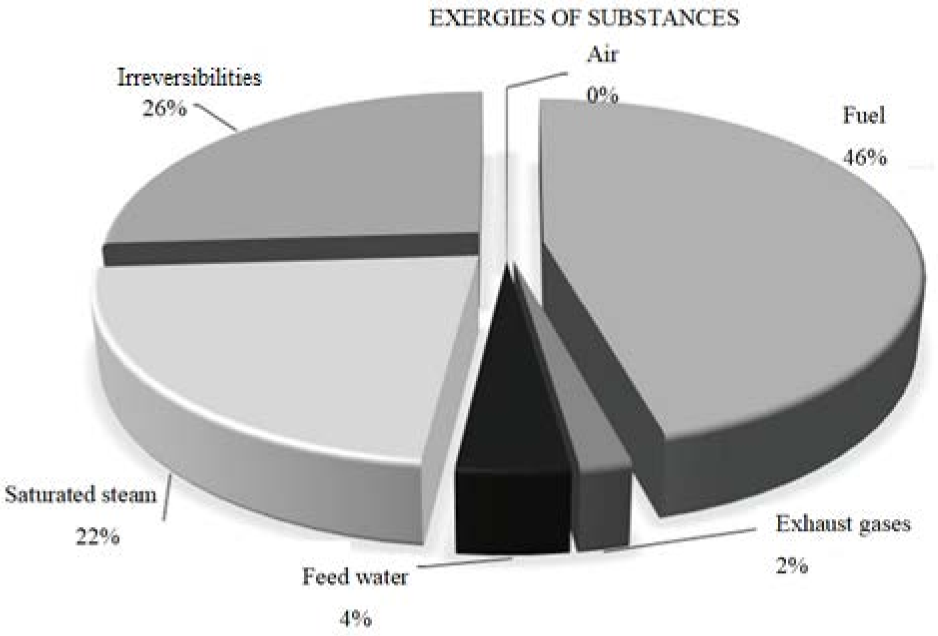

Figure 1. Percentage graph of the exergies of each substance in the process.

Table 4. Results for the different variables of the process

Variables	Energy (kW)	Exergy (kW)	Entropy (kW/K)
Air	31.057	0.575	0.1684
Fuel	339.590	362.664	0.0265
Exhaust gases	52.365	14.838	0.1107
Feed water	42.545	32.194	0.1366
Saturated steam	348.806	175.393	0.8670
Rejected heat	0.259	0.0126	0.0008
Performance direct method		0.901	
Performance indirect method		0.882	
Irreversibilities (kw)		206.190	
Gouy-Stodola irreversibilities (kw)		200.589	
Exergetic performance		0.394	

To determine the effect of saturated steam pressure on energy yields, exergy yields and irreversibilities, the above calculations were replicated for the range of 0.1 MPa to 1.3 MPa (**Figure 2**). Both the energetic and exergy yields increase with increasing saturated steam pressure. The increase in the exergy yield is more significant, with a positive variation of 13% (**Figure 2**). Irreversibilities decrease significantly in the range of 0.1 MPa to 0.4 MPa; above that value their decrease is less pronounced in relation to the increase in saturated steam pressure and experiences a total negative variation of 45 kW (**Figure 2**).

For the environmental and operating conditions of the steam generator, the energy analysis made it possible to identify, classify and measure the energy losses (**Tables 1** and **4**). The steam flow offered by the generator is four times greater than that demanded by the process. This suggests a replacement of the steam generator by another one with a lower steam production.

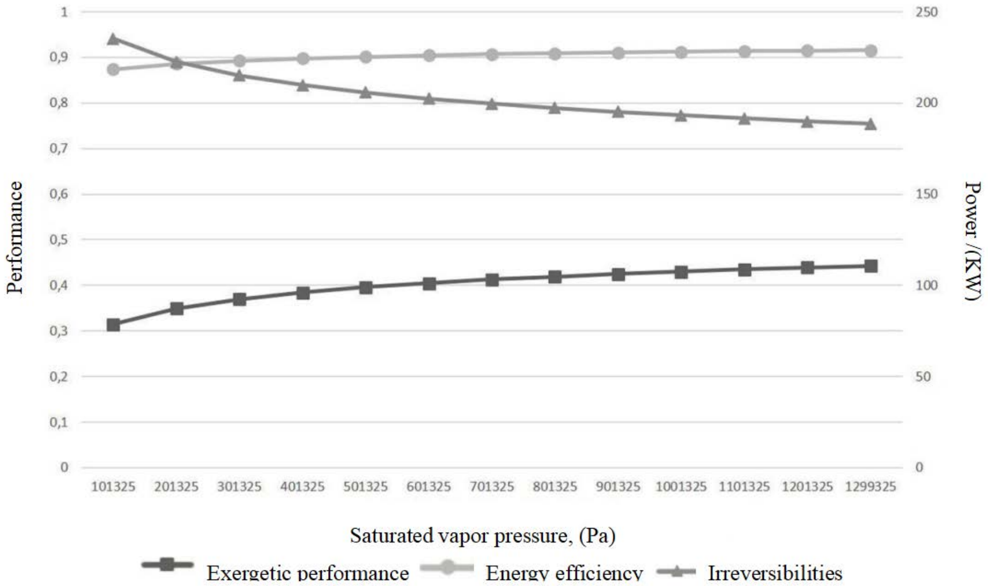

Figure 3. Behavior of energy yield, exergy yield and irreversibilities as a function of vapor pressure.

4. Conclusions

This paper describes a series of logical steps to calculate the energy efficiency of a steam generating plant. Normally, energy studies of steam generating facilities are applied to one of two methods (direct or indirect). In this case, both methods are applied to compare the results and demonstrate the relevance of using both methods indistinctly. The energy efficiency of the steam generator by the direct method is 0.901 and by the indirect method is 0.882, with a difference of 2.11%, which indicates that either method can be used. To determine the exergetic efficiency, equations were used that allow working with real values of ambient temperature, since they help to correct the difference between the parameters of the reference environment and the real environment. The exergetic efficiency of the steam generator was 0.39 and the substance that most influenced it is the fuel with 46%, then the irreversibilities of the process with 26%. These can be reduced by taking advantage of the condensed steam that is lost due to a design error in the installation. In general, but with equal importance, it was demonstrated that the steam generator is oversized for the real operating and process conditions, so it is recommended to replace it with another one of lower steam production.

Nomenclature

G	Mass flow
h	Specific enthalpy or convective heat transfer coefficient
P_{elect}	Electric power
PCI	Lower caloric value
Q	Heat flux
A_s	Heat exchange surface with the
T	Absolute temperature
η	Energy efficiency
V	Volume
Q	Heat or energy
D	Request
B	Exergy
b	Specific energy
I	Irreversibilities
n	Amount of substance
χ	Proportion of quantity of substance
R	Universal gas constant
S	Specific entropy
φ	Szargut-Styrylska relationship
c_P	Specific heat at constant pressure
v	Specific volume
P	Absolute pressure
Chemical symbols	
C	Carbon

H	Hydrogen
O	Oxygen
S	Sulfur
W	Humidity
C	Carbon

Subscripts and superscripts

Aire	Air substance
Aa	Feed water substance
Comb	Combustible substance
Vap	Saturated vapor substance
Esc	Exhaust gases
Rech	Rejected
S	Surface
F	Surface surroundings
Gv	Steam generator
Bruto	Gross
Ge	Gases at the steam generator outlet
Af	Cold air
D	Available
Gs	Dry gases
Nom	Nominal
Real	Real
Ent	Entry
Sal	Output
C	Kinetics
P	Potential
F	Physics
Q	Chemistry
I	Chemical components of the substance
Q	Chemistry
F	Physics
0	Reference environment
St	Standard
Corrg	Corrected
Comb	Fuel
Pl	Sidewall
Ff	Front and back wall
Combus	Combustion process
Gen	Generated

Conflict of interest

The authors declared no conflict of interest.

References

1. Kitto JB, Stultz SC. Steam: Its generation and use. Ohio: The Babcock & Wilcox Company; 2005.
2. Dincer I, Rosen MA. A worldwide perspective on energy, environment and sustainable development. International Journal of Energy Research 1998; 22(15): 1305–1321.
3. Lozano MA. Metodología para el análisis exergético de calderas de vapor en centrales térmicas (Spainish) [Methodology for the exergetic analysis of steam boilers in thermal power plants]. Zaragoza; 1987.
4. Ayhan B, Demirtas C. Investigation of turbulators for fire tube boilers using exergy analysis. Turkish Journal of Engineering and Environmental Sciences 2001; 25(4): 249–258.
5. Sami S, Etesami N, Rahimi A. Energy and exergy analysis of an indirect solar cabinet dryer based on mathematical modelling results. Energy 2011; 36(5): 2847–2855. doi: 10.1016/j.Energy.2011.02.027.
6. Rodríguez NG. Catálogo de especificaciones de productos rama combustibles (Spainish) [Catalog of fuel branch product specifications]. La Habana; 2014.
7. Çengel YA, Boles MA. Termodinámica (Spainish) [Thermodynamics]. Mexico: Mc-GRAW-HILL; 2012.
8. Pankratov G. Problemas de termotecnia (Spainish) [Problems of thermotechnics]. Moscow: Mir; 1987.
9. Rubio A. Generadores de vapor. Funcionamiento y explotación (Spainish) [Steam generators. Operation and exploitation]. Santa Clara: Feijóo; 2015.
10. Pavlov KF, Romankov PG, Noskov AA. Problemas y ejemplos para el curso de operaciones básicas y aparatos en tecnología química (Spainish) [Problems and examples for the course of basic operations and apparatus in chemical technology]. Moscow: Mir; 1981.
11. Ohijeagbon IO, Waheed MA, Jekayinfa SO. Methodology for the physical and chemical exergetic analysis of steam boilers. Energy 2013; 53: 153–164. doi: 10.1016/j.energy.2013.02.039.
12. Oliva LO. Indicaciones metodológicas para el cálculo de los rendimientos de los generadores de vapor (Spainish) [Methodological indications for the calculation of steam generator performances]. Santiago de Cuba; 2012.
13. Nordelo AB, González ÁR. Combustión y generación de Vapor (Spainish) [Combustion and steam generation]. Havana: Félix Varela; 2010.
14. Dincer I, Rosen MA. Exergy. Energy, environment and sustainable development. London: Elsevier Ltd; 2013.
15. Kotas TJ. The exergy method of thermal plant analysis. Butterworths; 1985.
16. Oliveira Sd. Exergy. Production, cost and renewability. London: Springer-Verlag London; 2013.
17. Szargut J, Styrylska T. Angenäherte Bestimmung der Exergie von Brennstoffen (German) [Approximate determination of the exergy of fuels]. Brennstoff-Wärme-Kraft 1064; 589–596.

18. Querol E, Gonzalez-Regueral B, Perez-Benedito JL. Practical approach to exergy and thermoeconomic analyses of industrial processes. London: Springer; 2013.
19. Guoy M. Sur l’energie utilizable (French) [On usable energy]. Journal of Physics: Theories and Applications 1889; 8(1): 501–518.
20. Kreith F, Goswami YD. The CRC handbook of mechanical engineering. CRC Press LLC; 2005.
21. Borges RJ, Monzón JA, Rodríguez MJ, *et al*. Método para la evaluación de la eficiencia e impacto ambiental de un generador de vapor (Spainish) [Method for the evaluation of the efficiency and environmental impact of a steam generator]. Energy Engineering 2016; 27(2): 135–143.

Thermal Science and Engineering (2021) Volume 4 Issue 2
doi:10.24294/tse.v4i2.1522

ORIGINAL RESEARCH ARTICLE

Analysis of the influence of the number of venetian blinds on compact heat exchangers

Alberto Menéndez-Pérez[1*], Rubén Borrajo-Pérez[1], Daniel Sacasas-Suarez[2]

[1] *Universidad Tecnológica de La Habana. Centro de Estudio de Tecnologías Energéticas Renovables, CETER. La Habana, Cuba. E-mail: amenendez@mecanica.cujae.edu.cu*
[2] *Centro de Inmunoensayo, CIE. La Habana. Cuba.*

ABSTRACT

The paper presents a numerical study of compact tube-fin heat exchangers with Venetian blades. The influence of the number of Venetian blades on the thermo-hydraulic characteristics of the exchanger is determined. A 3D numerical model was used in the laminar regime and for a Reynolds number variation, based on the hydraulic diameter between 120 and 1,200. By varying the number of Venetian blinds upstream and downstream of the central Venetian blind, it is determined that, for smaller numbers of Reynolds fins with 2 Venetian blades, the highest heat transfer coefficient is obtained. On the other hand, by increasing the air velocity at the model inlet, better heat transfer results are obtained for geometries with a higher number of Venetian blades.

Keywords: Venetian Fins; Heat Transfer Intensification; Numerical Simulation

ARTICLE INFO

Received: 24 October 2021
Accepted: 3 December 2021
Available online: 14 December 2021

COPYRIGHT

1. Introduction

Venetian blades are a widespread configuration. Each Venetian allows the initiation of a new boundary layer, while at the same time acting as a flow disturbing element. These mechanisms enhance heat transfer and make it possible to reduce the size of the equipment, thus achieving greater compactness. Several studies have been carried out on this type of fin, and new configurations have been experimented with and modeled with the aim of perfecting this geometry[1,2].

Among the extended surfaces, the most commonly used are flat, Venetian, alternating, and corrugated fins and possible combinations of these. Vortex generators have been added to these geometries as heat transfer intensifiers. The behavior of the flows is a decisive aspect in heat transfer, so there are two methods that allow altering the heat transfer patterns, as stated by T'Joen *et al.*[3] These methods are defined as: the main flow alteration method and the introduction of secondary flows. It may be the case that both mechanisms are present. The difference is that in the first method; the main features are manipulated through geometric changes, while in the second method the local flow structure is modified.

Venetian fin models are one of the most advanced intensified extended surfaces and are essentially formed by cutting the metal plate of the fin at intervals and rotating the metal strips from an angle that re-directs the flow[4].

There are combinations of heat exchangers with Venetian fins and elliptical, flat, or circular tubes. Geometries with flat tubes have better fin efficiency than geometries with circular tubes[2]. Venetian fins generally result in high heat transfer values per unit area but generate large pressure drops. The reason why Venetian blades are a complex technique to analyze is due to the fact that they have a number of different geometrical parameters. One of the parameters that distinguish Venetian blinds is the angle of inclination of the Venetian blinds (louvers), for this reason, many authors have been dedicated to investigating and establishing the optimal ranges of these angles[1,2,5].

In heat exchangers with circular or elliptical tubes, longitudinal vortices are generated when the flow passes around the tube and these are called horseshoe vortices. The main characteristic of these is that they generate high heat transfer values in the front zone of the tubes and around the tubes[6,7]. However, the heat transfer behind the tube is poor due to the recirculation of the flow in the dead or rear zone of the tube.

For low Reynolds numbers, the thickness of the boundary layer is such that the Venetian blades are embedded within it, thus forcing the fluid to change the channel through which it flows. As the Reynolds number increases, the flow that changes channel decreases, and the flow that maintains the main direction increases. This is due to the presence of a thinner boundary layer.

Karthik *et al.*[8] conclude, from the study of a water-filled air heating system using Venetian fins with elliptical tubes, that increasing the air inlet velocity produces a greater increase in the overall heat transfer coefficient than that obtained by increasing the mass flow rate of water through the tubes.

Sanders[9] states that most of the studies related to this subject are carried out in two dimensions, thus ignoring the effects created on the surface of the tubes. This is because recent articles have concluded that the analysis of three-dimensional flows close to the tube wall does not influence the performance of the exchanger equipment.

Some authors conclude that by using Venetian blades with different degrees of inclination each, good results can be obtained for small Reynolds values. The study consists of comparisons, varying the inter-fin pitch and the angle of inclination of the Venetian blades for a particular arrangement where the Reynolds number takes values between 100 and 1,000 approximately[1,7,8]. A very interesting fact is that for small values of the inter-fin pitch and large values of the tilt angle, large and strong airflow deviations are achieved.

The Schmidt correlation represents a good analytical model to find the efficiency of flat fins and circular tubes. This method offers an equation for the efficiency based on geometrical parameters and materials, used in experimental studies when it is impossible to obtain the temperatures at the fin wall[10], although this method is valid only when radial heat conduction exists in one dimension.

According to Ameel *et al.*[11], the black box the black box behavior of heat exchangers is commonly analyzed by the Logarithmic Mean Temperature Difference (LMTD) method or by the NTU (Number of Transfer Units) method.

There is research showing that Venetian blinds redirect the airflow in the direction parallel to their own planes[12,13], where visualization of the flow in scaled models is used to reach this conclusion.

Achaichia and Cowell[14] conclude in an investigation that undesired inter-fin flows are caused when the inter-veneer pitch is combined with large inter-veneer spacings and small veneer angles. The above criterion is also supported by Tu *et al.*[15] who state that better results are obtained using geometries with small inter-blade pitches (1.6 mm) and small blade angles of 26°.

Kang *et al.*[16] conclude that the use of Venetian blind arrays and multiple circular tubes produces 10%–15% higher heat transfer performance than using flat tubes for the same volumetric flows and velocities.

Although the literature review shows the existence of multiple studies on this type of fins, there is little information on the influence of the number of Venetian blades on the thermo-hydraulic characteristics of these heat exchangers. Precisely, this work determines the influence of the number of Venetian blades on the heat transferred and the pressure drop in a Reynolds range between 120 and 1,200.

2. Materials and method

Figure 1 shows a front view of a Venetian blind, presenting, among other things, the angle of inclination of the Venetian blinds and the height of the blinds. The figure corresponds to having fins equal to 2 blinds on either side of the central blind, commonly referred to as redirected blinds.

Table 1 below shows the dimensions of the one and two-row Venetian finned tube models to be studied.

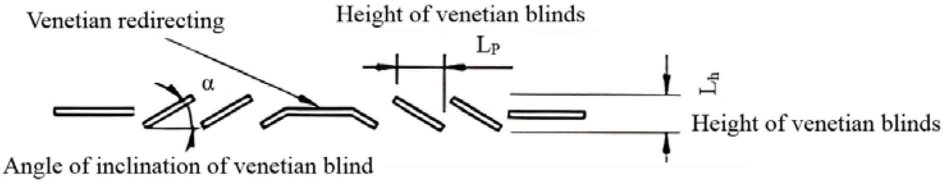

Figure 1. Front view of a venetian blind with a row of tubes.

Table 1. Dimensions of the venetian fin models for one and two rows of circular tubes

Description	Nomenclature	1 row		2 rows	
Pitch between fins [mm]	F_P	1.5			
Fin length [mm]	L	17		34	
Transversal fin spacing [mm]	S_t	22			
Angle of inclination of venetian blind [°]	a	27			
Blade thickness [mm]	t_f	0.1			
Width of venetian blind area [mm]	A_L	9			
Tube radius [mm]	R	4.5			
Distance from flap outlet to channel outlet [mm]	y	60			
Distance from channel inlet to flap inlet [mm]	x	7.5			
Total channel length [mm]	L_C	84		101	
Number of venetian blinds with respect to redirection	C_L	2	3	4	5
Venetian blind pitch [mm]	L_P	1.56	1.15	0.91	0.75
Venetian blind height [mm]	L_h	0.8	0.62	0.43	0.35
Fin Material	Aluminum				

The equations that govern the study of a phenomenon in which the motion of a fluid and its heat exchange with the surfaces it contacts are of interest are the continuity equation, the equations of quantity of motion in each of the axes and the energy equation. These equations in the computational domain, for incompressible flow, with constant properties and in steady state without viscous dissipation and in laminar regime, can be expressed in the same order in which they are mentioned, as follows (equations 1, 2 and 3):

$$\frac{\partial u_i}{\partial x_i} = 0 \qquad (1)$$

$$\rho\left[\frac{\partial u_j}{\partial t} + \frac{\partial u_j u_i}{\partial x_j}\right] = -\frac{\partial p}{\partial x_i} - \frac{\partial \tau_{ij}}{\partial x_j} \qquad (2)$$

$$c_p \rho\left[\frac{\partial T}{\partial t} + \frac{\partial u_j T}{\partial x_j}\right] = \frac{\partial}{\partial x_j}\left[\lambda \frac{\partial T}{\partial x_j}\right] \qquad (3)$$

The solution of equations 1, 2 and 3 is achieved for a computational domain shown in **Figure 2**. The domain, as can be seen, has been extended in the inlet and outlet region of the model. It was extended 7 times the fin spacing in the inlet direction and 7 times the minor diameter of the tube in the outlet direction. The need to have a uniform and one-dimensional velocity profile at the inlet of the model, as well as to avoid the existence of reverse flow in the outlet section is the reason for these extensions.

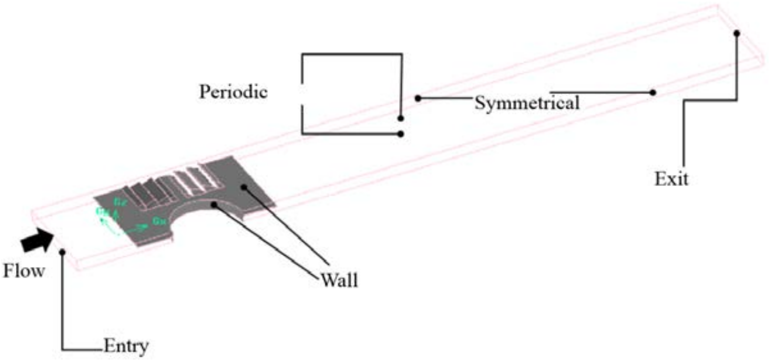

Figure 2. Representation of channel and fin boundary conditions.

The interpolation used for the energy was of the second order upwind type since this is more effective when there is no mesh totally normal to the flow. In the pressure-velocity coupling, the simple method and a first-order upwind scheme were used in the momentum equations and the standard model in the pressure. The fin in the central region of the domain is taken as a solid, while the channels above and below are considered to be fluid regions. Two boundary conditions that are needed are the temperature in the tube and the fluid inlet parameters to the channel. The temperature of the tubes will be considered equal to that of the cooling fluid circulating inside them, so the value of the heat transfer coefficient on the inside of the tube is disregarded given its high value when compared to that which must exist on the outside of the tube. The inlet velocity is data that can vary because the study of different Reynolds numbers requires the change of the velocity at the inlet. The general boundary conditions by region are summarized below:

At model input, equation 4:

$$v = w = 0 \quad u = const. \quad T = const. \tag{4}$$

In the upper and lower part of the domain, periodicity conditions were considered. On the fin surface, in addition to the existence of conjugate heat transfer, there is a no-slip condition, equation 5:

$$u = v = w = 0 \tag{5}$$

On the surface of the tube we will have, equation 6:

$$u = v = w = 0 \quad T = const. \tag{6}$$

$$\frac{\partial u}{\partial y} = \frac{\partial w}{\partial y} = \frac{\partial T}{\partial y} = v = 0 \tag{7}$$

At the model output, equation 8:

$$\frac{\partial u}{\partial x} = \frac{\partial v}{\partial x} = \frac{\partial w}{\partial x} = \frac{\partial T}{\partial x} = 0 \tag{8}$$

The model works under a laminar flow regime with low air velocities in the channel, in anticipation of the existence of annoying kinetic noises. It is also modeled in steady state. The flow to be analyzed is three-dimensional, with the velocity and temperature fields decoupled, which guarantees the independence between both variables. The flow velocity at the model inlet is varied between 0.5 and 5 m/s. The air temperature at the model inlet is 300 K, and at the pipe wall, it is considered equal to 286 K. The flow is considered incompressible.

The geometry and channel region are meshed with hybrid tetrahedron (TGrid) elements in Gambit 2.4.6 software. It has meshed in such a way that the density of elements was able to produce a mesh-independent solution, since the difference between the results of pressure drop and heat transfer coefficient does not exceed 1.6% between two successive mesh sizes. It does not have any element with skewness volumes, nor any element with negative or inverted volume since both would conspire against the convergence of the iterations. For the meshing, size functions were used on the more complex faces, as shown in **Figure 3**.

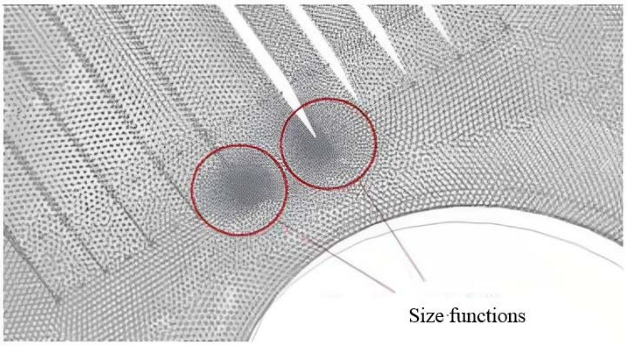

Figure 3. View of the mesh in the fin area where size functions were used.

2.1 Numerical model validation

In order to consider the results valid, the method used for their determination must be certified. The method used here in the certification consists of constructing a computational model with dimensions and characteristics corresponding to one that had already been investigated and its results are available in the literature. The model studied by Han *et al*.[17] was selected and validated against experimental results obtained by Wang *et al*.[18,19] Han *et al*. state that the average deviations of the friction factor (*f*) and Colburn factor (*j*) between their numerical model and their validation based on the experiments of Wang *et al*. are 9.3% and 4.5%, respectively. The authors' experiments were based on a similar venetian fin geometry with elliptical tube but using the venetian blades with variable lengths around the edge of the tube. Another difference is that the air entering the wind tunnel has a temperature of 308 K and the wall temperature of the tubes is 353 K. This study has all the dimensions different from the model studied in this work. The same types of flows, interpolations, boundary conditions and convergence criteria for energy and momentum are used. A coupling between velocity and pressure is also implemented using the SIMPLEC algorithm.

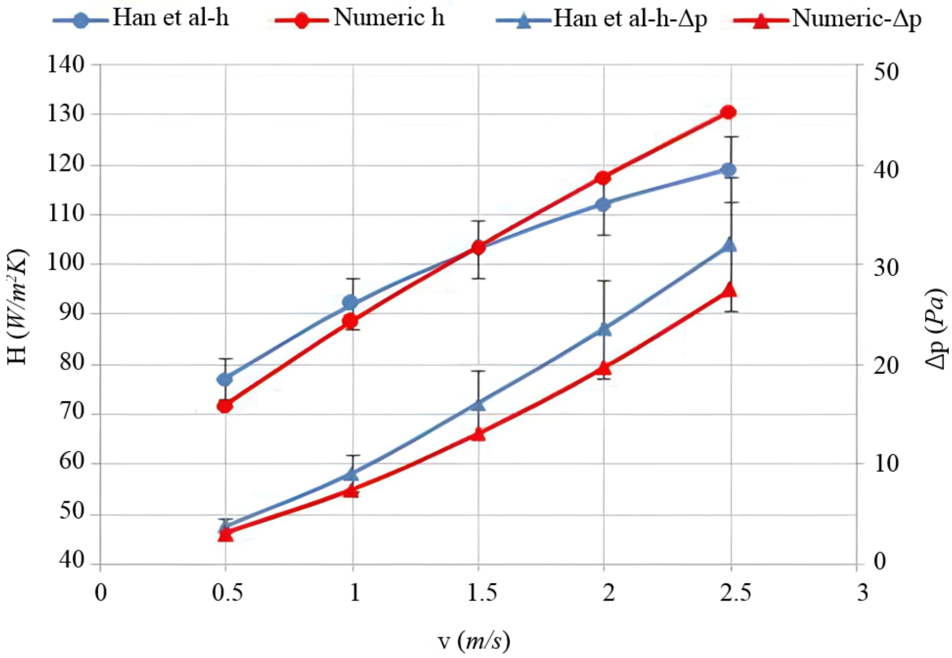

Figure 4. Validation of the global heat transfer coefficient of film and pressure drop.

Figure 4 shows that for the values of Δp, the behavior is quite approximate, although the numerical model slightly underestimates this parameter. The behavior of the heat transfer coefficient is also approximated by the numerical model. The difference between the behaviors of these curves may be caused by the inaccuracy in the reproduction of the geometry shown in the work of Han *et al*., which does not provide the necessary details for the exact reproduction of the model nor the correct constructive form. This work overestimates the value of h for velocities above 1.5 m/s, while underestimates the value of h for velocities below 1.5 m/s when compared to those of Han *et al*.[17].

The average deviations between the results for the global heat transfer film coefficient and the pressure drop of the work of Han *et al*.[17], are of the order of 5.22% and 21.61%, respectively. Then, despite the differences mentioned above, it can be noted that most of the values are within the uncertainty region, which delimits the error bars in **Figure 4**. In correspondence with the above, we can affirm that the method used in the work to achieve the simulation is valid. It can then be established that the method used, the simplifications, as well as the boundary conditions established in this work are valid to achieve the proposed objectives.

2.2 Data reduction

The Reynolds number was determined using the velocity at the minimum channel section $u_{\min}$, while the characteristic length is the hydraulic diameter of the channel D_h, equation 9:

$$Re = \frac{\rho u_{\min} D_h}{\mu} \tag{9}$$

The heat transferred at the exchange surface can be calculated with the change in air temperature between the inlet and outlet sections of the model ($T_{\text{out}} - T_{\text{in}}$), the mass flow m_a, and the specific heat of the air c_{pa}, according to equation 10:

$$Q = m_a c_{pa} \left(T_{\text{out}} - T_{\text{in}}\right) \tag{10}$$

When the fluid undergoes a phase change inside the tubes, it is common practice to consider a high value for the internal film heat transfer coefficient. Assuming this, the overall coefficient will be obtained by considering only the external heat transfer coefficient and the conduction inside the tube wall. The temperature of the internal wall of the tubes is considered constant and with the same value as that of the circulating coolant. The heat transferred can also be calculated through the well-known equation involving the logarithmic ΔT_{ln} (LMTD), knowing the transfer area A_f, the overall transfer coefficient $\bar{h}$, and the aforementioned temperature difference, equation 11:

$$Q_h = \eta_0 \bar{h} A_f F \Delta T_{ln} \tag{11}$$

The LMTD correction factor, F, was considered to be zero because one of the fluids maintains its temperature constant. The global heat transfer coefficient is calculated considering the equality of the heat expressed by equations 10 and 11.

$$Q = Q_h$$

The fin efficiency η_0 is involved and is itself a function of the heat transfer coefficient. The efficiency is calculated as a function of the fin efficiency η and the total transfer area A_0, equation 12:

$$\eta_0 = 1 - \frac{A_f}{A_0}(1-\eta) \tag{12}$$

The fin efficiency for a rectangular fin is determined using the approximate method developed by Schmidt for circular fins. The fin efficiency is expressed according to equation 13:

$$\eta = \frac{\tanh\left(m r_t \varphi\right)}{\left(m r_t \varphi\right)} \tag{13}$$

The value of m is calculated with the thermal conductivity of the fin (k_f) and its thickness (f_t), equation 14.

$$m = \sqrt{\frac{2\bar{h}}{k_f f_t}} \tag{14}$$

On the other hand, the term φ is obtained with the equivalent tube radius divided by the tube radius. This parameter depends on the geometry of the heat exchanger according to (equation 15 and 16):

$$\varphi = \left(\frac{R_{eq}}{r_t} - 1\right)\left(1 + 0.35\, ln\left(\frac{R_{eq}}{r_t}\right)\right) \tag{15}$$

$$\frac{R_{eq}}{r_t} = 1.27 \frac{X_m}{r_t}\left(\frac{X_L}{X_m} - 0.3\right)^{1/2} \tag{16}$$

Where X_m is half of the transverse spacing and X_L is calculated according to equation 17:

$$X_L = \frac{\sqrt{\left(\frac{S_T}{2}\right)^2 + S_L^2}}{2} \tag{177}$$

The fin efficiency and the global heat transfer coefficient have an implicit formulation, therefore an iterative process is needed. The equality of heats of equations 10 and 11 is the one that must be satisfied. For a fixed geometry, there is only one pair of values of these magnitudes, fin efficiency and global transfer coefficient, that meet this condition. Then the Colburn factor can be obtained from the Prandtl number and the friction factor according to equation 18:

$$j = \frac{\bar{h}}{\rho_m c_{pa} u_{min}} Pr^{2/3}$$

$$f = \frac{\Delta p}{0.5 \rho_a u_{min}^2} \left(\frac{A_{min}}{A_t} \right) \tag{18}$$

Where A_{min} is the minimum area of the passage section and A_t is the heat transfer area.

3. Results and discussion

The following are the essential elements to discuss the results obtained. The values obtained for the relevant quantities h, Δp, j, f and Q will be discussed here. These are the indicators generally used to make comparisons between heat exchange surfaces and therefore define which are the best performing surfaces.

It is customary, as mentioned before, in the current literature to present the behavior of heat exchangers using dimensionless numbers and consequently the values of the Colburn factor j and the Friction factor f as a function of the Reynolds number are shown in **Figure 5** and **Figure 6**. The legend of the figure refers to the number of venetian blades on each side of the central venetian blade, which produces a change of direction in the angle of the blades. Therefore, a number 3 on the scale would mean a total of 6 additional venetian blinds to the central one.

A probable explanation for this phenomenon is that when the number of venetian blades increases, so does the number of surfaces where new boundary layers develop (leading edges of the venetian blades). When the number of venetian blades is lower, they bring the cold fluid flowing through the center of the channel closer to the fin surface. This is possible because the smaller the number of blades, the longer the blades are.

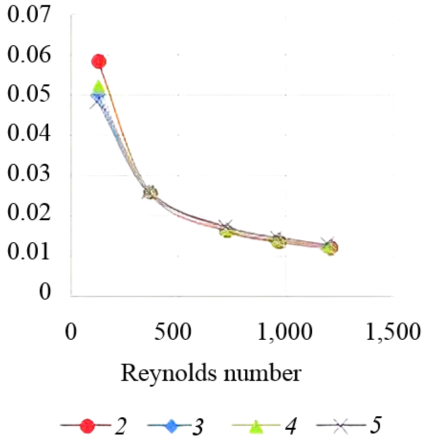

Figure 5. Colburn factor as a function of Reynolds number for two rows of tubes.

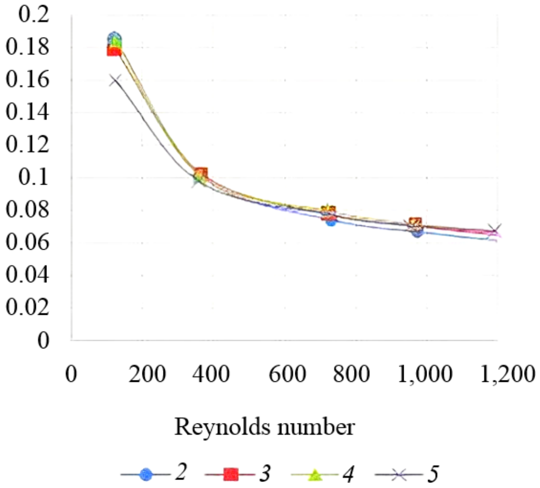

Figure 6. Friction factor as a function of Reynolds number for two rows of pipes.

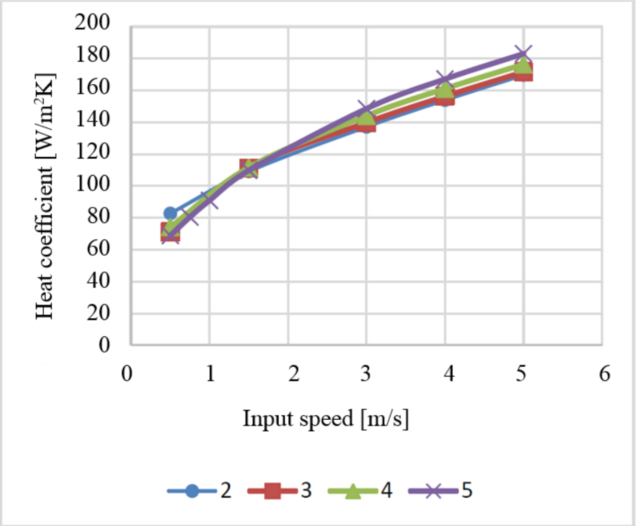

Figure 7. Heat transfer coefficient as a function of inlet velocity for two rows of tubes.

Figure 8 shows that the most important heat transfer mechanism, when velocities are minimal, is the development of the boundary layer at the front of the fin and the venetian blades, as it can be observed how the venetian blades break the boundary layer of the fluid, which influences the increase of the heat exchanged. In addition, the region of low heat transfer coefficients associated with the dead zone of the tubes is clearly observed. The differences in heat exchanged in the venetian blind region are due to the incidence of the flow on the surfaces of the pipes.

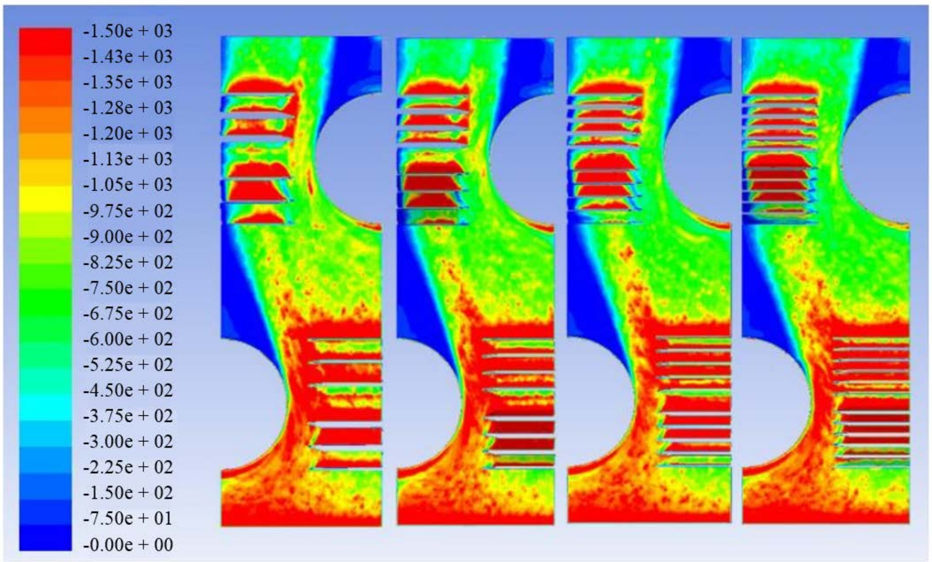

Figure 8. Heat flux in (W/m^2) over the top face of the fin surface for models with C_L between 2 and 5 (from left to right). Velocity of 1.5 m/s from bottom to top.

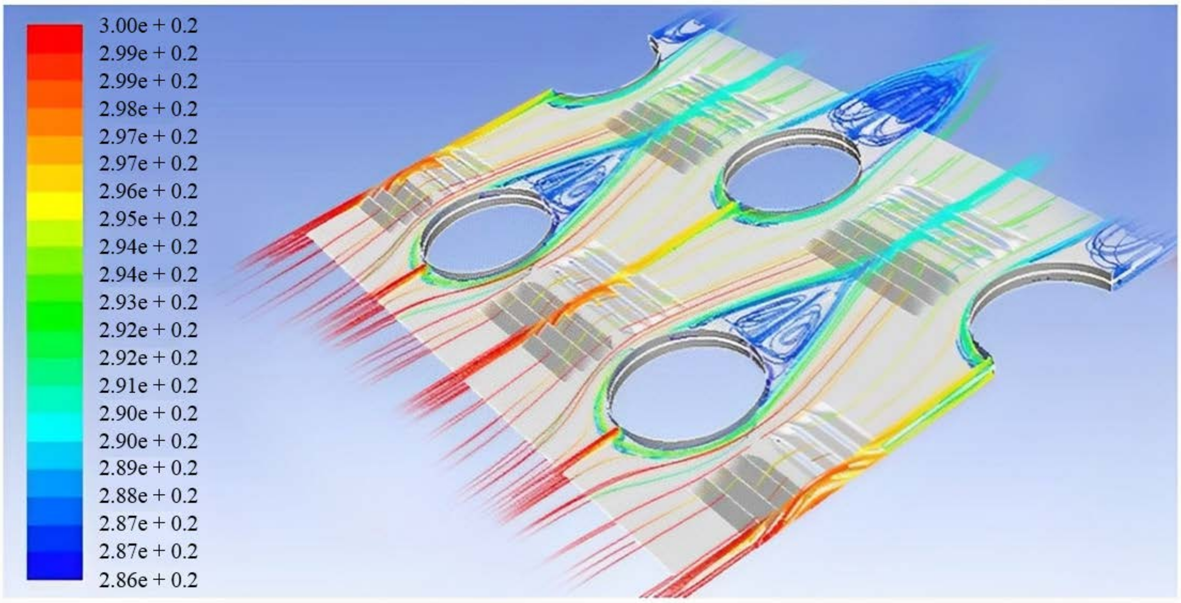

Figure 9. Colored streamlines as a function of temperature in degrees Kelvin. For an inlet velocity of 1.5 m/s.

Figure 9 shows the streamlines generated at the inlet face of the channel for an extension of the symmetry condition of the model. The differences in the horseshoe vortices in the first and second tubes are clearly seen. In the second tube, these vortices tend to contour the tube less, causing a larger recirculation region than that observed behind the tubes in the first row. It is also observed how the acceleration effect that the flow experiences when passing through the second row is manifested, decreasing the recirculation in the rear area of the tube.

Also, **Figure 10** shows the temperature profiles at the top of the fin. The main flow direction is from right to left. It can be observed that as the fluid has a higher velocity at the inlet of the model, the average temperature of the fin is higher and there is less uniformity at the outlet of the fluid. As this surface is a heat exchanger where the air is at a higher temperature than the fin surface, there is a greater heat transfer, since the temperature difference between the fin surface and the fluid is greater. It is observed at the outlet of the fin that the temperature is never constant over the entire surface, highlighting that the higher the velocity, the greater the temperature gradients.

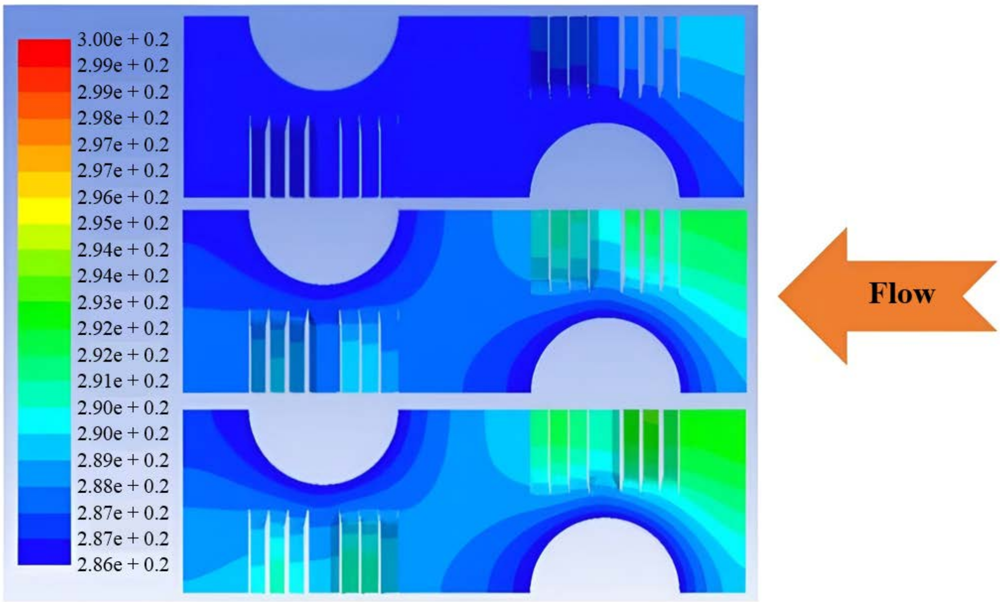

Figure 10. Temperature [K] at the top face of the fin for three inlet velocities, 0.5, 3.0 and 5.0 m/s (from top to bottom).

3.1 Limitations of the work

The results of the work are valid only for fins of similar geometry and in the vicinity of the dimensions of the one studied here, as long as the flow regime is laminar.

4. Conclusions

A computational model capable of reproducing the thermo-hydraulic behavior, shown in the literature consulted, of a heat exchange surface of venetian fins and circular tubes was created. This surface was used as a vehicle for the certification of the method.

Among the fundamental results, it was determined that for the model with two rows of tubes, the flow tends more and more to separate from the lateral face as the velocity increases, while in the first tube the behavior is the opposite, due to the presence of the second tube.

The heat transfer coefficient was found to increase when the number of venetian blades is lower, a result that is accentuated for lower Reynolds numbers. When higher velocities were studied, it was the models with the highest number of venetian blades that presented the best thermal-hydraulic behavior.

Conflict of interest

The authors declare that they have no conflict of interest.

References

1. Wang CC, Chen KY, Liaw JS, *et al*. An experimental study of the air-side performance of fin-and-tube heat exchangers having plain, louver, and semi-dimple vortex generator configuration. International Journal of Heat and Mass Transfer 2015; 80: 281–287.
2. Delač B, Trp A, Lenić K. Numerical investigation of heat transfer enhancement in a fin and tube heat exchanger using vortex generators. International Journal of Heat and Mass Transfer 2014; 78: 662–669.
3. T'Joen C, Huisseune H, Canière H, *et al*. Interaction between mean flow and thermo-hydraulic behaviour in inclined louvered fins. International Journal of Heat and Mass Transfer 2011; 54(4): 826–837.
4. Powar VS, Mirza MM. Performance of louver fin pattern as extended surface used to enhance heat transfer—A review. Int Journal of Engineering Research and Applications, 2013, 3: 1409–1413.
5. Wang CC, Chen KY, Lin YT. Investigation of the

semi-dimple vortex generator applicable to fin-and-tube heat exchangers. Applied Thermal Engineering 2015; 88: 192–197.

6. Zhong Y, Jacobi AM. Experimental study of louver-fin flat-tube heat exchanger performance under frosting conditions. In: Shah RK, Ishizuka M, Ruby TM, *et al.* (editors). Proceedings of the Fifth International Conference on Enhanced, Compact and Ultra-Compact Heat Exchangers: Science, Engineering and Technology; 2005 Sept 11–16; Whistler, British; Columbia, Canada. Hoboken, New Jersey, USA: Engineering Conferences International; 2005.
7. Salviano LO, Dezan DJ, Yanagihara JI. Optimization of winglet-type vortex generator positions and angles in plate-fin compact heat exchanger: Response surface methodology and direct optimization. International Journal of Heat and Mass Transfer 2015; 82: 373–387.
8. Pooranachandran K, Ali KSIL, Narasingamurthi K, *et al*. Experimental and numerical investigation of a louvered fin and elliptical tube compact heat exchanger. Thermal Science 2015; 19(2): 679–692.
9. Sanders PA. Effects of louver lengthand vortex generators to augment tube wall heat transfer in louvered fin heat exchangers [MSc thesis]. Virginia, USA: Virginia Polytechnic Institute and State University; 2005.
10. Huisseune H, T'Joen C, De Jaeger P, *et al*. Influence of the louver and delta winglet geometry on the thermal hydraulic performance of a compound heat exchanger. International Journal of Heat and Mass Transfer 2013; 57(1): 58–72.
11. Ameel B, Degroote J, Huisseune H, *et al*. Interaction effects between parameters in a vortex generator and louvered fin compact heat exchanger. International Journal of Heat and Mass Transfer 2014; 77: 247–256.
12. Schmidt TE. Heat transfer calculations for extended surfaces. Refrigerating Engineering 1949; 57(4): 351–357.
13. Ameel B, Huisseune H, Degroote J, *et al*. On fin efficiency in interrupted fin and tube heat exchangers. International Journal of Heat and Mass Transfer 2013; 60: 557–566.
14. Achaichia A, Cowell TA. Heat transfer and pressure drop characteristics of flat tube and louvered plate fin surfaces. Experimental Thermal and Fluid Science 1988; 1(2): 147–157.
15. Tu X, Lin H, Liang X. CFD simulation and experimental study on air-side performance for MCHX. International Refrigeration and Air Conditioning Conference; 2010 Jul 10–15; Indiana, USA. Purdue University; 2010.
16. Kang H, Jacobi AM, Minkyoo L. Air-side heat transfer performance of louver fin and multi-tube heat exchanger for fuel-cell cooling application, in air-side h eat transfer performance of louver fin and multi-tube heat exchanger for fuel-cell. International Refrigeration and Air Conditioning Conference; 2012 Jul 16–19; Indiana, USA. Purdue University; 2012.
17. Han H, He YL, Li YS, *et al*. A numerical study on compact enhanced fin-and-tube heat exchangers with oval and circular tube configurations. International Journal of Heat and Mass Transfer 2013; 65: 686–695.
18. Wang CC, Lee CJ, Chang CT, *et al*. Some aspects of plate fin-and-tube heat exchangers: With and without louvers. Journal of Enhanced Heat Transfer 1999; 6(5): 357–368.
19. Wang CC, Tsai YM, Lu DC. Comprehensive study of convex-louver and wavy fin-and-tube heat exchangers. Journal of Thermophysics and Heat Transfer 1998; 12(3): 423–430.

EnPress Publisher, LLC
Add: 9650 Telstar Avenue, Unit A, Suit 121, El Monte, CA 91731
Tel: +1 (949) 299 0192
Email: contact@enpress-publisher.com
Web: https://enpress-publisher.com